



universität
wien

DISSERTATION

Titel der Dissertation

„Deformation Induced Disordered Nanocrystalline FeAl
Studied by Advanced Transmission Electron Microscopy
Methods“

Verfasser

Dipl.-Ing. Mag. Christoph Gammer

angestrebter akademischer Grad

Doktor der Naturwissenschaften (Dr. rer. nat.)

Wien, 2011

Studienkennzahl lt. Studienblatt: A 791 411

Dissertationsgebiet lt. Studienblatt: Physik

Betreuerin / Betreuer: Ao. Univ.-Prof. Mag. Dr. Christian Rentenberger

Abstract

Bulk nanocrystalline intermetallic materials receive increasing scientific interest since they often show novel properties. In the present work intermetallic FeAl was made nanocrystalline by high pressure torsion deformation of a B2 ordered Fe-45at.%Al alloy. The resulting structures consist of nanoscaled grains with high defect densities and highly irregular grain boundaries. For their detailed characterization transmission electron microscopy studies combining imaging and diffraction are used. The complex image contrasts of deformation induced nanograins necessitate the development of new analysis techniques. A method yielding profile analysis from selected area electron diffraction patterns (PASAD) is worked out allowing a quantitative analysis of nanomaterials on a local scale. PASAD is applied successfully to analyse small nanocrystalline regions that are formed in FeAl during deformation showing the unexpected result that the coherently scattering domain (CSD) size is not changing as a function of strain. By applying PASAD to tilt series of diffraction patterns, a new method is derived that allows the determination of the average size and morphology of the CSD in 3D. It is shown that the average CSD is elongated in the shear plane. It was reported in the literature that in FeAl the long-range order is lost during deformation. In contrast, the present work shows that the disorder is not complete since it is revealed that chemically ordered nanodomains of about 2 nm are observed after deformation. Thermal annealing leads to the recurrence of the order, the recovery of dislocations and the rearrangement of grain boundaries. To study these processes, the ordered domain size, the CSD size and the grain size are monitored during annealing. The analysis yields the surprising result that during annealing the grain size is reduced by a factor of 2, while the CSD size increases by a factor of 2 and the ordered domain size by a factor of 15. Based on the coarsening of the chemically ordered nanodomains a model for the reordering process is developed and fitted to the results from differential scanning calorimetry. The model allows to determine the vacancy concentration, the vacancy migration enthalpy and the vacancy migration volume. Finally, by annealing of specimens deformed by high pressure torsion without unloading, i.e. maintaining the hydrostatic pressure, the vacancy concentration is determined and compared to that after unloading, thus confirming the occurrence of vacancy relaxation during unloading.

Zusammenfassung

Nanokristalline intermetallische Werkstoffe stoßen aufgrund ihrer oft unerwarteten Eigenschaften auf zunehmendes wissenschaftliches Interesse. In der vorliegenden Arbeit wurde nanokristallines intermetallisches FeAl durch Verformung der B2 geordneten Fe-45at.%Al Legierung mittels Hochdrucktorsion hergestellt. Die resultierende Struktur besteht aus nanoskaligen Körnern mit hohen Versetzungsdichten und unregelmäßigen Korngrenzen. Für die detaillierte Charakterisierung wurden Beugungsmodus und Abbildungsmodus im Transmissionselektronenmikroskop kombiniert. Die komplexen Bildkontraste der verformungsinduzierten Nanokörner erfordern die Entwicklung neuer Analysemethoden. Hier wird eine Methode für Profilanalyse aus Feinbereichsbeugungsbildern (PASAD) vorgestellt, die lokal aufgelöste quantitative Analyse von Nanomaterialien erlaubt. PASAD wird erfolgreich auf nanokristalline Strukturen angewendet, die sich bei der Verformung von FeAl ausbilden. Es zeigt sich das unerwartete Resultat, dass sich die Größe der kohärenten Streuvolumina (CSD) mit zunehmendem Verformungsgrad nicht ändert. Durch Anwendung von PASAD auf eine Kippserie von Beugungsbildern wird eine Methode entwickelt, die erlaubt die mittlere Größe und Form der CSD in 3D zu bestimmen. Es zeigt sich, dass die CSD in der Torsionsebene elongiert sind. Es wurde in der Literatur berichtet, dass Verformung die Ordnung in FeAl zerstört. Im Gegensatz dazu wird in der vorliegenden Arbeit gezeigt, dass die Entordnung nicht vollständig ist, da nach der Verformung chemisch geordnete Nanodomänen vorhanden sind (ca. 2 nm). Eine thermische Behandlung führt zu Ordnungseinstellung, Erholung sowie der Neuordnung der Korngrenzen. Um diese Prozesse genauer zu untersuchen, werden die Größe der Ordnungsdomänen, die Größe der CSD und die Korngröße beim Aufheizen gemessen. Durch die thermische Behandlung reduziert sich die Korngröße um einen Faktor 2, wobei gleichzeitig die Größe der CSD um einen Faktor 2 und die Größe der Ordnungsdomänen um einen Faktor 15 anwachsen. Basierend auf der Vergrößerung der Ordnungsdomänen wird ein Modell für die Ordnungseinstellung entwickelt und an die Resultate von dynamischer Differenzkalorimetrie angepasst. Das Modell erlaubt die Bestimmung der Leerstellendichte, der Leerstellen-Wanderungsenthalpie und des Leerstellen-Wanderungsvolumens. Durch gezieltes Ausheilen von Proben, die mittels Hochdrucktorsion verformt wurden, ohne zu entlasten, wird die Leerstellendichte bestimmt und mit jener nach Entlastung verglichen. Dabei wird eine Reduktion der Leerstellendichte beim Entlasten bestätigt.

Contents

Outline of this Work	xv
1 Introduction	1
1.1 Chemical Order in FeAl	1
1.1.1 Phase Diagram	1
1.1.2 Chemical Order	1
1.1.3 Ordered Domains	3
1.1.4 Thermodynamics of the Ordered State	4
1.2 Structure of Crystalline Materials	5
1.2.1 Defects	5
1.2.2 Grains	5
1.3 Nanocrystalline Materials	7
1.3.1 Production of Nanocrystalline Materials	7
1.3.2 Deformation of Nanocrystalline Materials	8
1.4 Mechanical Properties of FeAl	13
1.5 Potential Applications of Nanocrystalline FeAl	15
1.6 Previous Work	16
1.6.1 HPT Deformation of Intermetallic Compounds	16
1.6.2 Ball Milling of FeAl	16
2 Experimental Procedure	17
2.1 Production of the Raw Material	17
2.2 High Pressure Torsion	18
2.2.1 Illustration of the HPT Deformation	18
2.2.2 HPT Deformation of FeAl	18
2.3 Preparation of the TEM Samples	20
2.3.1 Preparation of Plan-View TEM Samples	20
2.3.2 Preparation of Cross-Section TEM Samples	23
2.4 Diffraction and Imaging as Fourier Transforms	26
2.5 Transmission Electron Microscopy	30
2.5.1 Electron Waves and Lenses	30
2.5.2 Schematics of a TEM	33
2.5.3 Diffraction	33
2.5.4 Contrasting	35
2.5.5 HRTEM	36

2.6	Diffraction	41
2.6.1	Diffraction and the Ewald Constuction	41
2.6.2	The Intensity of the Diffracted Beams	41
2.6.3	Dynamic Effects in Electron Diffraction	44
2.6.4	The Width of the Diffracted Peaks	45
2.6.5	Size Broadening	45
2.6.6	Strain Broadening	52
2.6.7	Strain Field of Dislocations	55
2.6.8	The Modified Williamson-Hall Plot	56
2.6.9	Other Effects Leading to Peak Broadening	56
2.6.10	Peak Positions	57
2.6.11	Diffraction in FeAl	58
2.7	Peak Broadening in 3D	58
2.8	Texture	59
2.9	Microhardness Measurements	60
2.10	Differential Scanning Calorimetry	61
2.10.1	Schematic Representation of a DSC	61
2.10.2	Evaluation of DSC Curves	63
2.10.3	Determination of the Activation Energy from a DSC Curve	63
2.10.4	Reordering	65
2.10.5	Recovery	65
2.10.6	Grain Growth	65
2.10.7	Other Kinetic Models	66
2.10.8	Experimental Realisation of the DSC Measurements	67
3	Advanced Transmission Electron Microscopy Tools for Nanocrystalline Materials	69
3.1	Focused Local Profile Analysis by Electron Diffraction	69
3.1.1	The Need for PASAD	69
3.1.2	Performing a PASAD Evaluation	70
3.1.3	The DigitalMicrograph Plugin PASAD-Tools	75
3.1.4	Outlook	79
3.2	Dark Field Scanning	81
4	Nanocrystallisation of FeAl by High Pressure Torsion Deformation	87
4.1	Evolution of the Nanocrystalline Structure	87
4.1.1	TEM Investigations	87
4.1.2	Using PASAD for a Focused Local Analysis	88
4.1.3	Modified Williamson-Hall Plot	90
4.1.4	Reproducibility of the PASAD Analysis	93
4.2	3D Analysis of the Nanocrystalline Structure	93
4.2.1	TEM Investigations	93
4.2.2	3D Analysis by Electron Diffraction	96
4.2.3	Applicability of 3D Profile Analysis	99

5	Thermal Stability of Nanocrystalline FeAl	101
5.1	DSC and TEM Investigations	101
5.2	Grain Size Evolution During Heating	106
5.3	Using Dark Field Series to Determine the Grain Size Reduction . . .	107
5.4	Evolution of the Coherently Scattering Domain Size	112
5.5	Growth of Nanosized Ordered Domains	113
5.6	Grain Size Reduction by Heating	120
6	Modelling the Reordering	123
6.1	Kinetics of the Vacancy Diffusion	123
6.2	Reordering via Ordering Jumps	124
6.3	Reordering via the Coarsening of Ordered Domains	125
6.3.1	Derivation of the Model	125
6.3.2	Parameters	128
6.3.3	Influence of Parameter Changes	129
6.4	Fitting the Model to a DSC Curve	130
6.5	Fitting the Model to a DSC Curve of an Annealed Sample	135
6.6	Comparison of the Values with Literature Data	137
6.7	The Effect of Pressure on the Reordering	138
6.8	The Effect of Unloading	140
7	Summary and Conclusions	145
	Included Publications	151
	Bibliography	153
A	Acknowledgements	177
B	Curriculum Vitæ	179

List of Figures

1.1	Phase diagram of FeAl. Source:[Kattner86]	2
1.2	Diagram representing the A2- and B2-structure	2
1.3	Schematic illustration of an antiphase boundary	4
1.4	Schematic illustration of a grain boundary	5
1.5	Dependence of the grain boundary fraction on the grain size	7
1.6	Deformation by dislocations	9
1.7	Schematic illustration of the Hall-Petch relation	10
1.8	Deformation by partial dislocations	11
1.9	Deformation by creep	11
1.10	Possibilities to dissipate stress building up in a triple junction	13
1.11	Grain boundary sliding accommodated by diffusion	13
1.12	Straightening of grain boundaries prior to superplastic flow	14
1.13	Steady state deformation during severe plastic deformation	14
1.14	Schematic illustration of a super dislocation	15
2.1	Diagram of the HPT deformation	19
2.2	Sample before and after HPT deformation	21
2.3	Stress strain curve of the HPT deformation	22
2.4	Images showing the preparation of a TEM sample	23
2.5	Location of different TEM sections in the HPT-disk	24
2.6	Images showing the preparation of a TEM cross-section sample	25
2.7	Schematic diagram representing the diffraction of a plane wave	28
2.8	Imaging using a lens described by the Fourier transform	29
2.9	Interaction of electrons with matter	31
2.10	Sketch of the layout of a transmission electron microscope	34
2.11	Possibilities of increasing the contrast of TEM images	36
2.12	Typical dark-field and bright-field image of nanocrystalline FeAl	37
2.13	Contrast transfer function for a CM30	39
2.14	Map of simulated HRTEM images	40
2.15	The Ewald construction	42
2.16	Diffraction on a small crystallite	47
2.17	Derivation of the Scherrer equation	47
2.18	The Warren-Averbach method	50
2.19	Different measures for the crystallite size	51
2.20	Indexed diffraction pattern of FeAl annealed to 220°C	57

2.21	Diffraction spots in 3D	58
2.22	Microhardness measurement	61
2.23	Schematic representation of a heat flow DSC	62
3.1	Comparison between integral X-ray and local electron diffraction . .	70
3.2	Importance of the resolution of the recording device for profile analysis	71
3.3	Nonlinear effects for diffraction patterns on a film	72
3.4	The importance of using the correct centre of integration	73
3.5	Dependence of the peak height on the deviation from the correct centre	74
3.6	Screenshot of the software PASAD-tools	76
3.7	Menus of the software PASAD-tools	80
3.8	Cropping of the beamstop in PASAD-tools	81
3.9	The centre determination in PASAD-tools	82
3.10	Azimuthal projection calculated by PASAD-tools	82
3.11	A diffraction profile after fitting in PASAD-tools	83
3.12	Adding peaks or splinepoints manually in PASAD-tools	83
3.13	Annotated diffraction pattern created by PASAD-tools	84
3.14	Diffraction pattern reconstruction by dark-field scanning	86
4.1	Evolution of the nanocrystalline structure during HPT deformation .	89
4.2	Diffraction profiles of NC FeAl deformed to different shear strains . .	91
4.3	Williamson-Hall plot of NC FeAl deformed to different shear strains	91
4.4	Diffraction profile and modified Williamson-Hall of NC FeAl	92
4.5	Tangential cross-section of HPT deformed FeAl	95
4.6	The effect of tilting on the measured size for platelet shaped CSD . .	97
4.7	Variation of the volume weighted mean CSD size with the tilt angle	98
5.1	DSC curve of HPT deformed nanocrystalline FeAl	102
5.2	TEM investigations of HPT deformed NC FeAl	104
5.3	TEM of HPT deformed NC FeAl heated to 220°C	104
5.4	TEM of HPT deformed NC FeAl heated to 370°C	105
5.5	TEM of HPT deformed NC FeAl heated to 500°C	105
5.6	Separation of the different processes in the DSC curve	106
5.7	Grain-size histograms of NC FeAl	108
5.8	Evolution of the volume weighted grain size with temperature	109
5.9	HPT deformed FeAl showing small-angle grain boundaries	110
5.10	Deformed FeAl heated to 370°C showing large-angle grain boundaries	111
5.11	Profiles of NC FeAl heated to different temperatures	113
5.12	Evolution of the CSD size with temperature	114
5.13	Variation of the ordered domain size with temperature	114
5.14	TEM study of the ordered domain growth with temperature	115
5.15	HRTEM analysis of nanosized ordered domains	116
5.16	Evolution of different characteristic sizes with temperature	120

5.17	Schematic model for the grain size reduction	121
6.1	Schematic representation of the vacancy diffusion process	124
6.2	Shift of a APB by vacancy diffusion.	126
6.3	Coarsening of the ordered domains by the annihilation of APB . . .	126
6.4	Dependence of the reordering on the vacancy migration enthalpy . .	131
6.5	Dependence of the reordering on the vacancy concentration	132
6.6	Dependence of the reordering on the initial APB boundary density .	133
6.7	Fit of the reordering model to a DSC-curve	134
6.8	Simulated ordered domain size in dependence of temperature	135
6.9	Simulated APB density in dependence of temperature	136
6.10	Fit of the reordering model to a DSC-curve of annealed FeAl	137
6.11	Fit of the reordering model to FeAl annealed under pressure	139
6.12	Determination of the vacancy migration volume	140
6.13	Experiment for studying the effect of unloading after deformation . .	141
6.14	Effect of unloading after deformation on the reordering	143

Outline of this Work

- In chapter 1 the necessary background on the intermetallic compound FeAl including its structure and deformation behaviour is given. Furthermore the main differences in structure and deformation behaviour between coarse crystalline and nanostructured materials are presented.
- Chapter 2 gives a detailed description of the experimental procedures used in this work. This chapter presents both, a short introduction for readers not familiar with the experimental procedures and a detailed description of each experiment presented in this work. A large section is devoted to the determination of microstructural parameters by line profile analysis. Due to the large amount of literature in this field that contains conflicting views, a systematic discussion is presented that starts from the principles of diffraction.
- Chapter 3 contains the development of new TEM methods for analysing nanocrystalline materials. These methods are essential for the quantitative analysis of nanocrystalline materials.
- The nanocrystallisation of FeAl during high pressure torsion deformation is discussed in chapter 4.
- Chapter 5 analyses the processes occurring in FeAl during heating using methods of transmission electron microscopy and differential scanning calorimetry.
- Based on these findings a model describing the reordering behaviour is developed in chapter 6.
- In chapter 7 an overall discussion and conclusions are given.

1 Introduction

“Science may be described as the art of systematic oversimplification.”

– Karl R. Popper

1.1 Chemical Order in FeAl

1.1.1 Phase Diagram

An intermetallic compound is an alloy made of metals including metalloids (e.g. Ge). It appears in the phase diagram as a separate phase within a certain concentration range. In the present work an intermetallic compound made from iron and aluminium is examined. In the phase diagram (cf. Fig. 1.1) the different phases are represented in dependence of the temperature as well as the composition. Fe-45at%Al is studied, since this concentration (indicated by an arrow in the phase diagram) is well inside the range of the intermetallic compound FeAl (indicated as a filled region in the phase diagram).

1.1.2 Chemical Order

In an ordered intermetallic compound, the different elements occupy certain places in the unit cell. In contrast to that, one calls an intermetallic compound disordered if the atoms occupy the places in the unit cell randomly, independent of the element. FeAl is based on the body-centred cubic (bcc) lattice. Ordered FeAl is B2 structured and disordered FeAl is A2 structured (cf. Fig. 1.2) according to the “Strukturbericht” by Ewald and Hermann [Ewald31]. The lattice parameter of FeAl is 0.2907 nm [Kraan86].

In materials science there are different ways to describe order. The short-range order is a measure for the “order” in the surrounding of an atom, i.e. it indicates how strongly neighbouring atoms are correlated. In the case of perfectly ordered FeAl, one Al-atom would have 8 neighbouring Fe-atoms (cf. Fig. 1.2) and in the

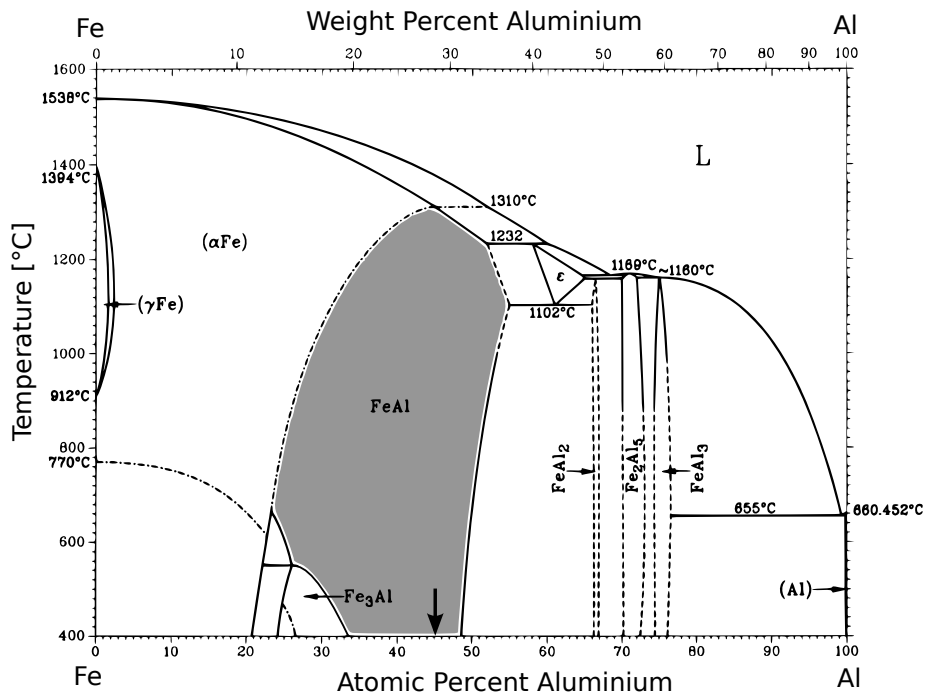


Figure 1.1: Phase diagram of FeAl [Kattner86]. The diagram shows the different phases in dependence of temperature and composition. The region of the intermetallic compound FeAl is filled in the diagram. The arrow indicates the composition (Fe-45at%Al) that was used in the present work.

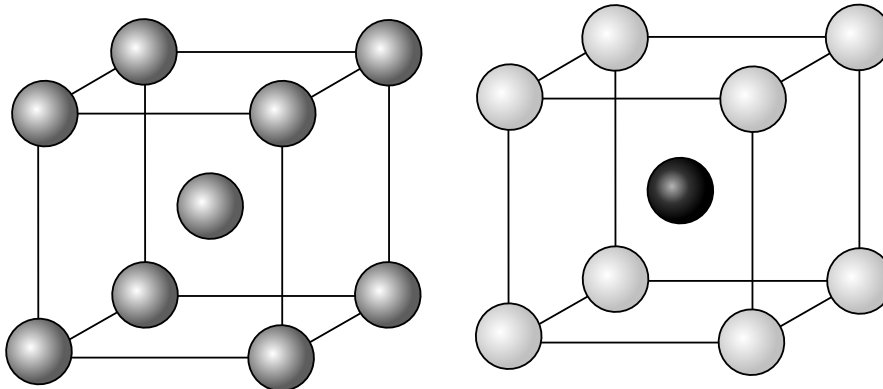


Figure 1.2: Diagram representing the A2-structure (left) and B2-structure (right): The Fe-atoms are represented in black and the Al-atoms in white. A grey atom indicates, that on this lattice place there is an equal probability to find an Fe- or Al-atom.

case of disordered FeAl on average 4 Fe-atoms and 4 Al-atoms. It is also possible to describe the correlation of an atom with its next nearest neighbours or with its m^{th} nearest neighbours. In many materials order extends up to larger interatomic distances in the range of 0.5–2 nm. In this case the order is often called medium range order [Phillips79].

In this work we are specifically interested in long-range order. In an ordered alloy, the different elements are sitting on different lattice positions. The long-range order is essentially a measure for the percentage of atoms that are sitting on the correct lattice positions. The long-range order can be quantified using the order parameter S [Bragg34]. In a perfectly ordered alloy every α atom is sitting at an α lattice position and every β atom on a β lattice position. In general only a certain fraction of α atoms occupies α lattice positions (indicated by $p_{\alpha,\alpha}$). To describe the order parameter we also need the fraction of α atoms in the alloy (A_α) and the fraction of α lattice places (W_α). Analogous expressions for β atoms can also be introduced.

$$S = \frac{p_{\alpha,\alpha} - A_\alpha}{1 - W_\alpha} = \frac{p_{\beta,\beta} - A_\beta}{1 - W_\beta} \quad (1.1)$$

For the case of the $B2$ structure Fe-45at%Al ($W_\alpha = 0.5$, $A_\alpha = 0.45$) the order parameter simplifies to

$$S = 2p_{\alpha,\alpha} - 0.9 = 2p_{\beta,\beta} - 1.1 \quad (1.2)$$

Long-range order can be understood as order extending over the whole material or can prevail in distinct areas, which are then called ordered domains. It is usually demanded that the areas with long-range order extend over at least a few nanometers.

1.1.3 Ordered Domains

Ordered domains are volumes with perfect long-range order. On the one hand an ordered domain can be neighbouring a lattice with different orientation or be surrounded by disordered material and on the other hand ordered domains can be separated by antiphase boundaries (cf. Fig. 1.3). At the antiphase boundaries there is a change of the elements occupying the different sublattices and therefore

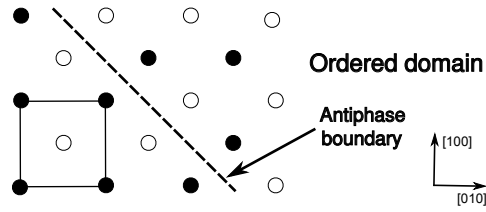


Figure 1.3: Schematic illustration of an antiphase boundary.

the order is disturbed. Antiphase boundaries can be described as the displacement of two parts of the crystal against each other. The corresponding displacement vector in FeAl is $\vec{u} = [111]$. The energy of a APB is $\gamma_{110} = 0.3 \frac{\text{J}}{\text{m}^2}$ [Westbrook00a]. In $L1_2$ ordered Ni_3Al a slight distortion of the lattice was detected in addition to the chemical fault [Rentenberger03].

1.1.4 Thermodynamics of the Ordered State

As the binding energies depend on the configurations of the atoms, intermetallic compounds have a lower free energy in the ordered state than in the disordered state and are therefore normally present in the ordered state. The energy difference between the ordered and the disordered state is called ordering energy. In contrary the configurational entropy is larger for the disordered state and can therefore lead at higher temperatures to a stable disordered state. This phase transition is called order-disorder transition [Haasen86], but it does not occur up to the melting point in FeAl, because of its high ordering energy. The ordering energy in FeAl is estimated to be 6.0 kJ/mol from experimental data and to be 6.62 kJ/mol from theoretical calculations [Qi96].

It should be noted that the ordering energy is defined as the work needed to convert a perfectly ordered alloy into one with a random atomic distribution or as the work required to interchange a correct pair of atoms. It should not be confused with the energy of formation of an ordered alloy phase which represents the energy needed for the transition from the pure constituents to the compound and is much higher than the ordering energy [Bragg35, Cahn02].

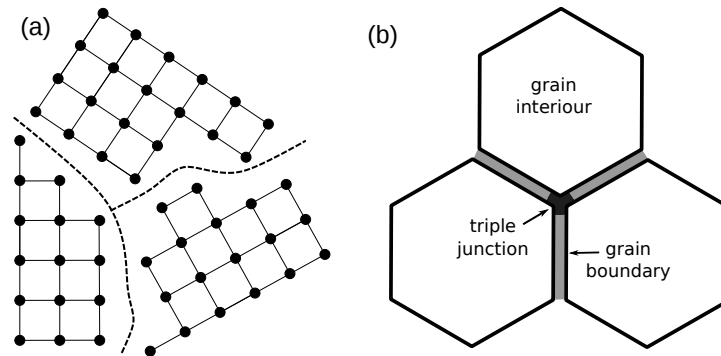


Figure 1.4: (a) A grain boundary is the boundary between crystalline regions having a different orientation. The detailed structure of the grain boundary is omitted. (b) Schematic illustration showing the grain interior, the grain boundaries and the triple junction.

1.2 Structure of Crystalline Materials

1.2.1 Defects

Materials are usually not single crystalline, i.e. they do not represent a perfect periodic lattice. Faults in the lattice are called defects [Kelly00]. The simplest type of defects are the zero-dimensional defects or point defects, which are not extended in space in any dimension. Examples of point defects are vacancies, interstitials and antisites. One dimensional defects are linear distortions of an otherwise perfect lattice. They are called dislocations and are divided into screw dislocations and edge dislocations [Hirth67].

Especially for high deformations at moderate temperatures, it is important to note that screw dislocations of different signs (i.e. having opposite Burgers vectors) can easily annihilate by cross-slip, but edge dislocations that do not lie on the same slip plane have to climb in order to annihilate and can therefore be present in a high density for severely deformed materials [Schafner01].

1.2.2 Grains

Areas within a material having different lattice orientations are called grains (cf. Fig. 1.4). The interfaces are called grain boundaries and can be classified into two types. If the grains are rotated against each other less than $\approx 15^\circ$, they are called small-angle grain boundaries and otherwise large-angle grain boundaries. These

distinction is made because small-angle grain boundaries can be represented as a periodical arrangement of dislocations. For tilted grains, the grain boundary can be represented by edge dislocations and for twisted grains by screw dislocations. Large-angle grain boundaries are more difficult to describe. They can be described by structural units or by using disclinations [Mikaekyan00]. It is important to note that large-angle grain boundaries can act as sources of dislocations [Hurtado95].

In nanocrystalline materials grain boundaries are often present in non-equilibrium conditions. In contrast to coarse crystalline materials, large-angle grain boundaries are frequently high-energy stepped or curved grain boundaries [Huang03] and the grain boundaries have a high excess free volume [Divinski11]. Non-equilibrium grain boundaries are very important for the deformation behaviour of nanocrystalline materials [Nazarov93, Valiev94]. Furthermore triple junctions (regions where three grains intersect, cf. Fig 1.4b) are very important in nanocrystalline materials because they often exhibit a disordered structure, which is to be expected as atoms present in triple junctions are influenced by all three neighbouring grains.

For tetrakaidecahedron grain shapes the volume fraction of grain boundaries and triple junctions can be calculated (d denotes the grain size and w the grain boundary thickness) [Palumbo90]. The results are plotted in Figure 1.5.

$$f_{\text{grain core}} = \left(\frac{d-w}{d} \right)^3 \quad (1.3)$$

$$f_{\text{grain boundary}} = \frac{3w(d-w)^2}{d^3} \quad (1.4)$$

$$f_{\text{triple junction}} = 1 - f_{\text{grain core}} - f_{\text{grain boundary}} \quad (1.5)$$

A term that is very important for diffraction experiments is the coherently scattering domain. Dislocations (cf. chapter 1.2.1) in the grain interior can disturb the periodic structure of the lattice and lead to strain fields and therefore to small orientation changes within the grain. The regions in the grains having the same orientation are called coherently scattering domains, they represent the sizes that are measured when using diffraction (i.e. electron or X-ray diffraction).

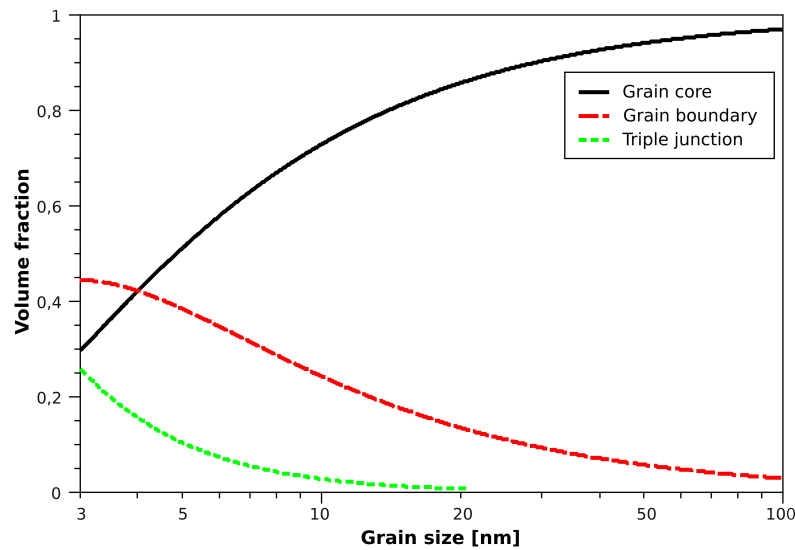


Figure 1.5: Plot of the volume fraction of grain boundaries and triple junctions in dependence of the grain size for tetrakaidecahedron grain shapes and an assumed grain boundary thickness of 1 nm.

1.3 Nanocrystalline Materials

1.3.1 Production of Nanocrystalline Materials

Nanocrystalline materials are defined as materials with a grain size smaller than 100 nm [Gleiter00]. In the last years nanocrystalline materials have attracted increasing scientific interest, as they often exhibit improved mechanical properties with respect to their coarse crystalline counterparts. Especially the combination between high strength with high ductility at room temperature is unique in nanocrystalline materials [Wang02, Zhu04].

Methods of fabrication of nanocrystalline materials can be separated into two categories [Koch06]. In the “bottom up” approach the nanocrystals are built up from atoms. Methods belonging to this category are e.g. “inert gas condensation”, “electrodeposition” or “sputter deposition”. These methods are widely used for the production of thin films or of nanocrystalline powder, but cannot be used for the production of non-porous bulk samples. Furthermore, impurities are often problematic for materials produced using this methods. Bulk samples can be obtained from compacting the powder, which is often done at higher temperatures leading to recrystallisation and therefore to the loss of the nanocrystalline structure.

A second approach which can be used for the production of bulk nanocrystalline materials is the “top down” approach. In these methods coarse crystalline materials are rendered nanocrystalline by “severe plastic deformation” (SPD) [Valiev06a]. Examples of this technique are: Torsion of a material under high pressure – “high pressure torsion” (HPT) [Zhilyaev08]; pressing a material through two channels, that are inclined against each other – “equal channel angular pressing” (ECAP) [Valiev06b]; repeatedly rolling a material and folding it – “repeated cold rolling” (RCR) [Saito98, Wilde05]. An other top-down method is ball milling [Fecht07], but using this method it is not possible to produce in one step bulk specimens. The powder that is obtained has to be compacted leading again to problems with recrystallisation and impurities.

1.3.2 Deformation of Nanocrystalline Materials

Deformation is usually described through dislocations (cf. Fig. 1.6). Slip occurs by the movement of dislocations on glide planes rather than by the rigid displacement over the entire plane. When stress is applied, existing dislocations and dislocations generated by Frank-Read sources will move through the crystal [Hirth67]. A lower density of grown-in dislocations drastically increases the yield strength of a material, as was shown in deformation tests of micropillars [Bei08]. This effect plays an important role in the deformation of nanosized specimens or nanocrystalline materials, where the deformed volume and the dislocation spacing have a similar length scale.

Furthermore it is known that by reducing the grain size d , the yield stress σ increases. This relation is called Hall-Petch and can be described by the following law [Hall51]

$$\sigma \propto d^{-0.5}. \quad (1.6)$$

This dependence is usually analysed in terms of dislocation “pile ups” at grain boundaries. This means that the smaller the grain size the higher the applied stress needed to propagate dislocations through the grain boundaries as less dislocations pile up at the grain boundaries [Pande93]. Other models consider the grain size dependent accumulation of dislocations by intragranular plasticity [Saada05] with the generation of geometrically necessary dislocations [Ashby70].

For grain sizes smaller than about 30 nm a breakdown of this relationship can

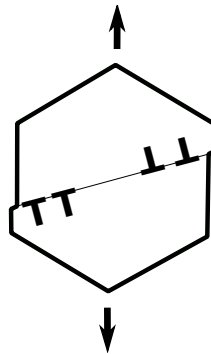


Figure 1.6: Deformation by dislocations. Slip occurs through the movement of dislocations.

be observed that leads to a decrease of the shear strength for decreasing grain size. (The grain size at which this breakdown occurs is strongly dependent on the structure of the nanocrystalline material, e.g. sharp grain boundaries can shift the breakdown to sizes lower than 10 nm [Lu93].) This mechanism is usually called inverse Hall-Petch relation [Carlton07, Chokshi89] (cf. Fig.1.7). It is usually explained by a change in the dominant deformation process. Grain boundary mediated processes start to play a crucial role when grains become sufficiently small and nucleation of dislocations is increasingly difficult [Yamakov04].

Deformation in nanocrystalline materials [Meyers06, Ovidko05, Hemker04] is usually described in four different ways: two-phase-based models, dislocation-based models, diffusion-based models and grain-boundary-shearing models [Carlton07].

Two-phase-based models are based on geometric considerations in terms of the fraction of crystalline and intercrystalline volume, which is often just assumed as amorphous (cf. also Fig. 1.5 and Fig. 1.4) in nanocrystalline materials [Wang95].

The hardness also depends on the glide of a dislocation through a dislocation network. At large spacings of the dislocation network, the critical stress is given by the dislocation cutting mechanism and at smaller spacings by the Orowan bypassing mechanism changing the grain size dependence [Scattergood92]. Furthermore an exact solution to the dislocation pile up in very small grains gives rise to a staircase function deviating from the ideal Hall-Petch behaviour [Pande93].

Partial dislocations are expected to play a crucial effect when the grain size is reduced and the generation of a full dislocation is hindered in the grain (as it has a bigger Burgers vector). A deformation mechanism that is frequently proposed is

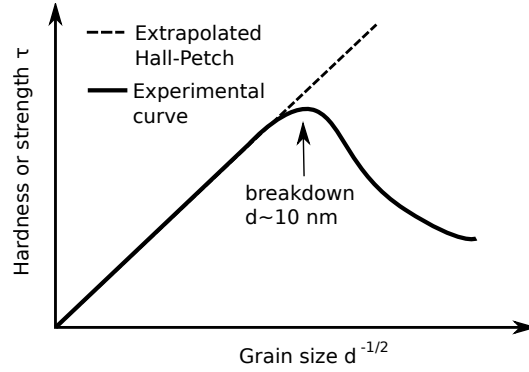


Figure 1.7: Schematic illustration of the Hall-Petch relation. The hardness or strength is proportional to the square root of the inverse grain size. It is experimentally observed that the Hall-Petch relation holds very well for coarse crystalline materials, but breaks down for nanocrystalline materials with very small grain sizes.

the emission of partial dislocations from grain boundaries that run across the grain and are then absorbed into the opposing grain boundary [Hemker04] (cf. Fig. 1.8). This has been shown by molecular dynamic simulations [Swygenhoven02] and has been supported experimentally by the reversibility of the peak broadening using in-situ peak profile analysis of deformed nanocrystalline Ni [Budrovic04] and by the TEM observation of twins and stacking faults (e.g. in nanocrystalline Al [Chen03]).

Twinning is also sometimes put forward as deformation mechanism for nanocrystalline materials [Liao04]. Although deformation twinning is observed in TEM studies of nanocrystalline materials, their density is not high enough to make twinning a dominant deformation mechanism.

For nanocrystalline materials it is expected that deformations tied to diffusion can become important even at low homologous temperatures [Cai99]. To describe creep mechanisms [Meyers06], typically the following dependence of the strain rate ($\dot{\epsilon}$) on the stress (σ) and the grain size (d) is used (where D represents the diffusion coefficient, k_B the Boltzmann constant, T the temperature, n the stress exponent and p the size exponent)

$$\dot{\epsilon} \propto \frac{D}{k_B T} \frac{\sigma^n}{d^p}. \quad (1.7)$$

In Nabarro Herring creep [Herring50] ($D = D_{\text{bulk}}, p = 2, n = 1$) the diffusion occurs through the main body of the grain (cf. Fig. 1.9a). It can be found at higher temperatures. In Coble creep [Coble63] ($D = D_{\text{grain boundary}}, p = 3, n = 1$)

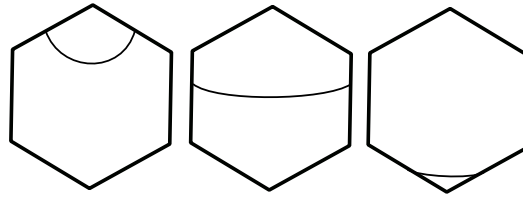


Figure 1.8: Deformation by the emission of partial dislocations. A partial dislocation is emitted from the grain boundary. The partial dislocation runs across the grain and is absorbed in the grain boundary again.

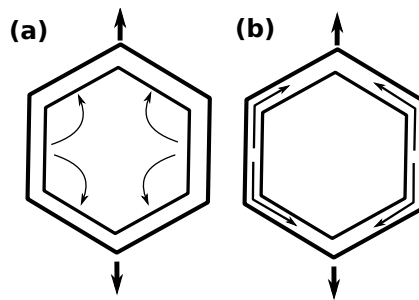


Figure 1.9: (a) In Nabarro-Herring creep the diffusion occurs through the main body of the grain. (b) In Coble creep the diffusion occurs through the grain boundaries.

the diffusion occurs through the grain boundaries (cf. Fig. 1.9b). Due to the lower diffusion constant of grain boundaries it can be activated at lower temperatures. A special case of Coble creep is the triple junction creep ($D = D_{\text{triple junctions}}$, $p = 4$, $n = 1$) which can be activated for very fine grained materials (~ 10 nm), where triple junctions start to make up a significant volume fraction of the material. It is important to note that the diffusivity in triple junctions is much higher than in grain boundaries due to the presence of excess free volumes. In addition to the diffusion driven creep, there is also dislocation creep ($D = D_{\text{self diffusion}}$, $n = 4 - 6$, and $p = 0$) which does not show any grain size dependence.

Superplasticity denotes the ability of a material to undergo a large plastic deformation ($>100\%$) without failure. It has been found in various metals, intermetallic compounds and ceramic systems at homologous temperatures higher than 0.5. In contrast to that superplasticity is observed in nanocrystalline materials at relatively low temperatures [Mukherjee02]. In Ni_3Al with a grain size of 50 nm superplasticity was observed at a homologous temperature of 0.36 [McFadden99].

Superplasticity in nanocrystalline materials can be explained by grain boundary sliding [Padmanabhan04]. Further evidence for grain boundary sliding also comes from molecular dynamic simulations [Swygenhoven99].

Grain boundary sliding [Gifkins67] denotes the relative shear of neighbouring grains against each other localised in the grain boundary. In addition to the grain boundary sliding, a plastic accommodation term has to be added to account for the incompatibility of deformation (cf. Fig. 1.10). Grain boundary sliding can be accompanied by the emission of partial dislocations or by diffusion. Using diffusion through grain boundaries as accommodating mechanism leads to a Coble creep type dependence of the strain rate from the stress [Meyers06, Raj71] (cf. Fig. 1.11). The shear of two grains against each other can also be accommodated by the rotation of a third grain [Wang08]. If the grain boundary sliding is not accommodated, a crack forms.

Padmanabhan [Padmanabhan04] formulated a model in which the grain boundaries are straightened first and then sliding occurs (cf. Fig. 1.12). The rearrangement of the grain boundaries can be based on dislocations or diffusion, and threshold stresses can be worked out for the formation of a plane interface necessary for grain boundary sliding to occur both based on dislocations or diffusion:

$$\sigma_{0,\text{dislocatios}} = 1.42(G\Gamma_B r)^{0.5} \frac{1}{d} \quad (1.8)$$

$$\sigma_{0,\text{diffusion}} = 0.269 \left(\frac{Gk_B T \dot{\epsilon}}{D_{GB} a c_V} \right)^{0.5} d^{0.5} \quad (1.9)$$

where d represents the grain size, σ the stress, ϵ the strain, G the bulk modulus, Γ_B the grain boundary energy, r the residual misfit which results because the initial misfit does not have to be a multiple of the Burgers vector, k_B the Boltzmann constant, T the temperature, D_{GB} the grain boundary diffusion, a the lattice constant and c_V the vacancy density. These equations intersect at some grain size and for smaller grains diffusion based and for larger grains dislocation based grain boundary sliding is dominant. The mesoscopic sliding process is then described by discrete shear events.

It should be noted that in nanocrystalline materials shear localisation in the form of shear bands can occur [Wei02]. Furthermore in nanocrystalline materials stress driven grain boundary migration can be observed [Jin04]. Dynamic recrystallisa-

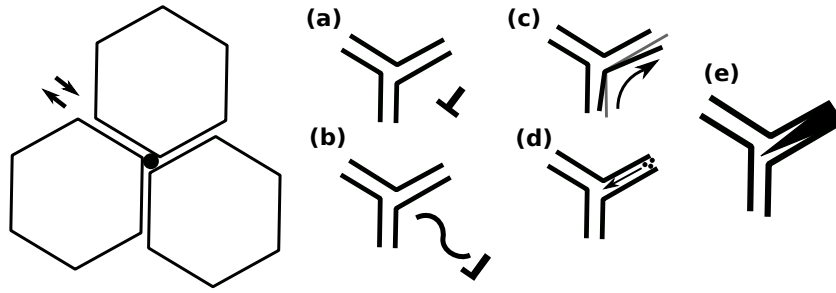


Figure 1.10: When shearing grains against each other stress builds up in the triple junction. There are several ways to dissipate the stress. (a) Emission of a dislocation. (b) Emission of a partial dislocation. (c) Grain rotation. (d) Diffusion of material. (e) If the stress is not dissipated, i.e. if the grain boundary sliding is unaccommodated, a crack forms.

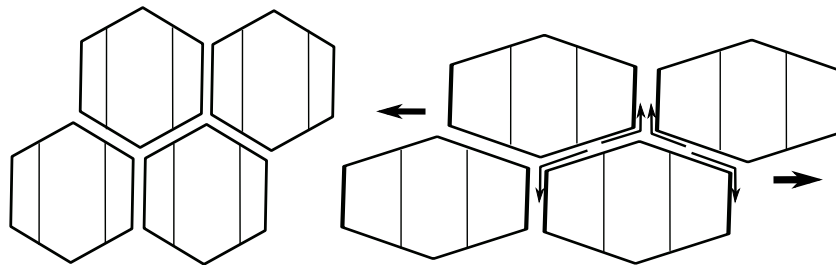


Figure 1.11: Schematic illustration of grain boundary sliding accommodated by diffusion. The grains slide against each other as can be seen from the straight lines drawn on the grains. The grain boundary sliding is accommodated by a flow of material which leads to the elongation of the grains.

tion during deformation can play a crucial role for nanocrystalline materials. This is especially the case for methods of severe plastic deformation, e.g. high pressure torsion deformation (cf. chapter 2.2). In severe plastic deformation the material reaches a final grain size which can be explained in two different ways: (i) the generation of dislocations combined with dynamic recrystallisation [Hafok06, Geist10] as shown in Figure 1.13a or (ii) grain boundary sliding (cf. Fig. 1.13b).

1.4 Mechanical Properties of FeAl

To understand the deformation in a material it is important to consider its slip systems. Slip preferentially occurs along the closed packed directions, which leads for B2 to the following slip systems: $\{110\}\langle 111\rangle$, $\{112\}\langle 111\rangle$ and $\{123\}\langle 111\rangle$

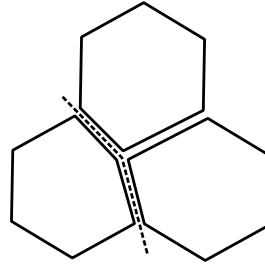


Figure 1.12: Schematic illustration of superplastic flow by grain boundary sliding. The grain boundaries are straightened before grain boundary sliding occurs.

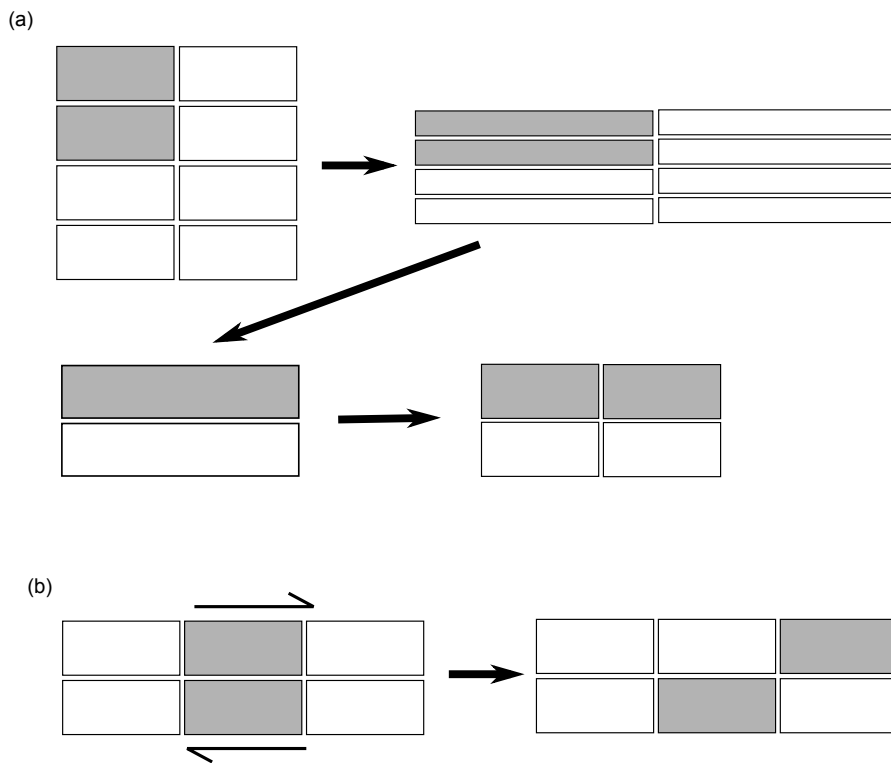


Figure 1.13: Schematic diagram of possible deformation mechanisms explaining why a steady state grain size is reached during severe plastic deformation. (a) The grains are elongated during the shear deformation, dynamic recrystallization leads to the annihilation of grain boundaries in the very thin grains. The generation of dislocations breaks apart the elongated grains forming again the initial configuration. (b) While the grains stay unchanged deformation happens by grain boundary sliding.

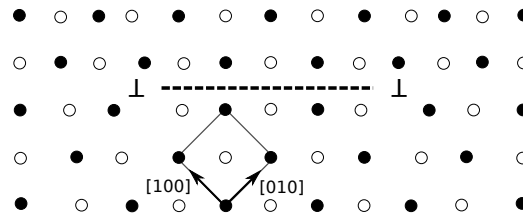


Figure 1.14: Schematic illustration of a super dislocation. Two $\frac{a_0}{2}\langle 111 \rangle$ dislocations carry an antiphase boundary between them.

[Hirth67]. In FeAl slip mainly occurs along the $\{110\}\langle 111 \rangle$ and the $\{112\}\langle 111 \rangle$ systems [Yamagata73]. Two $\frac{a_0}{2}\langle 111 \rangle$ dislocations are favourable to one $a_0\langle 111 \rangle$ dislocation (a_0 denotes the lattice parameter) as they have a smaller energy. These two dislocations have to carry an antiphase boundary between them. This arrangement is called super dislocation (cf. Fig. 1.14). The splitting distance of the dislocations is usually around 2 nm, as in this case the energy is minimised [Wu03].

An other important parameter to consider in deformation is the bulk shear modulus $G = 112$ GPa. The elastic constants of FeAl are summarised in the following table [Sang02]:

$$\begin{aligned} C_{11} & 199 \text{ GPa} \\ C_{12} & 74 \text{ GPa} \\ C_{44} & 91 \text{ GPa} \end{aligned}$$

FeAl is very brittle, especially at low temperatures and with a high Al-content. Ductility for Fe-45at%Al is less than 2%. Fracture usually appears at grain-boundaries. The yield strength is about 400 MPa and Vickers hardness about 300 MPa [Liu98, Deevi96]. In compression tests of single crystalline FeAl pronounced shear banding can be observed [Yamagata73, Yoshimi98].

1.5 Potential Applications of Nanocrystalline FeAl

Intermetallic FeAl has a great potential as a medium to high-temperature structural material. It does not only show good mechanical properties and an excellent corrosion resistance even at high temperatures, but this compound is also extremely light weight and both of the raw materials (Fe and Al) are cheap and abundant. Still for the commercial utilisation of FeAl its poor room-temperature ductility and its poor high-temperature creep-resistance pose a big problem [Sundar03, Westbrook00b].

The utilisation of nanocrystalline FeAl could drastically improve the properties of FeAl. Thus especially bulk nanocrystalline FeAl is a promising candidate for the replacement of iron-base and nickel-base superalloys.

1.6 Previous Work

1.6.1 HPT Deformation of Intermetallic Compounds

The greatest amount of work on the production of nanocrystalline structures using HPT has been focused on pure metals [Zhilyaev08]. When looking at the HPT deformation of intermetallic compounds, some work on the shape-memory alloy NiTi can be found (e.g. [Peterlechner09b]). A lot of work is focused on L1₂ structured compounds (e.g. Cu₃Au [Rentenberger08] and Ni₃Al [Rentenberger05]). Significantly less work can be found on B2 structures as they usually have a much higher intrinsic brittleness (e.g. TiAl [Korzniakov99]). In general a chemically disordered nanocrystalline structure results from the HPT deformation of intermetallic compounds.

1.6.2 Ball Milling of FeAl

Ball milling has been used for the deformation of a large range of intermetallic compounds, as it also allows the deformation of very brittle compounds. Still a major disadvantage over HPT deformation is the presence of impurities which can strongly influence the results. Furthermore to obtain a compact specimen the powder has to be pressed under elevated temperatures leading to an increased grain size. Similarly to HPT deformation, the formation of the nanocrystalline structure during ball milling is accompanied by loss of the long-range order [Bakker95]. For B2-ordered FeAl, both the disordering by ball milling and the subsequent reordering during annealing has been studied using different integral methods, like differential scanning calorimetry, X-ray and neutron diffraction, as well as magnetometer measurements [Hernando98, Amils99, Varin99, Amils01, Gialanella98, Zeng06, Amils00].

2 Experimental Procedure

*“A theory is something nobody believes, except the person who made it.
An experiment is something everybody believes, except the person who
made it.”*

– Albert Einstein

2.1 Production of the Raw Material

Fe-45at.%Al was alloyed at the Department of Solid State Physics at the Technical University of Vienna from high purity Fe (99,99 %) and Al (99,9997 %) using the cold boat technique under argon atmosphere. Single crystals were grown in our lab from the alloyed compound under vacuum in alumina crucibles. A modified vertical Bridgman technique was used, where the crucible used for single crystal growth remained fixed and the furnace was moved [Fischer76]. The single crystals were grown at a speed of 10 mm/h at 1460°C under vacuum ($<10^{-6}$ mbar). In order to maximise the long-range order and to minimise the vacancy concentration, the Fe-45at.%Al single crystals were annealed for one week at 400°C under vacuum ($<10^{-6}$ mbar) [Xiao95].

To check the quality of the single crystal growth, the top and the bottom of one sample were cut off by spark erosion, grinded and polished and then etched for 30 s using the Keller etching solution [Schumann91]. This solution consists of 2 ml hydrofluoric acid, 3 ml hydrochloric acid, 5 ml nitric acid and 10 ml aqua dest. Optical microscopy inspection of the etched surface revealed an uniform brightness and no grain boundaries, thus indicating the good quality of the single crystal.

Furthermore the composition of all FeAl single crystals was analysed on a Zeiss Supra 55 VP scanning electron microscope equipped with energy-dispersive X-ray spectroscopy (Oxford INCA) present in our faculty. The composition of Fe and Al content was measured several times in the top and bottom slices of the single

crystals leading to the conclusion, that the deviation of composition between the top and bottom of the single crystals was less than 2 at.%.

Finally the orientation of all single crystals was measured using the back-reflection Laue method. In this method a film-plate is placed between the X-ray source and the sample. The beam emitted from the X-ray source passes through a hole in the film and hits the sample. The beams that are diffracted from the sample hit the film forming a spot pattern. From the spot pattern the orientation of the crystal can be deduced. Laue images were taken on a W-anode line using an acceleration voltage of 22 kV on a device present in our group. The distance between sample and film was chosen to be 30 mm. To evaluate the orientation the QxLaue Software was used [QxLaue].

2.2 High Pressure Torsion

2.2.1 Illustration of the HPT Deformation

During the high pressure torsion (HPT) deformation [Bridgman43, Zhilyaev08] a coin-shaped sample is pressed between two steel anvils having a cavity so that a quasi-hydrostatic pressure acts on the sample. The anvils are rotated against each other leading to a plastic deformation of the sample (cf. Fig. 2.1). The shear strain depends on the thickness of the sample d and the number of turns N . It is not homogeneous across the sample, but increases with increasing radius R . As the shape of the sample stays constant during deformation, very high deformations (up to 100,000 %) can be achieved by HPT. The shear strain can be calculated using the following formula [Schrivastava82]

$$\gamma = \frac{2\pi NR}{d}. \quad (2.1)$$

2.2.2 HPT Deformation of FeAl

From the FeAl single crystal, which was approximately 30 mm long and had a diameter of 10 mm, disks with a thickness of 0.8 mm were cut using spark erosion. Spark erosion was carried out in our lab using a Charmilles Isopulse P25 device. From the disks the HPT samples were punched-out by spark erosion leading to HPT-samples with a diameter of 8 mm (cf. Fig. 2.2a). For an improved second

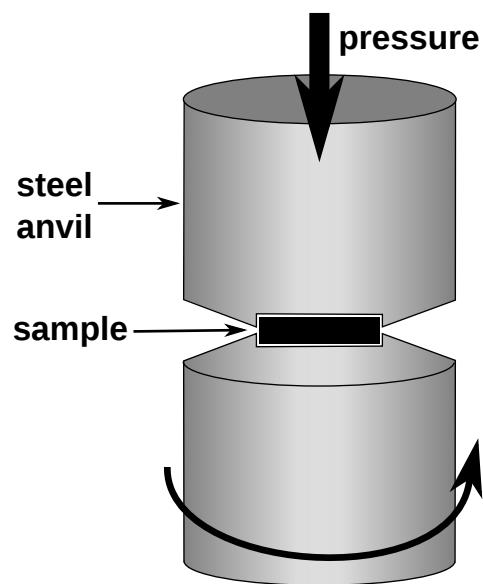


Figure 2.1: Schematic diagram of the HPT deformation. A coin-shaped sample is pressed under high pressure between two steel anvils. The anvils are rotated against each other leading to the deformation of the sample.

generation of samples, disks with a diameter of 6 mm were punched-out and embedded in a 1 mm steel ring leading again to a sample with a diameter of 8 mm (cf. Fig. 2.2b). The ring was used to improve the deformation behaviour, as in the first generation of samples the FeAl disks were often cold welded to the steel anvils at the edge of the cavity due to the high pressure.

The samples were grinded and sand-blasted in order to remove impurities coming from spark erosion and above all to enhance the surface roughness and thus preventing the sample from slipping during deformation. The friction between sample and anvil was further improved by sand blasting the anvils after every deformation. To detect any slipping during deformation (i) the samples were marked with a fineliner on the lower and upper surface (cf. Fig. 2.2) and (ii) the torque was recorded. The shape of the torque curve gives information on the quality of the HPT deformation, as slipping, misalignment or cold welding of the anvils can be easily detected. A typical curve is shown in [Gammer11d].

The HPT deformation was performed at room temperature using a pressure of 8 GPa and a speed of 0.2 turns per minute, which corresponds to a maximum deformation rate of $\dot{\gamma} \approx 0.1$. From the recorded torque curve the stress-strain dependence can be calculated. Figure 2.3 shows that the stress saturates at strain $\gamma \approx 50$ reaching a plateau stress $\tau = 1.2$ GPa.

Figure 2.2c shows a HPT sample after deformation. Due to the high pressure during the deformation some of the material is pressed out of the cavity in the anvil. Since FeAl is very hard and brittle, this portion is small and leads to a thickness reduction of approximately 10%.

2.3 Preparation of the TEM Samples

2.3.1 Preparation of Plan-View TEM Samples

For the TEM investigations disks with a diameter of 2.3 mm were cut from the outer rim of the HPT disk using spark erosion (cf. Fig. 2.4c). The HPT samples were marked in radial direction using spark erosion in order to be able to correlate TEM investigations with the shear direction (cf. Fig. 2.4a). The TEM samples were thinned to approximately 0.15 mm thickness by mechanical grinding. Using an electropolishing equipment of the type Struers Tenupol 3 present in our lab, the samples were further thinned using as electrolyte methanol with 33 % nitric acid cooled to a temperature of -25°C [Yoshimi98]. The equipment was adjusted in

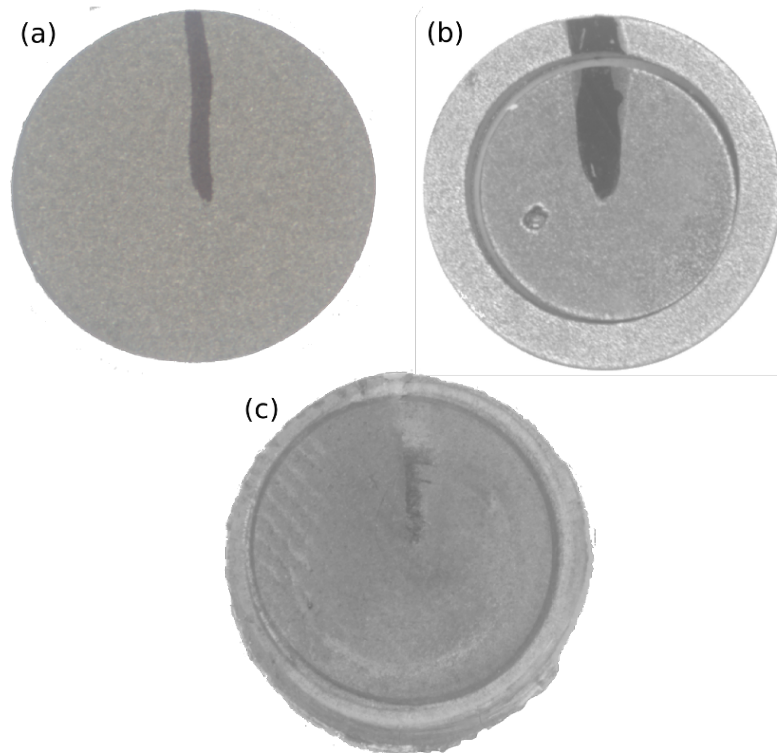


Figure 2.2: (a) FeAl sample before HPT deformation. (b) FeAl sample embedded in a steel ring before HPT deformation and (c) after deformation. The marks can be seen clearly, indicating the sample did not slip during deformation. All samples had a diameter of 8 mm and a thickness of about 0.8 mm before and of about 0.75 mm after HPT deformation.

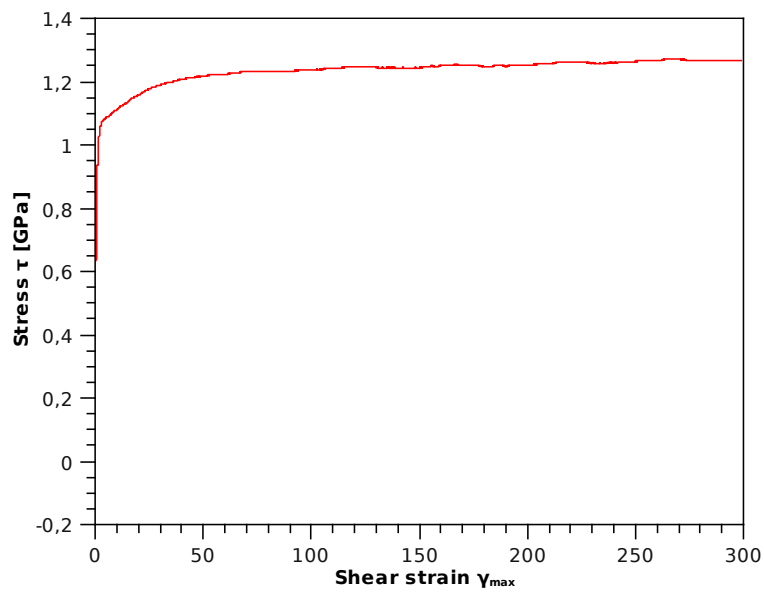


Figure 2.3: Stress strain curve of the HPT deformation calculated from the torque measured during the deformation. The sample shows hardening and saturates after around half a rotation, corresponding to a strain of ≈ 50 , at a stress-value of about 1.2 GPa.

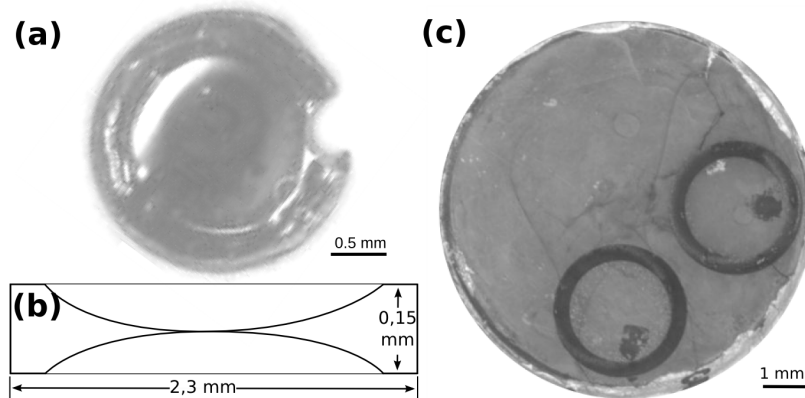


Figure 2.4: (a) Image of a TEM sample prepared by electropolishing recorded with an optical microscope. The sample shows a mark at the edge indicating the radial direction. Around the hole the sample is sufficiently thin for the TEM-investigations. (b) Schematic illustration of a TEM sample prepared by electropolishing. (c) Areas of the HPT disk from where the TEM samples were cut out.

such a way, that polishing was terminated with the first occurrence of a hole in the sample. Electropolishing usually lasted approximately 5 minutes. The tension was set to 4 V, the current was measured and was usually around 50 mA. Figure 2.4b shows a schematic representation of a prepared TEM sample. Around the hole, the sample is sufficiently thin for TEM investigations (≈ 50 nm).

2.3.2 Preparation of Cross-Section TEM Samples

Especially in the case of samples made by HPT most TEM investigations are based on plan-view samples only (cf. Fig. 2.4c), probably due to experimental difficulties in preparing cross-section TEM specimens of the rather thin HPT disks. Still, when analysing nanocrystalline structures with non-equiaxed grains or non-homogeneous structures, the analysis of different TEM sections is necessary [Huang07, Peterlechner09b]. Therefore, in addition to conventional plan-view TEM samples (cf. Fig. 2.4c), various cross-section samples were cut from the HPT disk (cf. Fig. 2.5).

The preparation of the cross-section TEM samples was done by electropolishing. As the HPT disk has a height of ~ 0.7 mm only, the cross-section sample had to be put between dummy material prior to electropolishing. In the first step, a thin stripe was cut out of the HPT disk using spark erosion. The location of the stripe

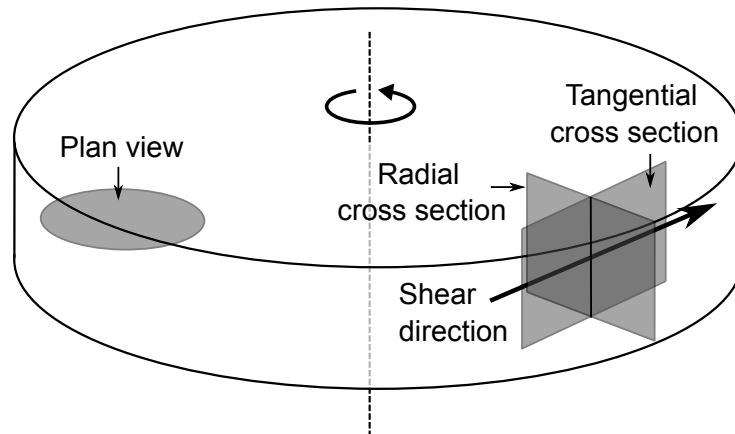


Figure 2.5: Sketch showing the location of different TEM sections in the HPT-disk. The plan view (or top view) sample lies horizontally in the HPT-disk, the tangential cross section contains the shear direction and has its plane normal parallel to the radial direction, the radial cross section contains the radial direction and has its plane normal parallel to the shear direction.

for different cross-sections is indicated in Figure 2.5. The stripe was laid down and put between two stripes of dummy material. As dummy material remainders of a FeAl single crystal were used. A disk with a diameter of 2.3 mm was punched out from the stripes using spark erosion so that the sample stripe was in the middle of the disk. (It is recommended to release the electrolyte first and then retract the pipe that is used for punching as otherwise the small stripes will get lost. This is achieved by turning of the main switch of the spark erosion machine while punching.) For stability reasons the stripes were glued together and glued into a brass ring using a very thin layer of conducting epoxy glue (cf. Fig. 2.6a). For the electropolishing process a conducting glue had to be used. The resulting “sandwich” sample was thinned to approximately 0.15 mm thickness by mechanical grinding. In order to ensure that the hole forms in the sample and not the dummy material, the sample was dimpled from both sides reaching a final thickness of approximately 0.05 mm (cf. Fig. 2.6b). The electropolishing was performed in the same way as for the plan-view TEM samples (cf. chapter 2.3.1).

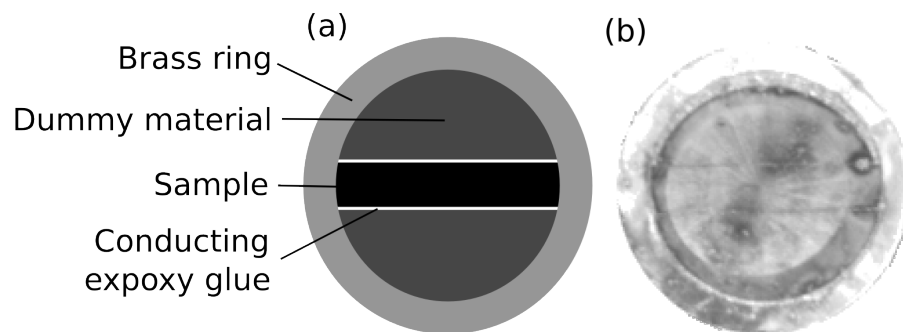


Figure 2.6: (a) Schematic drawing showing a “sandwich” sample that can be used to prepare TEM cross-sections by electropolishing. The desired cross section sample is glued between two stripes of dummy material (in this case single crystalline FeAl) and glued into a brass ring for stability reasons. To allow electropolishing a conducting epoxy glue was used. The sample is then thinned to 0.15 mm and dimpled from both sides to 0.05 mm. An image of the resulting “sandwich” sample is shown in (b).

2.4 Diffraction and Imaging as Fourier Transforms

Before starting the chapters about transmission electron microscopy and diffraction, the basics of diffraction and imaging are discussed. A unified treatment of diffraction and imaging using only the Fourier transform is developed.

Irrespective whether light, X-ray, electrons or neutrons are used for imaging, they can be described using waves [Cowley95, Goodman05, Warren90]. Two special kinds of waves are of importance

$$\psi(\vec{x}, t) = \psi_0 \exp(i(\omega t - k\vec{n}_0 \cdot \vec{x})), \quad (2.2)$$

which represents a plane wave travelling in the direction of the unit vector \vec{n}_0 at the position \vec{x} and

$$\psi(r, t) = \psi_0 \exp\left(\frac{i(\omega t - kr)}{r}\right), \quad (2.3)$$

the spherical wave radiating from the origin at a radius r ($k = \frac{2\pi}{\lambda}$ denotes the wave number and ω is the angular frequency). Other waves can be constructed by superposition (which is a simple addition of the wave functions). It is important to note that what is actually measured is the intensity of the wave which is given by

$$I = |\psi|^2 = \psi^* \psi. \quad (2.4)$$

This gives rise to the interference of waves and implies that the phase is lost in the measurement of the wave.

Consider first the diffraction of a parallel beam of radiation on a sample ($\psi_{\text{in}}(\vec{x}) = \psi_0 \exp(ik\vec{n}_0 \cdot \vec{x})$). For simplification it will be assumed that the distance at which the diffracted radiation is studied is large in comparison to the dimension of the specimen (Fraunhofer far-field approximation) and that diffracted beams will not be diffracted again (kinematic theory). Furthermore we consider elastic scattering only, i.e. scattering where the energy is conserved. The specimen can be described by a 3D function describing the scattering power ($f_{\text{sample}}(\vec{x})$), e.g. the electron density in X-ray diffraction or the electrostatic potential for electron diffraction. Every point of the specimen gives rise to a spherical wave (Huygens principle [Huygens90]) which is proportional to the scattering power at this specific point of the sample \vec{x}

(cf. Fig. 2.7). At the position of observation (\vec{R}) the diffracted radiation is

$$\psi(\vec{R}) = f(\vec{x})\psi_0 \exp(ik\vec{n}_0 \cdot \vec{x}) \frac{\exp(ik|\vec{R} - \vec{x}|)}{|\vec{R} - \vec{x}|}. \quad (2.5)$$

To get the whole diffracted intensity it is necessary to integrate over the whole sample. Furthermore we apply the following far-field approximation

$$\frac{\exp(ik|\vec{R} - \vec{x}|)}{|\vec{R} - \vec{x}|} \approx \frac{\exp(ikR)}{kR} \exp(-ik\vec{n} \cdot \vec{x}), \quad (2.6)$$

where R denotes the magnitude of \vec{R} and \vec{n} the normal vector in direction of \vec{R} . The approximation is valid as we assumed that $x \ll R$. Thus we receive

$$\psi_{\text{dif}}(\vec{R}) \propto \int_{\mathbb{R}^3} f_{\text{sample}}(\vec{x}) \exp(ik(\vec{n} - \vec{n}_0) \cdot \vec{x}) d\vec{x}. \quad (2.7)$$

Usually the scattering vector $\vec{g} = \frac{k}{2\pi}(\vec{n} - \vec{n}_0)$ is used (crystallographers convention) leading to

$$\psi_{\text{dif}}(\vec{g}) = \frac{\exp(ikR)}{kR} \int_{\mathbb{R}^3} f_{\text{sample}}(\vec{x}) \exp(-2\pi i\vec{g} \cdot \vec{x}) d\vec{x}. \quad (2.8)$$

Thus the mathematical basis of the kinematic theory of diffraction is the Fourier transform [Goodman05]

$$\psi_{\text{dif}}(\vec{g}) \propto \mathcal{F}[f_{\text{sample}}(\vec{x})]. \quad (2.9)$$

Still it is important to note that there is a significant difference between the Fourier transform and diffraction, in the case of diffraction \vec{g} can not take any values in \mathbb{R}^3 but is limited to the difference between two unit vectors times the wave number (as we are in the far field only the direction matters and not the distance). This is the basis of the Ewald construction (cf. chapter 2.5.3).

Thus we can make use of the vast methodology that has been developed for the Fourier transformation [Gammer07, Stein75] including the following properties:

- The Fourier transform is unique and has an inverse.
- Symmetry: $\mathcal{F}\mathcal{F}[f(x)] = f(-x)$.
- Linearity: $\mathcal{F}[a_1f_1(x) + a_2f_2(x)] = a_1\mathcal{F}[f_1(x)] + a_2\mathcal{F}[f_2(x)]$.

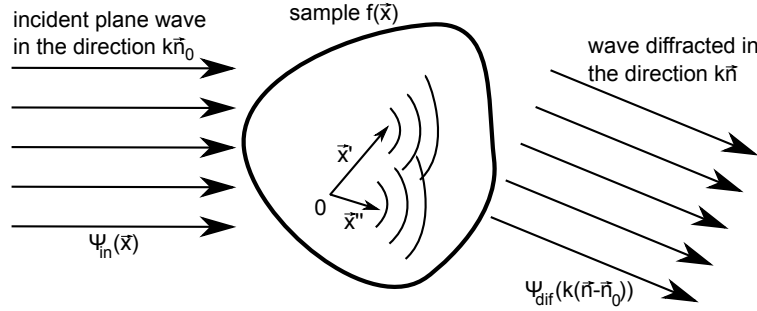


Figure 2.7: An incident plane wave travelling in the direction \vec{n}_0 hits a sample. Every point of the sample emits a spherical wave, that depends on the scattering power of the sample at this position $f(\vec{x})$. The wave detected in the far field in the direction \vec{n} is determined by the Fourier transformation of the scattering power of the sample.

- Friedel's law states that symmetry or anti-symmetry is preserved by the Fourier transform.
- The convolution theorem is the most useful property of the Fourier transform: $\mathcal{F}[f_1 \otimes f_2] = \mathcal{F}[f_1]\mathcal{F}[f_2]$.
- The Parseval theorem implies the conservation of the norm upon Fourier transform and thus the conservation of the radiation in diffraction.

Now consider a lens as the simplest imaging system (cf. Fig. 2.8). The object exit wave $\psi_0(x,y)$ will pass through the lens and form a diffraction pattern in the back focal plane $\mathcal{F}[\psi_0]$ (the back focal plane corresponds to an infinite distance and thus the far-field approximation is perfectly applicable). It is enough to consider the two-dimensional case as we will not be able to get a 3D image. The diffraction pattern will be again Fourier transformed forming an image $\psi = \mathcal{F}\mathcal{F}[\psi_0]$. The resulting image is identical with the object exit wave, but it will be inverted resulting from the symmetry property of the Fourier transformation (the image will be also magnified by a factor $\frac{d_2}{d_1}$ because the relevant variable for the 2D Fourier transform is $\tilde{x} = \frac{x}{d}$). Let us now consider an imperfect optical system, the diffracted beams are influenced (usually beams with a higher spatial frequency g are influenced more strongly), which is expressed by the optical transfer function $T(g)$, which leads to the following

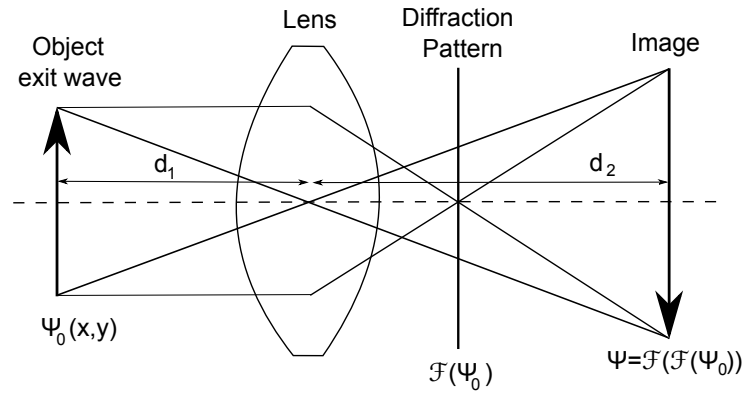


Figure 2.8: This sketch shows how imaging using a single lens can be described by the Fourier transform. The diffraction pattern formed in the back focal plane corresponds to the Fourier transform of the object exit wave. A second Fourier transform forms the image.

expression for the “disturbed” diffracted beams:

$$\mathcal{F}[\psi_0](g)T(g). \quad (2.10)$$

Thus (apart from the magnification) by the convolution theorem we get

$$\psi(x,y) = \psi_0(x,y) \otimes t(x,y), \quad (2.11)$$

where $t(x,y)$ is defined as the inverse Fourier transform of $T(g)$.

2.5 Transmission Electron Microscopy¹

2.5.1 Electron Waves and Lenses

In an electron microscope electrons instead of light are used for imaging. To understand all the modes of the TEM it is important to take a look at the interaction of electrons with matter (cf. Fig. 2.9). When an incident beam of electrons interacts with a thin sample, some electrons are elastically scattered (diffracted beam) and some electrons pass the material (transmitted beam). These beams can be used for diffraction and conventional imaging in the transmission electron microscope (TEM). Electrons that are inelastically scattered are used in electron energy loss spectroscopy (EELS). One form of inelastic scattering is the inner-shell ionizations and can be used for a determination of the atomic composition. Furthermore inelastically scattered electrons give rise to Kikuchi-lines. Atoms emit characteristic X-rays which are used in the TEM for composition measurements (EDX). In the scanning electron microscope (SEM) the sample does not have to be electron transparent as not transmitted but backscattered electrons are used for imaging. Secondary electrons are used for topographic contrast and backscattered electrons for a contrast that depends on the atomic number.

A TEM of the type Philips CM200T (capable of reaching an acceleration voltage of 200 kV) was used for conventional electron microscopy and an electron microscope of the type Philips CM30ST (capable of reaching an acceleration voltage of 300 kV) for the high resolution transmission electron microscopy, both equipped with a LaB₆-cathode. Both microscopes are present in our labs. The wavelength of an electron [Broglie25, Davisson27] results from the deBroglie Wavelength,

$$\lambda = \frac{h}{m_e v} \sqrt{1 - \frac{v^2}{c^2}}, \quad (2.12)$$

where v represents the speed and m_e the rest mass of the electron (h denotes the Planck constant and c the speed of light). As fast electrons have a much shorter wavelength than light, it is possible to achieve higher resolutions than in a light microscope.

Instead of glass lenses in the electron microscope magnetic lenses are used. Enlargement is based on the Lorenz-force acting on moving electrons. Electron lenses

¹A more detailed introduction to electron microscopy can be found for example in [Williams96, DeGraef03, Fultz05, Reimer08].

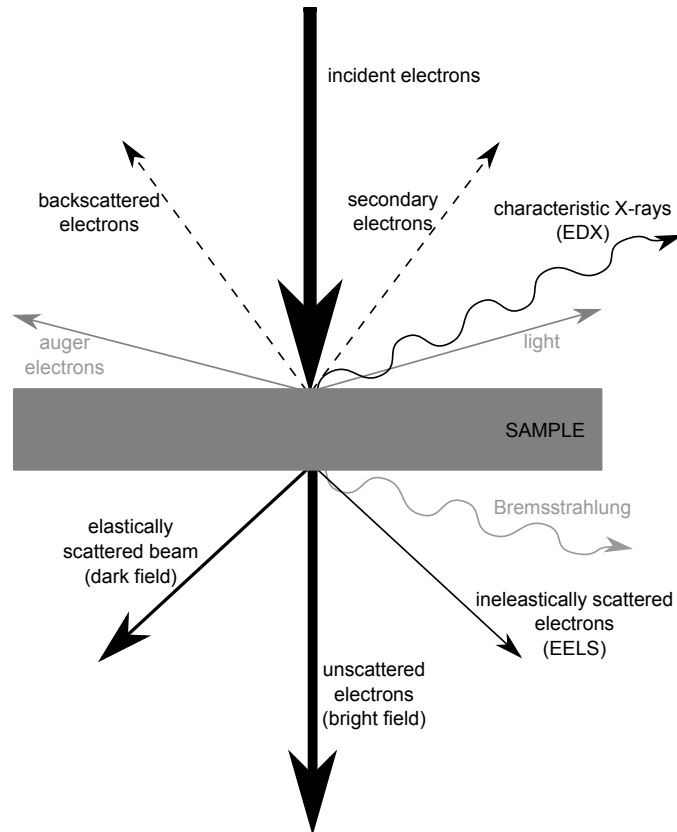


Figure 2.9: This figure shows the interactions of electrons with matter. The dashed lines represent the interactions that are used for imaging in SEM. The characteristic X-rays can be used for composition measurements (SEM+TEM). Elastically scattered and unscattered electrons are used in TEM for imaging and diffraction. Inelastically scattered electrons carry a lot of information (e.g. chemical composition) that can be exploited in EELS. The grey lines represent interactions that are rarely used in electron microscopy.

contain many aberrations. The aberration function χ of a lens can be described using the even Zernike polynomial (g denotes the modulus of \vec{g} and ϕ its angle)

$$\chi(g, \phi) = \frac{2\pi}{\lambda} \sum_{m \geq n \geq 0, m \in 2\mathbb{N}} w_{nm} \frac{(\lambda g)^n}{n} \cos(m(\phi - \phi_{nm})), \quad (2.13)$$

with aberration coefficients w_{nm} where $n - 1$ denotes the order of the aberration and m its symmetry [Born80]. The following table gives a summary of the most important coherent aberrations. As for electron lenses usually a slightly different notation is used [Uhlemann98], this is also added in the table:

aberration name	w_{nm}	TEM notation
First order aberrations		
defocus	w_{20}	Z (or Δ)
twofold astigmatism	w_{22}	A ₁
Second order aberrations		
axial coma	w_{31}	3B ₂
threefold astigmatism	w_{33}	A ₂
Third order aberrations		
spherical aberration	w_{40}	C _s
star aberration	w_{42}	4S ₃
fourfold astigmatism	w_{44}	A ₃

In addition to these aberrations there are also the incoherent aberrations that lead to a damping (these are the chromatic aberration and time-dependent perturbations). Most aberrations can be corrected for, but the spherical aberration is very difficult to correct for and is thus the limiting factor in most transmission electron microscopes. The ray aberrations can be deduced from the wave aberrations by differentiation [Born80], therefore the limiting resolution due the spherical aberration becomes

$$d_s = C_s \cdot \alpha^3, \quad (2.14)$$

whereby C_s is the constant of the spherical aberration and α ($= \lambda g$) the aperture angle. The limiting resolution due to the wavelength of the electrons after Abbe [Abbe1873] is

$$d_b = \frac{0.61\lambda}{\sin \alpha}. \quad (2.15)$$

The minimum of the sum $d_s + d_b$ defines the resolving power of the microscope, which is approximately 0.2 nm for the Philips CM200T and approximately 0.17 nm for the Philips CM30ST. Lately C_s -corrected microscopes became widely available reaching values smaller than 0.05 nm [Nellist04, Dahmen09].

In addition to the instrumental resolution (d_i), the resolution is further reduced by the resolution governed by noise

$$d = \sqrt{d_i^2 + d_{\text{noise}}^2} \quad (2.16)$$

$$d_{\text{noise}} = \frac{SNR_{\text{lim}}}{C\sqrt{D}} \quad (2.17)$$

where D denotes the dose and C the contrast and SNR the signal to noise ratio.

2.5.2 Schematics of a TEM

A schematic representation of a TEM can be found in Figure 2.10. The imaging mode is illustrated in Figure 2.10a. The condenser-lens focuses the electron-beam on the sample. Using the condenser aperture, only rays close to the optical axis are selected as beams far away from the optical axis give rise to large aberrations. The objective lens creates a magnified image, which is then further magnified by a set of projector lenses. In the back focal plane of the objective-lens the objective aperture can be inserted to select which beams contribute to the image formation.

2.5.3 Diffraction

A great strength of TEM is the ability to switch between imaging mode and diffraction mode. Figure 2.10b shows a TEM operating in diffraction mode, where the intermediate lens is focused on the back-focal plane of the objective-lens, thus showing a diffraction pattern on the screen. In the image-plane of the objective-lens the selected area aperture can be inserted, which acts as a virtual aperture on top of the sample. Using this aperture it is possible to take diffraction patterns of areas selected in the imaging mode. For this reason the diffraction mode is usually referred to as selected area electron diffraction (SAD).

Crystalline samples only allow diffraction in specific directions θ , which can be determined using Bragg's law

$$2d_{hkl} \cdot \sin \theta_{hkl} = n \cdot \lambda \quad (2.18)$$

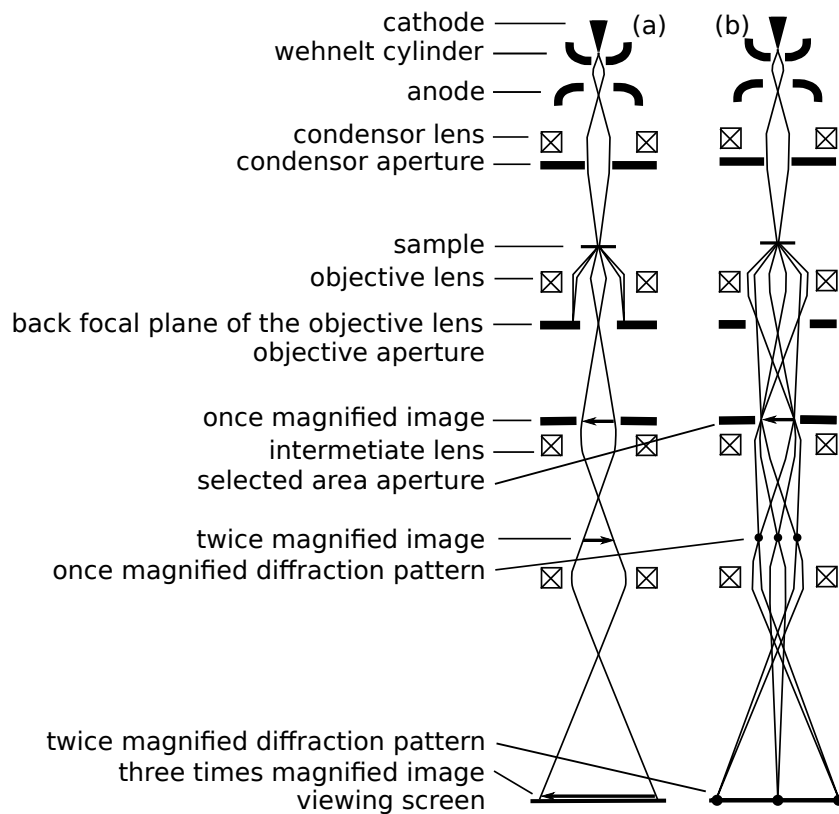


Figure 2.10: Sketch of the layout of a transmission electron microscope. (a) In the imaging mode a magnified image of the sample is projected on a screen. (b) In the diffraction mode the back focal plane of the objective lens is magnified on the screen, showing a diffraction pattern.

whereby n is an integer, λ represents the wavelength and d the lattice spacing. The lattice spacing can be calculated for a cubic lattice with lattice constant a

$$d_{hkl} = \frac{a}{\sqrt{h^2 + k^2 + l^2}}, \quad (2.19)$$

whereas h, k, l represent the Miller indices.

For small diffraction angles 2θ , the sinus of the angle can be approximated by the angle

$$n \cdot \lambda = d_{hkl} \cdot 2\theta = 2 \frac{G}{2L} \quad (2.20)$$

L represents the camera length and G the distance of the diffraction spot to the central beam. This leads to the following equation, which can be used to index reflections in a diffraction pattern

$$\lambda L = G \cdot d_{hkl}. \quad (2.21)$$

For a more advanced treatment of diffraction refer to chapter 2.6.

2.5.4 Contrasting

To improve the contrast of an image in the TEM, the objective aperture can be inserted to select which beams contribute to the image formation. For bright-field images only the central beam is selected and for dark-field images only diffracted beams are selected (cf. Fig. 2.11a,b). Lens aberrations increase drastically for beams far from the optical axis, therefore in the dark-field image the objective aperture is kept on the optical axis, and the incoming electron beam is tilted to select a diffracted beam (cf. Fig. 2.11c).

For crystalline samples, the intensities of the central and diffracted beams depend on the local orientation of a crystal. Also defects lead to a local distortion of the crystal lattice and therefore to a local change of the intensities. These effects lead to spatial intensity variations in dark- and bright-field images called diffraction-contrast. Besides the diffraction contrast there are also the thickness contrast (i.e. the contrast depends on the thickness of the sample) and the mass contrast (i.e. areas with heavier elements act as thicker regions). These contrasts arise from incoherent scattering of electrons. For thin crystalline samples, the diffraction contrast plays the most important effect.

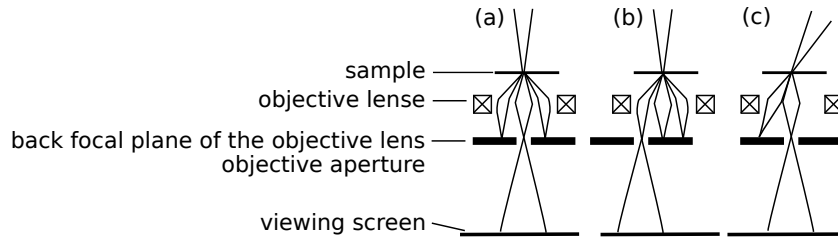


Figure 2.11: Schematic representation of the possibilities to increase the contrast in TEM images. (a) In the bright-field image, the transmitted beam is selected. (b) In the dark-field image a diffracted beam is selected. (c) To increase the image quality, rather than moving the aperture, the incoming beam is tilted.

Figure 2.12a shows a typical dark-field image and 2.12b a typical bright-field image of nanocrystalline FeAl. Especially in the bright-field image it is clearly visible that the contrast is very complex due to the overlapping of grains and the very high defect density present in nanocrystalline materials [Rentenberger04]. An exact analysis of the defect and grain structure is therefore very difficult. From the dark-field images grain sizes and domain sizes can be estimated.

2.5.5 HRTEM

In contrast to dark- or bright-field imaging (cf. chapter 2.5.4) in high resolution transmission electron microscopy (HRTEM) no aperture or a very large aperture is used. Thus the central and the diffracted beams interfere forming an image that contains information on the atomic structure of the material making it possible to measure inter-atomic distances, determine the atomic structure, visualise single defects or investigate the structure of interfaces. In contrast to conventional TEM which is based on amplitude changes (e.g. diffraction-contrast or thickness-contrast), in HRTEM the phase shift induced by the specimen is used for the image formation, i.e. HRTEM is a phase-contrast microscopy method.

Consider a crystal oriented in zone-axis, then the specimen consists of columns of atoms. If the sample is thin the incoming plane wave interacts with the sample in such a way that its amplitude stays unchanged, but the phase is changed, i.e. the wave vector k of the plane wave is changed. This can be understood because the electric potential of the atom columns $V(x,y)$ accelerates the electrons basically just as if the acceleration voltage of the microscope would have been changed. Due to the high acceleration voltages used in the TEM it is safe to assume that $V \ll V_0$,

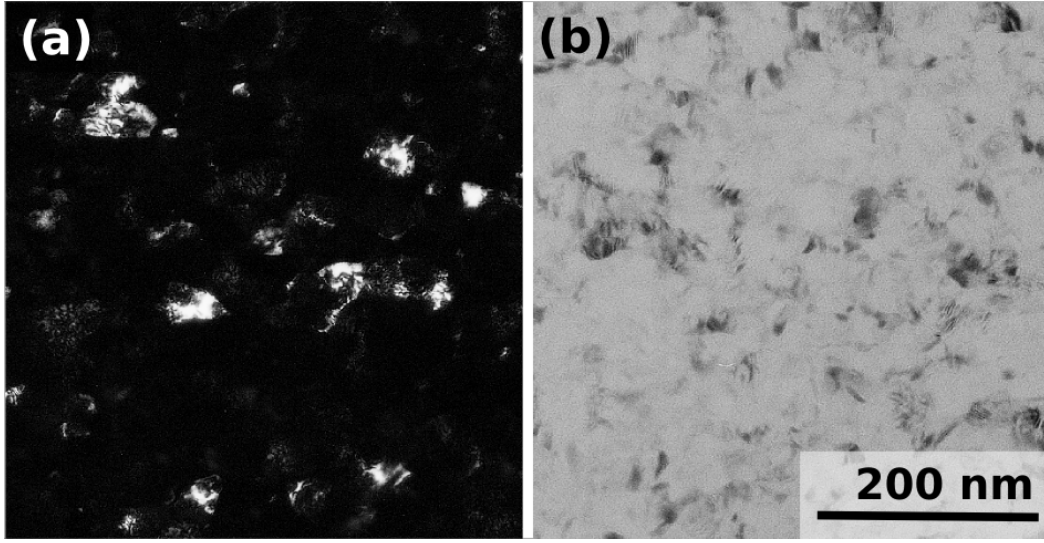


Figure 2.12: Typical dark-field (a) and bright-field (b) image of the same area of nanocrystalline FeAl deformed by HPT.

where V_0 represents the acceleration voltage leading to

$$\tilde{k} \approx k \left(1 + \frac{V(x,y)}{V_0} \right). \quad (2.22)$$

This is called phase object approximation (POA) and means that the exit wave is determined by multiplying the incident wave with

$$\exp(i\sigma V(x,y)), \quad (2.23)$$

where $\sigma = \frac{\pi}{\lambda V_0}$ denotes the interaction constant (without relativistic corrections) and $V(x,y)$ is called projected potential [DeGraef03]. For a higher precision it is possible to divide the sample into multiple slices and calculate and propagate the exit wave from slice to slice. This method commonly used in computer algorithms is called multislice algorithm. If the sample is sufficiently thin (i.e. $\sigma V \ll 1$), it is possible to expand the exponential function to

$$1 - i\sigma V(x,y), \quad (2.24)$$

which is called the weak phase object approximation (WPOA).

Knowing the exit wave, it is possible to apply the Fourier optics developed in

chapter 2.4 to obtain the image. This is done by a convolution of the exit wave with the Fourier transform of the contrast transfer function $CTF(g)$. The contrast transfer function contains the aperture function $A(g)$, the envelope function $E(g)$ that represents damping of higher spatial frequencies and the aberrations of the microscope $\exp(i\chi(g))$. For the phase object we are only interested in the imaginary part and thus it simplifies to

$$CTF(g) = A(g)E(g)2\sin(\chi(g)) \quad (2.25)$$

and the resulting image wave is

$$\psi(x,y) = \exp(ikx)(1 - i\sigma V(x,y)) \otimes \mathcal{F}[CTF(g)]. \quad (2.26)$$

The detected image represents the absolute square value of the wave [Williams96]

$$I \approx 1 + 2\sigma V(x,y) \otimes \mathcal{F}[CTF(g)]. \quad (2.27)$$

For perfect phase imaging we would need a transfer function that is 0 at $g=0$ and large and negative otherwise, then atoms would appear as black spots in the image (a positive value would lead to “bright” atoms). Unfortunately in the case of HRTEM the situation is not as easy as that. As shown in chapter 2.5.1 the most important aberrations are

$$\chi(g) = \frac{\pi}{2}C_s\lambda^3g^4 - \pi\Delta f\lambda g^2, \quad (2.28)$$

thus it is clear that the transfer function depends on the defocus and the spherical aberration coefficient. The defocus can be chosen freely and is usually set to the Scherzer defocus

$$\Delta f_{\text{Scherzer}} = -1.2\sqrt{C_s\lambda}. \quad (2.29)$$

Figure 2.13 shows the transfer function for the CM30 at Scherzer defocus. The CTF is 0, decreases and stays almost constant thus providing a broad band of good transmittance. The crossover of the CTF with the origin is called point resolution. At higher spatial frequencies the transfer function shows an oscillation behaviour and changes sign, leading to complicated contrast. The highest spatial frequency where the CTF is nonzero, is called information limit. By using focal

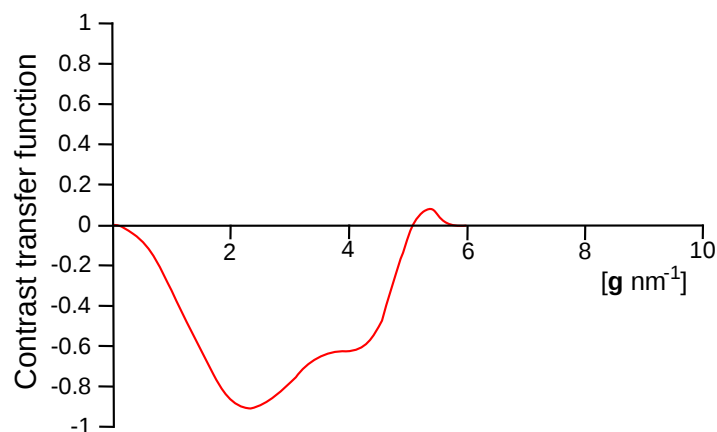


Figure 2.13: Contrast transfer function for the CM30 equipped with a LaB₆ cathode at Scherzer defocus. The CTF is 0 at 0 nm⁻¹ and provides a broad band of good transmittance up to spacial frequencies of about 5 nm⁻¹. The crossover of the CTF with the origin is called point resolution. The highest spatial frequency where the CTF is nonzero, is called information limit. The function was simulated using the JEMS software package [Stadelmann87].

series reconstruction, the information limit of the microscope can be reached. The microscope used was equipped with a LaB₆ electron source and therefore the information limit almost coincides with the point resolution. For microscopes equipped with a field emission gun the information limit goes well beyond point resolution limit (due to high spatial and temporal coherency). Special care has to be taken in these case when interpreting contrasts.

In any case, since the contrast depends on the sample thickness and the defocus, one has to be extremely careful with the interpretation of HRTEM images. For this reason usually a matrix of images for a given range of defocus and sample thickness values is simulated. Figure 2.14 shows such a map for FeAl.

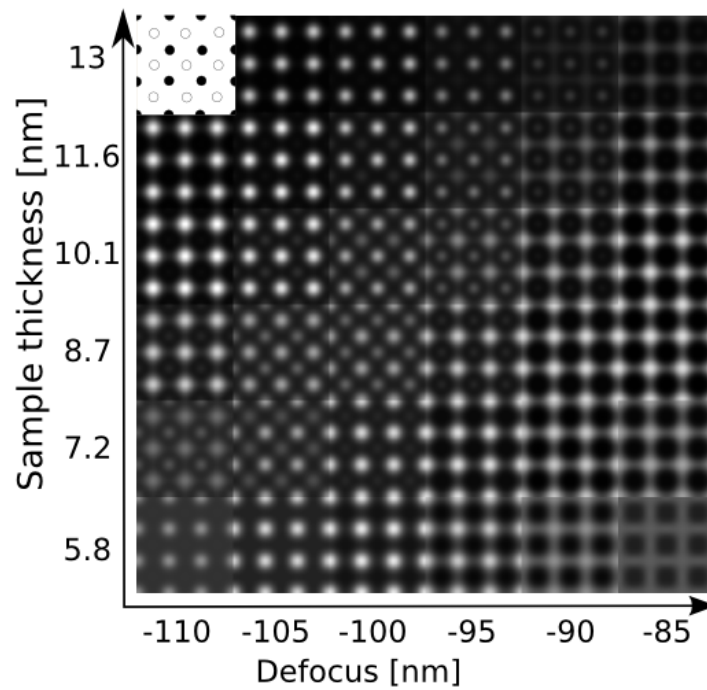


Figure 2.14: HRTEM map showing simulated images for different values of defocus and sample thickness. A FeAl crystal is simulated having a [100] orientation (cf. top left corner). It should be noted that the atom positions correspond either to bright or dark contrasts in the image. The map was simulated using the JEMS software package [Stadelmann87].

2.6 Diffraction

2.6.1 Diffraction and the Ewald Constuction

After a simple description of diffraction at lattice planes in chapter 2.5.3, a more elaborated description of diffraction using the Fourier transform will be developed. In chapter 2.4 it was shown that diffraction corresponds to the Fourier transform of the sample scattering power

$$\psi_{\text{dif}}(\vec{g}) \propto \mathcal{F}(f_{\text{sample}}(\vec{x})) = \int_{\mathbb{R}^3} f_{\text{sample}}(\vec{x}) \exp(-2\pi i \vec{g} \cdot \vec{x}) d\vec{x}, \quad (2.30)$$

whereas \vec{g} could not take any value in \mathbb{R}^3 but was restricted to $\vec{g} = k(\vec{n} - \vec{n}_0)$ (cf. Fig. 2.15a).

Let us now consider an infinite lattice with basic vectors \vec{a}_r . The reciprocal lattice \vec{a}_s^+ is defined by

$$\vec{a}_r \cdot \vec{a}_s^+ = \delta_{rs}. \quad (2.31)$$

It is the Fourier transform of the real lattice. Using this definition, the diffracted beams show only intensity if \vec{g} lies on the reciprocal lattice as then the expression $\vec{g} \cdot \vec{x}$ in the Fourier transform is not zero (cf. Fig. 2.15b). The next very helpful consequence of the reciprocal lattice is the possibility to use the Fourier convolution theorem. Consider for example a thin TEM specimen. The Fourier transform of a sample gives an elongated rod, thus using the Fourier convolution theorem, we just have to place the rod at every lattice point (cf. Fig. 2.15c). Similarly if we put atoms in the unit cell, we just have to superimpose the reciprocal lattice with the Fourier transform of the unit cell.

2.6.2 The Intensity of the Diffracted Beams

In detail this means that the lattice is given by

$$f(\vec{x}) = f_{\text{u}}(\vec{x}) \otimes \sum \delta(\vec{x} - \vec{x}_n), \quad (2.32)$$

where f_{u} represents the function of the unit cell which is repeated at every lattice point \vec{x}_n . The Fourier transform of the real lattice is the reciprocal lattice. Each position of the reciprocal lattice has to be superimposed with the Fourier transform of f_{u} , which is called structure factor. The structure factor can be represented as

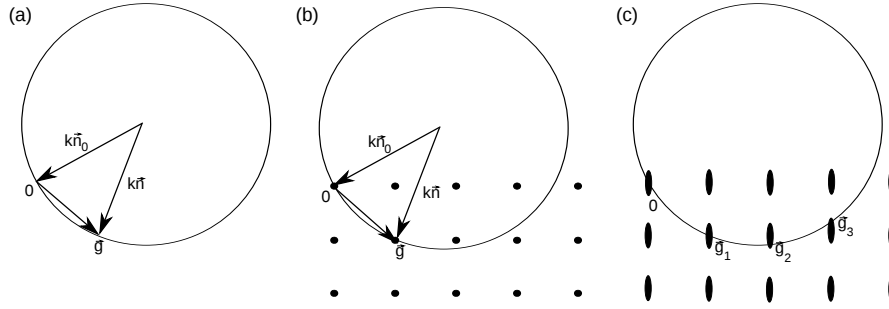


Figure 2.15: (a) The diffraction vector \vec{g} is limited to values $k(\vec{n} - \vec{n}_0)$. This leads to the Ewald construction, the vector $k\vec{n}_0$ is drawn in such a way that its ending point is the origin. Now a circle is constructed having this vector as radius. The diffraction vector \vec{g} has to end on the circle. (b) If the reciprocal lattice is drawn, the points touching the Ewald circle lead to constructive interference. (c) Thin films used in the TEM give rise to elongated lattice rods (thin objects have a broad Fourier transform) and thus more diffraction spots are visible in the TEM.

a sum of all the atoms in the unit cell

$$F(\vec{g}) = \sum_j f_i \exp(-2\pi i \vec{g} \vec{r}_j), \quad (2.33)$$

here f_i represents the atomic form factor of the atom sitting on this lattice place and \vec{r}_j its position in the unit cell. It should be noted that the atomic form factor is different for X-ray diffraction and electron diffraction [DeGraef03]. The main properties of the atomic form factor for electron diffraction are that it decreases with decreasing atomic number and increasing scattering angle.

The diffracted beam is therefore the Fourier transform of $f(\vec{x})$ which is simply the reciprocal lattice weighted with the structure factor. Using Miller indices (hkl) (meaning $\vec{g} = h\vec{a}_1^\dagger + k\vec{a}_2^\dagger + l\vec{a}_3^\dagger$) we reach for the intensity of the diffracted beam

$$I_{hkl} = KvV^{-2} |F(hkl)|^2, \quad (2.34)$$

where V denotes the volume of the unit cell, v is the effective diffracting volume and K a scaling factor containing only factors that do not depend on the sample or reflection used. In addition also the Debye-Waller factor that describes the influence of the temperature can be included. For the intensity of a diffraction ring resulting from a polycrystalline sample, the number of symmetry-equivalent

reflections $H_{\{hkl\}}$ and a Lorentz factor has to be added that takes into account geometric effects (in this simple case d_{hkl}) [Reimer08]

$$I_{\{hkl\}} = K v H_{\{hkl\}} V^{-2} |F(hkl)|^2 d_{hkl}. \quad (2.35)$$

It should be noted that this relation is only valid for untextured samples, and strong deviations from the expected intensity can occur in textured materials.

For this work the structure factor of A2 and B2 structured FeAl are of importance. B2 structured FeAl has an Fe-atom at the origin [000] and an Al-atom at the position $\frac{1}{2}[111]$ thus leading to

$$\begin{aligned} F^{B2}(hkl) &= f_{Fe} \exp(0) + f_{Al} \exp(-i\pi(h+k+l)) \\ &= \begin{cases} f_{Fe} + f_{Al} & h+k+l \text{ even} \\ f_{Fe} - f_{Al} & h+k+l \text{ odd} \end{cases} \end{aligned} \quad (2.36)$$

In the A2 structure at both positions a Fe- and an Al-atom can be found with equal probability

$$\begin{aligned} F^{A2}(hkl) &= (0.5f_{Fe} + 0.5f_{Al}) \exp(0) + \\ &\quad (0.5f_{Fe} + 0.5f_{Al}) \exp(-i\pi(h+k+l)) \\ &= \begin{cases} f_{Fe} + f_{Al} & h+k+l \text{ even} \\ 0 & h+k+l \text{ odd} \end{cases} \end{aligned} \quad (2.37)$$

The reflections with $h+k+l = \text{odd}$ are thus called superlattice reflections, and the other reflections matrix reflections. For a partly ordered material with a long-range order parameter S

$$\begin{aligned} F(hkl) &= (p_{\alpha,\alpha}f_{Fe} + p_{\beta,\alpha}f_{Al}) \exp(0) + \\ &\quad (p_{\alpha,\beta}f_{Fe} + p_{\beta,\beta}f_{Al}) \exp(-i\pi(h+k+l)) \\ &= \begin{cases} f_{Fe} + f_{Al} & h+k+l \text{ even} \\ S(f_{Fe} - f_{Al}) & h+k+l \text{ odd} \end{cases} \end{aligned} \quad (2.38)$$

(using $p_{\beta,\alpha} = 1 - p_{\beta,\beta}$, $p_{\alpha,\beta} = 1 - p_{\alpha,\alpha}$ and $S = 2p_{\alpha,\alpha} - 1 = 2p_{\beta,\beta} - 1$).

This means that the long-range order parameter can be determined from the intensity of a superlattice reflection. To exclude other effects on the intensity

(such as texture), the quotient of the intensity of a superlattice reflection and the corresponding matrix reflection is used [Warren90]

$$S^2 = \frac{I(100)}{I(200)} \frac{I_{\text{ordered}}(200)}{I_{\text{ordered}}(100)} \propto \frac{I(100)}{I(200)}. \quad (2.39)$$

2.6.3 Dynamic Effects in Electron Diffraction

As in electron diffraction the interaction with matter is very high (the intensity of the diffracted beam is about a factor of 10^4 larger as compared to X-ray diffraction) the assumption that the diffracted beams will not be diffracted again is not valid. Therefore we need to apply the dynamic theory of diffraction to calculate the intensities of the diffracted beams correctly. The following table gives a short overview of the most prominent diffraction techniques:

type of diffraction	typical wavelength	typical scattering cross section	dynamic/kinematic
electron	2.5 pm (200 kV)	10^6 barn	dynamic
X-ray	154 pm ($\text{CuK}\alpha$)	400 barn	kinematic
neutron	100 pm	10 barn	kinematic

In the theory of dynamic diffraction, scattering of diffracted beams has to be accounted for. Therefore the intensities of different reflections are not independent of each other and are dependent strongly on the thickness of the crystal. The intensities can be determined by solving a set of coupled differential equations (for each diffracted beam one equation) called Howie-Whelan equations [Howie62]. For the simple two-beam case (i.e. the crystallite is oriented in such a way that only the transmitted beam and one diffracted beam are excited) these equations can be solved [Fultz05] leading to the following intensity for the diffracted beam (I_g). The intensity of the transmitted beam is $I_0 - I_g$ in this case.

$$I_g = \frac{\sin^2(\pi t s_{eff})}{(\xi_g s_{eff})^2} \quad (2.40)$$

where

$$\xi_g = \frac{\pi V \cos \theta_B}{\lambda F_g} \quad (2.41)$$

denotes the extinction distance, t the thickness of the crystallite in direction of the transmission, s the excitation error and

$$s_{eff} = \sqrt{s^2 + \frac{1}{\xi_g^2}} \quad (2.42)$$

the effective excitation error.

2.6.4 The Width of the Diffracted Peaks

In addition to the intensity of the diffraction peaks, their shape is important because it gives information on the microstructure. The main effects that can be observed are shifting, broadening and asymmetric broadening of the peaks. Consider first peak broadening; many effects give rise to peak broadening:

- The instrumental broadening
- The limited size of the crystallites (coherently scattering domains)
- Non-uniform lattice distortions (strains)
- Planar faults
- More specialized effects such as solid solution inhomogeneities

The resulting signal is a convolution of all these effects plus the background

$$I(g) = I_{\text{instrumental}} \otimes I_{\text{size}} \otimes I_{\text{strain}} \otimes I_{\text{planar faults}} \otimes \dots + \text{Background}. \quad (2.43)$$

The background is very difficult to simulate using a physical function and is thus generally fitted empirically. The instrumental broadening can be determined by measuring a coarse crystalline sample, where size and strain broadening is negligible. A detailed description of size and strain broadening will be given in the following chapters.

2.6.5 Size Broadening

Consider a finite crystallite. The sample function changes from equation 2.32 to

$$f(\vec{x}) = f_u(\vec{x}) \otimes \sum \delta(\vec{x} - \vec{x}_n) s(\vec{x}) \quad (2.44)$$

whereby s , the shape function, takes a value of 1 inside of the crystallite and 0 else.

Taking the squared Fourier transform (neglecting cross terms) leads to

$$I(\vec{g}) \propto F^2 \mathcal{F}[s]^2 \quad (2.45)$$

Using $\mathcal{F}[s]^2 = \mathcal{F}[s \otimes s]$ leads to the new expression

$$V \cdot V(t) = s \otimes s, \quad (2.46)$$

where V is the volume of the crystallite and $V(t)$ has an interpretation as the volume common to a crystallite with itself shifted a distance t (for a specific peak the shift has to be normal to the diffracting planes). Thus the relevant additional factor in the intensity of the diffracted beam due to the finite size is [Beyerlein11]

$$V \mathcal{F}[V(t)]. \quad (2.47)$$

Diffraction from a perfect crystal gives rise to sharp diffraction spots. Consider a crystallite with a limited number of scattering planes, thickness= D (cf. Fig. 2.16). For this case $V(t)$ is simply a triangle function (\wedge) and the corresponding intensity is proportional to

$$I(g) \propto \mathcal{F}[\wedge] = \frac{\sin^2(\pi Dg)}{(\pi g)^2}, \quad (2.48)$$

showing that a limited crystal size gives rise to a broadened peak. The width of the peak depends inversely on the size of the crystallite. The intensity of a 3D crystallite can be calculated in an analogous way.

It is important to point out that the crystallite size is a measure of the coherently diffracting domain. It is not the same thing as the grain size or particle size ($D_{\text{crystallite}} < D_{\text{grain}} < D_{\text{particle}}$). Coherence is broken down by orientation variations as small as 1° [Ungar05]. In severely deformed materials the crystallite size would correspond to the size of the dislocation cells [Ungar05].

Consider now an ensemble of crystallites (cf. Fig. 2.17a). Only crystallites in Bragg-position give rise to scattering into the (hkl) reflection. For the sake of simplicity the coordinate system is chosen such that the z -axis points in the direction of the diffraction vector (i.e. perpendicular to the scattering planes).

The integral width β is defined as the area of the peak divided by its maximum

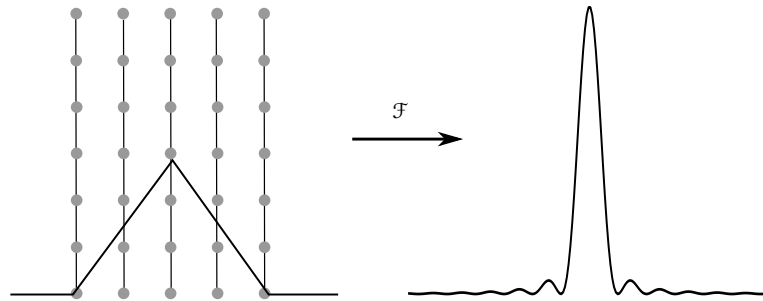


Figure 2.16: Diffraction on a small crystallite consisting of only few lattice planes. $V(t)$ of the crystallite is a triangle function (\wedge) and the diffracted intensity, which is given by the Fourier transform is a squared sinc-function. The width of the sinc-function is inversely proportional to the size of the crystallite.

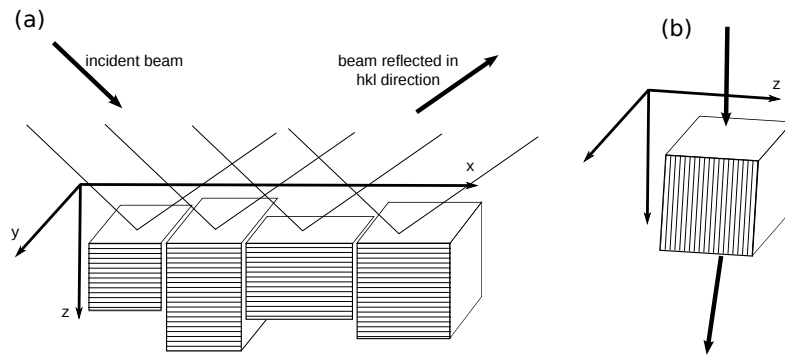


Figure 2.17: (a) Derivation of the Scherrer equation. An incident beam is scattered on crystallites that have a limited size. The crystallites are drawn such that the reflecting planes are normal to the z-axis. (b) If the diffraction is not done in reflection but in transmission not the height but the width of the crystallites is measured).

(the width of a rectangle with the same area as the peak). As the area of the peak ($\frac{\sin^2(\pi Dg)}{(\pi g)^2}$) is proportional to D and the maximum to D^2 , we get if we integrate over the ensemble of crystallites

$$\beta = \frac{\text{Area}}{\text{Maximum}} = \frac{\int D(x,y)dxdy}{\int D(x,y)^2dxdy}, \quad (2.49)$$

and using $D = \int dz$ and $\int D(x,y)dxdy = V$

$$\beta^{-1} = \frac{1}{V} \int DdV. \quad (2.50)$$

Thus the integral width is inversely proportional to the volume weighted mean height of the crystallites in Bragg positions measured in direction of the diffraction vector (usually called volume-weighted column-length) [Langford78]

$$\langle D \rangle_V = \beta^{-1}. \quad (2.51)$$

An other way to express the integral width is by using $V(t)$ leading to

$$\langle D \rangle_V = \frac{1}{V} \int V(t)dt. \quad (2.52)$$

It should be pointed out that when the diffraction is not done in reflection (as shown in Fig. 2.17a) but in transmission as it is the case in a TEM, not the height but the width of the crystallites is measured (cf. Fig. 2.17b).

An other measure of the peak width that is often used is the full width at half maximum (FWHM). The FWHM (Δg) is slightly larger than the integral width leading to the following relation, which is usually called Scherrer equation

$$\langle D \rangle_V = \frac{0.85}{\Delta g}. \quad (2.53)$$

Different values can be found for this constant in literature and it can change slightly depending on the crystallite form and distribution. Still it is important to note that the inverse relation to the integral width is exact.

The true volume weighted size

$$\langle D \rangle_{V,\text{true}} = \frac{\sum_i D_i \cdot D_i^3}{\sum_i D_i^3} \quad (2.54)$$

(whereas D_i represents the diameter of an equivalent sphere with the same volume as particle i) however depends on the crystallite form and distribution. This is often expressed by

$$\langle D \rangle_{V,\text{true}} = K \langle D \rangle_V, \quad (2.55)$$

where K is called Scherrer constant [Langford78]. Assuming spherical crystallites $K = \frac{4}{3}$. It should be noted that if the crystallites are elongated and the elongation has a specific relation to the crystal orientation, the peak width will be different for different peaks. This is called anisotropic size broadening [Langford78].

A completely different approach to measure the crystallite size is the Warren-Averbach method [Warren50]. It can be used to determine the area weighted mean height of the crystallites in Bragg positions measured in direction of the scattering vector (usually called area-weighted column-length), which is given by (applying the Leibnitz integral rule)

$$\langle D \rangle_A = -\frac{V(0)}{V'(0)}. \quad (2.56)$$

From this equation it follows that by plotting the Fourier transform of the peak (which is $V(t)$), the intercept of the tangent at $t = 0$ with the t -axis is the area weighted mean (cf. Fig. 2.18). Usually instead of t the column length L is used that is measured in units of the lattice spacing. In practice a Fourier series is computed and the Fourier coefficients $A(L)$ are used for the analysis. This method is described in [Warren90].

By this method it is also possible to determine the crystallite size distribution [Kril98]. Still in general a complementary method (such as TEM) is necessary for an unequivocal determination of the crystallite size distribution. Furthermore very broad or multimodal size distributions make a profile analysis very difficult.

Special care has to be taken when comparing different statistical parameters that can be used to describe the crystallite size distribution. An overview of different “sizes” is given in Figure 2.19. Most frequently mean diameters are used that are computed by assuming that all crystallites have a circular shape. Large discrepancies exist however in the weighting.

Usually the situation is quite complicated and the diffracted beam depends on the shape and the distribution of the crystallites. It has been shown that the Voigt [Balzar99] function can be used to fit peaks. The Voigt function is a convo-

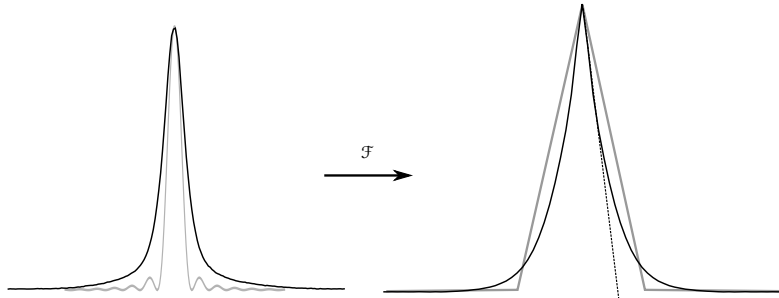


Figure 2.18: Light grey curves: The diffracted peak of an idealised crystallite is a sinc-function. Taking the Fourier transform of the diffracted peak gives $V(t)$, which is in this case a triangle function where the width of the triangle function represents the size of the crystallite. Black curves: A more realistic diffracted peak is shown. Taking the Fourier transform gives a function that deviates from the ideal triangle function. The size is determined in this case by putting a tangent to the function and taking its intersect with the t-axis.

lution of a Gauss

$$I \propto \exp\left(-\pi \frac{x^2}{\beta_G^2}\right) \quad (2.57)$$

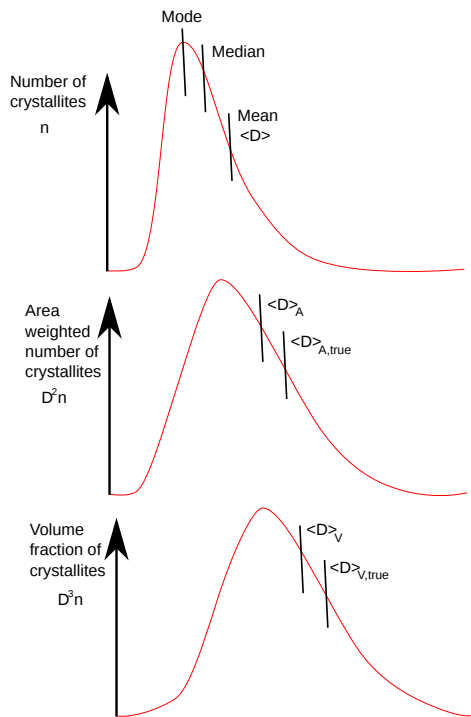
and a Lorentz function

$$I \propto \left(\frac{\beta_L^2}{\pi^2} + x^2\right)^{-1}. \quad (2.58)$$

As the Voigt function is rather difficult to compute often the pseudo-Voigt function (which is the sum of a Gaussian and a Lorentz curve) is used to fit peaks [Thompson87, Lin97]

$$pV = I_0 \left(\nu \frac{1}{\pi w} \left(1 + \left(\frac{x - x_0}{w} \right)^2 \right)^{-1} + (1 - \nu) \sqrt{\frac{\ln(2)}{\pi w^2}} \exp\left(-\ln(2) \left(\frac{x - x_0}{w} \right)^2\right) \right), \quad (2.59)$$

where I_0 denotes the area under the peak, ν the mixing parameter, x_0 the position



mode of the crystallite diameters

The most frequently occurring crystallite diameter.

median crystallite diameter

50% of the crystallites are larger/smaller than this size.

mean crystallite diameter

$\langle D \rangle$ The average of all the crystallite diameters.

area-weighted column-length

$\langle D \rangle_A$ The area weighted mean size measured in direction of the diffraction vector.

area-weighted mean diameter $\langle D \rangle_{A,true}$ The mean crystallite diameter, whereas each crystallite is weighted with D^2 . ($\langle D \rangle_{A,true} = \frac{3}{2} \langle D \rangle_A$ for spherical crystallites)

volume-weighted column-length $\langle D \rangle_V$ The volume weighted mean size measured in direction of the diffraction vector.

volume-weighted mean diameter $\langle D \rangle_{V,true}$ The mean crystallite diameter, whereas each crystallite is weighted with D^3 , i.e. the volume fraction. ($\langle D \rangle_{V,true} = \frac{4}{3} \langle D \rangle_V$ for spherical crystallites)

Figure 2.19: If there is not one sharp crystallite size but a distribution of sizes different statistical measures can be used to define the size. The mean value is most often used. The mean crystallite diameter is determined when counting crystallites (as is done when using TEM dark-field images, but in this case the grain size is measured). In diffraction not the number of crystallites is relevant but the area weighted or volume weighted crystallite diameter (depending on which method is used). In addition to that it should be noted that the size extracted from profile analysis is not the mean diameter but a mean column-length and thus a correction factor has to be used.

and $2w$ the FWHM. The integral width can be calculated using

$$\beta = \frac{w}{(1 - \nu)\sqrt{\frac{\ln(2)}{\pi}} + \nu\frac{1}{\pi}}. \quad (2.60)$$

The use of the pseudo-Voigt function is justified as for a wide range of shapes and distributions. Simulations of the size-broadening for spherical crystallites and typical (i.e. not too broad) lognormal or gamma distributions show that the line profiles can be satisfactorily modelled using pseudo-Voigt functions [Popa02, Reimann02]. Broader crystallite size distributions yield a higher contribution of the Lorentzian part in the Voigt function, which is obvious as a Lorentz function has a more pronounced tail in comparison to the Gaussian. The Gaussian contribution to the Voigt function is therefore often used to describe the width of the crystallite size distribution. The exact expression for the peak profile of spherical crystallites with a log-normal distribution can be found for example in [Ribarik01].

2.6.6 Strain Broadening

If a grain contains a uniform strain, this leads to a change in lattice spacing and thus to a simple shift of the diffracted peak, but not to a broadening of the peak. If g_0 denotes the equilibrium diffraction vector, a compressive stress leads to $g > g_0$ and a tensile stress to a $g < g_0$.

If the strain is not uniform, there is a combination between compressive and tensile stresses. The resulting diffracted peak will consist of many peaks with a slightly different position and therefore appear as an additionally broadened peak. To analyse the strain broadening consider the Bragg equation

$$g = \frac{1}{d} \quad (2.61)$$

by differentiation follows

$$\frac{dg}{dd} = -\frac{1}{d^2} \quad (2.62)$$

or

$$\Delta g = -\Delta d \frac{1}{d^2} = -g \frac{\Delta d}{d} \quad (2.63)$$

which leads to the conclusion that the peak width is proportional to g times the lattice strain. The strain broadening is thus dependent on g , which can be used to separate the size broadening from the strain broadening. For this purpose the apparent strain e was introduced [Stokes44]

$$e = \frac{\beta_{strain}}{2g} \quad (2.64)$$

which has an interpretation as maximum strain.

How the strain and size broadening are convoluted depends on the assumption of the peak broadening [Balzar96]. The Williamson-Hall plot [Williamson53] follows directly by assuming a Cauchy peak shape for both the size and strain broadening

$$\beta = \beta_{size} + \beta_{strain} = \frac{1}{\langle D \rangle_V} + 2eg. \quad (2.65)$$

Assuming a Gaussian broadening leads to

$$\beta^2 = \beta_{size}^2 + \beta_{strain}^2 = \frac{1}{\langle D \rangle_V^2} + 4e^2 g^2. \quad (2.66)$$

For a more detailed analysis it is best to start with the Warren-Averbach method [Warren50, Warren90]. If for two lattice planes the distance is slightly different from the ideal distance, the strain can be defined as

$$\epsilon(L) = \frac{\Delta L(L)}{L}, \quad (2.67)$$

where L denotes the lattice separation distance. The effect of the strain on the Fourier coefficient thus follows by averaging over all cells with a distance L

$$A_{distortion}(L,g) = \langle \exp(-2\pi i g L \epsilon(L)) \rangle. \quad (2.68)$$

For not too large L

$$A_{distortion}(L,g) \approx \exp(-2\pi^2 g^2 L^2 \langle \epsilon^2(L) \rangle). \quad (2.69)$$

Assuming the broadening results from a size and a strain broadening, the Fourier coefficient can be written as $A(L) = A_{size}(L)A_{distortion}(L)$ or taking the logarithm

$$\ln A(L) = \ln A_{size}(L) - 2\pi^2 g^2 L^2 \langle \epsilon^2(L) \rangle. \quad (2.70)$$

Thus using the Warren-Averbach method, size and strain broadening can be separated. To calculate the intensity profile, the inverse Fourier transform of $A(L)$ has to be taken

$$I(g) = 2 \int_0^\infty A(L) \cos(2\pi Lg) dL. \quad (2.71)$$

A second very popular method to separate size and strain is the double-Voigt method [Balzar93, Balzar99]. Assuming that both the size and the strain have a Gauss and a Lorentz part leads to the following expressions

$$\beta^C = \beta_{size}^C + \underbrace{a^C g^2}_{\beta_{strain}^C} \quad (2.72)$$

$$\beta^G = \beta_{size}^G + \underbrace{a^G g^2}_{\beta_{strain}^G} \quad (2.73)$$

where the superscripts C and G denote the Cauchy and the Gauss parts. The fact that in contrary to the Williamson-Hall plot, the mean-square strain depends quadratically also on both, the Lorentz and the Gaussian part, results from the different definition of strain.

By taking the Fourier transform of a Voigt-profile and comparing to the definitions of size and strain the following expressions can be deduced [Balzar93]

$$\langle D \rangle_V = \frac{1}{\beta_{size}} \quad (2.74)$$

$$\langle D \rangle_A = \frac{1}{2\beta_{size}^C} \quad (2.75)$$

$$\langle \epsilon^2(L) \rangle = \frac{1}{g^2} \left(\frac{\beta_{strain}^G}{2\pi} + \frac{\beta_{strain}^C}{L\pi^2} \right) \quad (2.76)$$

Thus the double Voigt approach is equivalent to the Warren-Averbach approximation and it is thus built into a many whole profile analysis computer programs based on Rietveld refinement such as the commercially available TOPAS [Topas] or the freeware BREADTH [Breadth]. From these equations it can be immediately seen that for a Gaussian strain distribution the strain is independent of L and it follows that

$$\sqrt{\langle \epsilon^2 \rangle} = \sqrt{\frac{2}{\pi}} e. \quad (2.77)$$

Further approaches are the momentum or variance method, where the asymptotic behaviour of a peak is used [Groma98, Borbely01] or the whole powder pattern modelling. Here in contrast to whole profile analysis no analytical functions are used to fit the peaks but ab-initio theoretical profile functions are constructed using a model based on microstructural parameters and fitted to the profile. Software packages based on this method are MWP-fit [Ribarik01] and PM2K [Leoni06].

2.6.7 Strain Field of Dislocations

To evaluate the strain field of an arrangement of dislocations is quite complex and depends not only on the density and type of defect but also on their correlation. Wilkens [Wilkens70] has introduced a very popular model to describe the mean square strain due to dislocations (here only the leading term is presented, the abbreviation $L^* = 0.5 \exp(-0.25) \cdot L$ is used)

$$\langle \epsilon^2(L) \rangle = \frac{\rho C b^2}{4\pi} \begin{cases} -\ln\left(\frac{L^*}{R_{eff}}\right) + \dots, & \text{if } \frac{R_{eff}}{L} > 1 \\ \frac{R_{eff}}{L} + \dots, & \text{if } 1.81 \frac{R_{eff}}{L^*} \leq 1 \end{cases} \quad (2.78)$$

In this formula ρ represents the dislocation density, b the Burgers vector, R_{eff} the cutoff radius of the dislocation strain field and C the contrast factor, which represents the visibility of dislocations in different reflections. This definition is introduced as dislocations lead to an anisotropic broadening, e.g. for $b \cdot g = 0$ no broadening is visible. The average dislocation contrast factor for untextured cubic crystals with equally populated slip systems is given by

$$C = C_{h00} \left(1 - q \frac{h^2 k^2 + h^2 l^2 + k^2 l^2}{(h^2 + k^2 + l^2)^2} \right) \quad (2.79)$$

where C_{h00} and g depend on the elastic constants and the type of dislocations and lead to 0.35 and 2.77 for screw dislocations and 0.39 and 2.77 for edge dislocations in FeAl. Thus to get rid of the anisotropic broadening $C \cdot g$ is used instead of g in the modified Williamson-Hall plot or the modified Warren-Averbach plot [Ungar96, Ungar99]. It should be noted that the contrast factors of dislocations for most crystal systems can be calculated on the AnizC website [AnizC].

2.6.8 The Modified Williamson-Hall Plot

Now it is possible to formulate the modified Williamson-Hall plot

$$\beta = \frac{1}{\langle D \rangle_V} + 2e \cdot (\sqrt{C}g) \quad (2.80)$$

or when expressed as a function of the dislocation density

$$\beta = \frac{1}{\langle D \rangle_V} + \sqrt{0.5 \ln(P) A} \rho b (\sqrt{C}g). \quad (2.81)$$

It should be noted that if the FWHM is used rather than the integral width $\frac{0.85}{\langle D \rangle_V}$ has to be used. The modified Williamson-Hall plot proposed by Ungar [Ungar96] takes not only the dislocation density into account but also the dislocation correlations ($Q = \langle \rho^2 \rangle - \langle \rho \rangle^2$) but for the present work it was decided to limit the number of fitting parameters to a minimum in order to increase the reliability. Still it should be noted that the Williamson-Hall plot can also contain higher orders of g , therefore it is often observed that the points lie on a curve that is in between a linear and a quadratic one.

2.6.9 Other Effects Leading to Peak Broadening

Extended defects such as stacking faults or twins can lead to the termination of the coherency and thus to an additional broadening [Balogh06, Ungar98]. The broadening is very different for different reflections as only certain lattice planes are affected by planar faults. Furthermore stacking faults introduce an asymmetric broadening and can also lead to peak shifts.

Stacking faults and twins are not of importance for nanocrystalline FeAl. But in FeAl the order is destroyed by APB. APB also lead to an additional peak broadening that affects only superlattice reflections. Thus superlattice reflections have to be

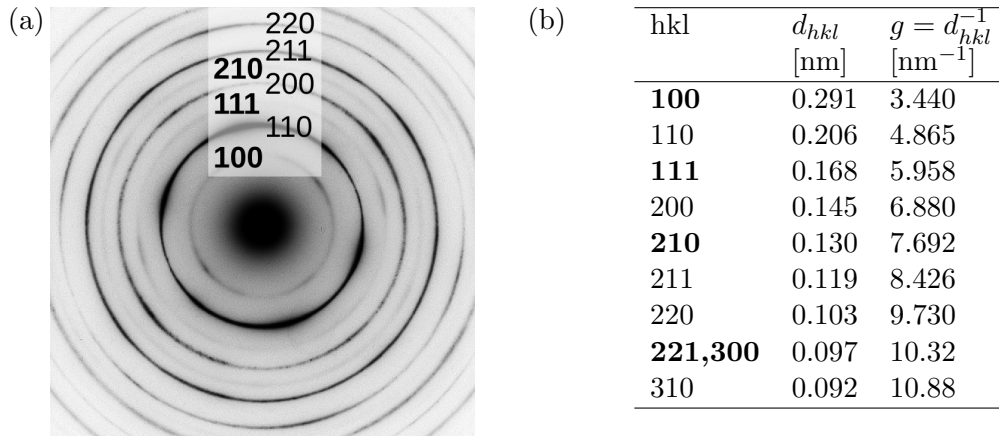


Figure 2.20: (a) Indexed diffraction pattern of FeAl annealed to 220°C. Superlattice reflections are indicated in bold. (b) Table showing the lattice distances d_{hkl} and diffraction vectors g_{hkl} of the reflections appearing in FeAl.

treated separately and the size determined from the superlattice reflections is not the crystallite size but the size of the ordered domains.

2.6.10 Peak Positions

Not only the intensity or the width of the peaks can be evaluated but also their positions. As discussed already in chapter 2.6.6 a homogeneous lattice strain leads to a change in lattice constant and thus to a shift of the peak. Thus a lattice expansion or a lattice compression can be detected by a precise measurement of the peak positions.

Furthermore there can also exist lattice strains that are orientation dependent resulting from residual stresses. In a material that contains many grains, an individual grain is not free to deform in the same way as an isolated grain as it is restrained by its neighbours. This can lead to residual stress after deformation or production of thin films. Especially in thin films there can be also residual stresses arising from lattice misfits or impurities. These stresses lead to a direction-dependent lattice strain that can be measured by diffraction stress analysis, which is done by tilting and rotating the specimen and measuring the change in lattice constant [Welzel05].

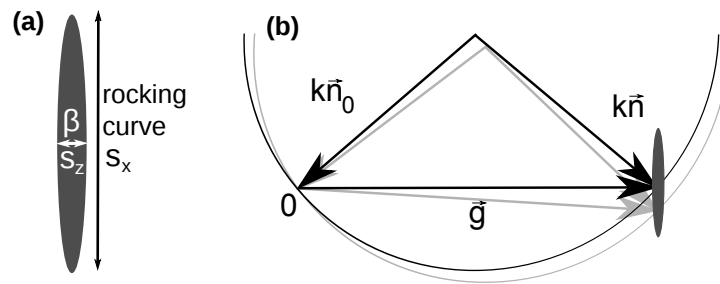


Figure 2.21: (a) Schematic drawing of a reciprocal lattice spot. The lattice spot is extended in all directions (s_x, s_y, s_z). s_z is measured in direction of \vec{g} and s_x, s_y normal to that. It should be noted that the broadening in direction of s_z is usually much smaller than in the other two directions. (b) Schematic drawing showing that the rocking curve s_x can be measured by tilting the sample and thus the Laue circle.

2.6.11 Diffraction in FeAl

Figure 2.20a shows a typical electron diffraction pattern of nanocrystalline FeAl. The diffraction pattern shows a ring pattern as the grains are randomly distributed. The diffraction rings are indexed. Bold reflections are superlattice reflections, they appear only in the B2, but not in the A2 structure (cf. chapter 2.6.2). Furthermore Figure 2.20b shows a table of diffraction rings appearing in FeAl including the lattice distance d and diffraction vector $g = d^{-1}$, which can be used for indexing diffraction patterns. .

2.7 Peak Broadening in 3D

The diffraction spots of a material extend in the reciprocal space in all directions (s_x, s_y, s_z) (cf. Fig.2.21a). In the previous chapter only the profile in the direction of \vec{g} was considered. In this case the relevant dimension is s_z and the broadening, called line broadening, provides information on the crystallite size and strain in the material. In addition there is also a broadening normal to that (s_x , often called simply s). By tilting the sample and thus the Ewald sphere it is possible to record a curve in the direction s_x , called rocking curve (cf. Fig.2.21b). The rocking curve can be important for materials deformed to a low degree. These materials contain deformation cells that are slightly tilted against each other and thus give rise to a broadening in the rocking curve [Jakobsen06].

2.8 Texture

In general in a polycrystalline material all grains are oriented in a random way. If this is not the case and the grains have some preferred directions this is called texture [Kocks98, Engler09]. There are two ways of recording texture: by using diffraction it is possible to detect the intensity changes of a certain reflection with orientation and on the other hand by methods like electron backscatter diffraction (EBSD) the orientation of each individual grain can be mapped [Suwas08].

Also selected area diffraction provides information about the texture of a sample. If a material is nano- or polycrystalline, rings can be seen in the diffraction pattern. If the intensity of some of these rings is very weak or if the rings are not uniform, this is an indication of texture [Schwarzer93]. For a detailed analysis the sample has to be tilted to several orientations. In general texture is very important in deformation as usually some orientations are unstable (thus their volume fraction decreases) and some are stable (thus their volume fraction increases) with respect to the deformation imposed and hence texture develops. Thus also in materials processed by severe plastic deformation, usually pronounced textures can be observed [Kilmametov04].

There exist two very prominent types of texture. If the crystals are oriented in such a way that the same crystallographic direction $[uvw]$ in most of the grains is nearly parallel to an axis, this is called a $[uvw]$ fibre texture and the axis is called fibre axis. A fibre texture usually is present in extruded materials. If the crystals are oriented in such a way that the same crystallographic plane (hkl) in most of the grains is nearly parallel to the sheet surface and a certain direction in that plane is roughly parallel to a direction $[uvw]$ called rolling direction, this is called a $(hkl)[uvw]$ sheet texture. Such textures can be found in materials after torsion. In cold-rolled materials, the texture can occur as combinations of many different sheet textures and is thus in the most general way described by fibre textures. In the following all texture components relevant for bcc are summarized [Kocks98]:

Deformation mode	texture components
extrusion	$\langle 110 \rangle$
compression	$\langle 111 \rangle, \langle 100 \rangle$
shear	$\{112\} \langle 110 \rangle$ (D component) $\{110\} \langle 001 \rangle$ (E component)
rolling	$\{001\} \langle 110 \rangle, \{111\} \langle 110 \rangle$ (i.e. $\langle 110 \rangle \parallel$ RD, α -fibre) $\{111\} \langle 110 \rangle, \{111\} \langle 112 \rangle$ (i.e. $\langle 111 \rangle \parallel$ ND, γ -fibre) $\{001\} \langle 110 \rangle, \{111\} \langle 112 \rangle$ (i.e. $\langle 110 \rangle \parallel$ TD, ϵ -fibre)

2.9 Microhardness Measurements

The hardness of a solid is a measure for its resistance to plastic deformation. Hardness is not an intrinsic material property and does not have a precise definition. It is a property value of the material that is determined using a defined measurement procedure. The most common way to measure hardness is by indentation [Tabor96]. A tip is pressed into the material using a defined force. From the size of the formed impression the hardness can be determined. It has been shown that there is a linear correlation between indentation hardness H_V and tensile strength σ for metals ($H_V \approx 3\sigma$) [Pavlina08]. Thus in industry indentation hardness measurements are often used for a nondestructive testing of bulk metals.

In the present case the Vickers microhardness [Smith22] method was used, where the indenter is a diamond tip with the shape of a squared pyramid with a top angle of 136° (cf. Fig. 2.22a). The tip was pressed into the material. The applied force was increased with a rate of 0.1 N/s. The maximum force of 2 N was held for 10 seconds before the tip was retracted. The maximum force was chosen so that the size of the imprint is between 20 and 30 μm as in this range the maximum precision is reached. Indentation was performed in our faculty using a Paar MHT-4 indenter. The imprints were recorded using a Zeiss Axioplan optical microscope equipped with a CCD-camera. Figure 2.22b shows an image of a typical imprint in FeAl. From the size of the diagonal of the imprint (d) and the maximum force (F) the Vickers hardness can be calculated using the following relation

$$H_V = 1.8544 \frac{F}{d^2} \text{ [Pa]}. \quad (2.82)$$

For a good statistics for every microhardness measurement at least 10 imprints

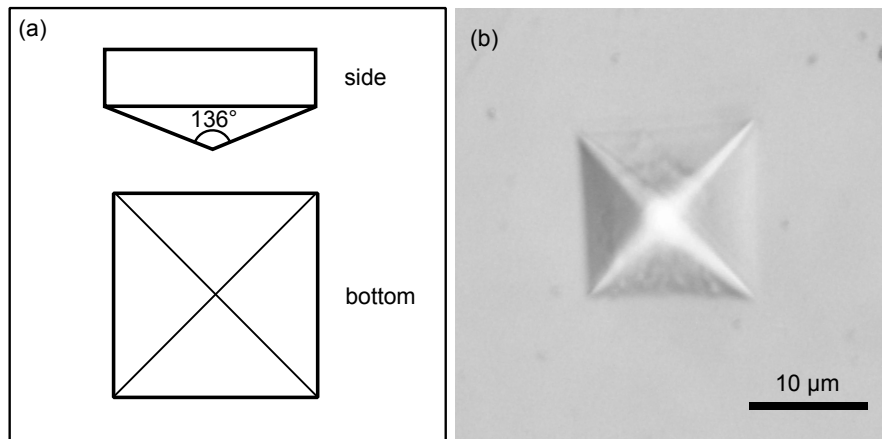


Figure 2.22: Figure showing the Vickers microhardness measurement. (a) The indenter has a diamond tip with the shape of a squared pyramid and a top angle of 136° . From the size of the imprint of the tip (b), the hardness can be determined.

were recorded and the mean and standard deviation was determined.

2.10 Differential Scanning Calorimetry

2.10.1 Schematic Representation of a DSC

Differential scanning calorimetry (DSC) is a procedure for the determination of the heat flow to a sample (endothermic) or from a sample (exothermic) at a given temperature $T(t)$. One can differentiate between isothermal measurements (measurements at a constant temperature) and isochronal measurements (measurements with a constant heating rate and cooling rate). Figure 2.23 shows a schematic representation of a heat flow DSC, which measures the heat flow between a sample and a reference. A furnace is heated using a defined temperature program. Two crucibles are placed on the sensor, an empty crucible as reference (R) and a second crucible filled with the sample (S). The sensor is a heat conducting disc with a well defined heat conductivity. In the sensor thermocouples are integrated that measure the temperature difference ΔT between the reference and the sample. As the sensor has a well defined heat conductivity, the temperature difference is proportional to the heat flow $\Delta W = k\Delta T$. The device-specific proportionality constant k can be calibrated using a set of standard samples [Hoehne96].

Beside the heat flow DSC there is also the power-compensated DSC. In this de-

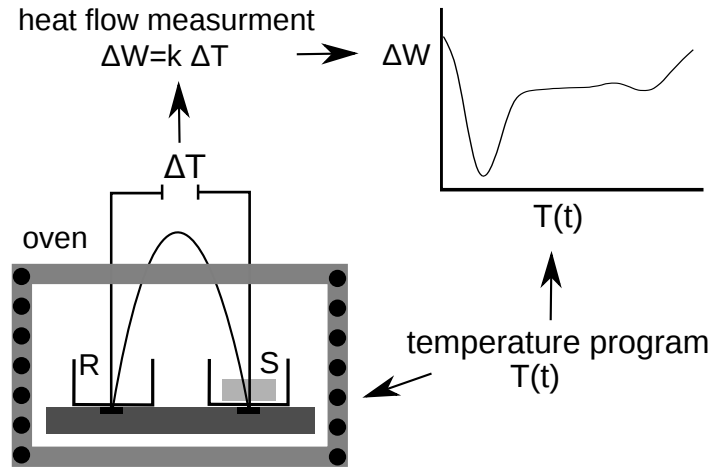


Figure 2.23: Schematic representation of a heat flow DSC. A furnace is subjected to a given temperature program $T(t)$. The temperature difference ΔT between the reference and the sample is measured. Since there is a well defined thermal resistance between sample and reference, the temperature difference is proportional to the heat flow ΔW .

sign both the reference and the sample are heated separately and kept at the same temperature. Therefore the heat flow needed to heat the samples can be measured directly. The power compensated DSC is usually used for isothermal measurements. A rather new technique is the modulated DSC where a sinusoidal signal is superimposed with a linear heating/cooling to distinguish between reversible and non-reversible heat flow [Reading94]. Differential Thermal Analysis (DTA) is similar to the heat-flow DSC with the difference that the sample and reference are not connected. Still there is a temperature difference between sample and reference as for example the sample absorbs energy in the case of an endothermic process and the sample temperature starts to lag behind. DTA is used particularly at higher temperatures or in aggressive environments, where a heat-flux DSC would not be able to operate. Devices that can measure heat flows smaller than $1 \mu\text{W}$ are called microcalorimeters. Furthermore there exist also combined devices such as the thermalgravimeter, which contains a microbalance and can be used for oxidizing measurements.

2.10.2 Evaluation of DSC Curves

DSC experiments can be used to determine a broad range of processes [Hoehne96]. Processes giving rise to a heat flow/absorption or a change in specific heat can be quantified. For this work we will be mainly interested in reordering, recovery (i.e. the annihilation of dislocations) and grain growth, all giving rise to an exothermic peak.

2.10.3 Determination of the Activation Energy from a DSC Curve

Thermally activated reactions can be very complex, but usually as a simplification it is assumed that the transformation rate $\frac{d\alpha}{dt}$ can be described as product of a function depending on the transformed fraction α and one depending on the temperature T

$$\frac{d\alpha}{dt} = f(\alpha)K(T). \quad (2.83)$$

Furthermore it is assumed that the temperature dependent function follows an Arrhenius type dependency

$$K = k_0 \exp\left(-\frac{E_a}{RT}\right), \quad (2.84)$$

where k_0 is a constant and E_a represents the activation energy of the process.

For a set of isothermal measurements performed at different temperatures T_i , the activation energy can be easily derived from the following equation which simply follows by combining equation 2.83 and 2.84

$$\ln(t_f(T_i)) = \frac{E}{RT_i} + C. \quad (2.85)$$

Here t_f is the time needed to reach a certain transformed fraction and C is a constant. For a set of isochronal measurements $T = \beta t$ performed at different heating rates β , the analysis is more complex. Integration by separation of the variables yields

$$\int_0^\alpha \frac{d\alpha}{f(\alpha)} = \frac{k_0}{\beta} \int_0^{T_f} \exp\left(-\frac{E}{RT}\right) dT = \frac{RE_a}{\beta k_B} \int_{y_f}^\infty \frac{\exp(-y)}{y^2} dy, \quad (2.86)$$

where the substitution $y = \frac{E}{RT}$ was used. Assuming a constant fraction trans-

formed, the left hand side gives a constant. The integral on the right hand side has to be solved using some approximation. Different types of approximations lead to different equations, here the most important ones are listed. For a review containing a more complete list of methods see [Starink04].

The most popular approach is the Kissinger-Akahira-Sunose (KAS) method, where for various heating rates $\ln(\beta T_f^2)$ is plotted against $\frac{1}{RT_f}$ and the activation energy is determined by taking the negative slope of the linear interpolation [Mittemeijer92]

$$\ln\left(\frac{\beta}{T_f^2}\right) = -\frac{E_a}{RT_f} + C. \quad (2.87)$$

A variation with a better accuracy is the type B-1.92 method [Starink03]

$$\ln\left(\frac{\beta}{T_f^{1.92}}\right) = -1.0008\frac{E_a}{RT_f} + C. \quad (2.88)$$

If the rate of transformation at T_f is known it is not necessary to make any approximations. This approach is called Friedman method [Gupta88]. Combining equation 2.83 and 2.84 and taking the logarithm gives

$$\ln\left(\frac{d\alpha}{dt}\right) = -\frac{E_a}{RT_f} - \ln f(\alpha) \quad (2.89)$$

again assuming a constant fraction transformed and $T = \beta t$ leads to

$$\ln\left(\beta\frac{d\alpha}{dT}\right) = -\frac{E_a}{RT_f} - \ln f(\alpha). \quad (2.90)$$

Usually it is very difficult to determine a temperature where a certain fraction has transformed, therefore the peak temperature T_p is used. The peak temperature, i.e. the temperature where the reaction rate is maximal occurs to a good approximation at the same transformed fraction for different heating rates [Mittemeijer92]. Therefore it is justified to use T_p rather than T_f , which also leads to the Kissinger method [Kissinger56, Kissinger57]

$$\ln\left(\frac{\beta}{T_p^2}\right) = -\frac{E_a}{RT_p} + C. \quad (2.91)$$

It should be noted that it is not necessary to assume a specific kinetic model to derive this equation, although this is often read in papers [Starink04].

2.10.4 Reordering

To reorder a disordered material, the atoms have to move to the correct lattice positions, which is energetically favourable and thus energy is released and the DSC curve shows an exothermic peak. The reordering is closely linked to vacancy movement as the migration of vacancies allows the atoms to change positions [Reimann01]. If the alloy is completely disordered before the peak and ordered after the peak, the area under the peak represents the ordering energy [Cahn02].

2.10.5 Recovery

DSC curves can be used to determine dislocation or vacancy densities if the area of the peak related to the annihilation of dislocations/vacancies can be determined [Gao09, Schafler05b]. The energy of the dislocation peak is given by

$$H = Gb^2 \frac{N}{4\pi\kappa} \ln((b\sqrt{N})^{-1}), \quad (2.92)$$

where G is the shear modulus, b the Burgers vector, N the dislocation density and $\kappa = 1 - \frac{\nu}{2}$, with ν being the Poisson ratio. Determining the vacancy concentration is done by dividing the energy of the vacancy peak by the formation energy of a single vacancy. Additionally Kissinger type analysis can be used to determine the activation energies of the recovery processes.

2.10.6 Grain Growth

In normal grain growth, the grains grow reducing the amount of grain boundaries and thus the interfacial free energy. Besides the activation energy of grain growth that can be determined by a Kissinger type analysis of the grain-growth peak, addition of information can be derived using DSC [Chen09, Huang93]. The total energy due to grain boundaries is given by

$$H = \gamma_{GB} \frac{V}{r}, \quad (2.93)$$

where V is the molar volume, r the average grain radius and γ_{GB} the grain boundary energy. Thus if the grain size is known before (r_1) and after (r_2) an exothermic

heat release ΔH , the grain boundary energy can be determined using the equation [Huang93]

$$\Delta H = \gamma_{GB} V \left(\frac{1}{r_1} - \frac{1}{r_2} \right). \quad (2.94)$$

A more advanced analysis can be done by modelling the grain growth. The increase of the average grain radius r with time t can be expressed as [Chen09]

$$\frac{dr}{dt} = \frac{cM\lambda^n\gamma}{r^{n-1}} \quad (2.95)$$

where c is a constant, λ the interatomic distance, γ the interfacial tension and n the grain growth exponent ($n = 2$ would be predicted by theoretical grain growth models, but in practise values between 1.5 and 4 are encountered).

2.10.7 Other Kinetic Models

In general a large variety of kinetic models exist [Christian65, Liu07]. Most of them are based on equations 2.83 and 2.84. The kinetics is described through an appropriate selection of $f(\alpha)$, k_0 and E_a . The most popular model is the Johnson–Mehl–Avrami–Kolmogorov (JMAK) kinetics [Avrami39]

$$\frac{d\alpha}{dt} = K(T)n(1-\alpha)(-\ln(1-\alpha))^{1-1/n} \quad (2.96)$$

or in its integral form

$$\alpha(t) = 1 - \exp(-(Kt)^n). \quad (2.97)$$

The JMAK kinetics can be used for the description of phase transformations and is often applied to crystallization in an amorphous phase. The kinetic exponent n is related to both the nucleation and the growth of the new phase in the old phase (in the case of crystallization the crystalline phase in the amorphous phase). The exponent can be interpreted as the dimension of the growth plus the rate of nucleation. Three dimensional growth (3) and constant nucleation rate (1) would result in $n = 3 + 1 = 4$. It should be noted that there is a set of prerequisites for JMAK kinetics to be applicable, i.e. the processes should be random without heterogeneities and time dependencies. The exponent is determined by a double logarithmic plot of equation 2.97 which directly results in the so called Avrami plot

for an isothermal analysis

$$\ln(-\ln(1 - \alpha)) = n \ln(t) + C. \quad (2.98)$$

For the isochronal case follows after some calculations [Malek95]

$$\ln(-\ln(1 - \alpha)) \approx -\frac{nE_a}{k_B T} + C. \quad (2.99)$$

It is interesting to note that in an isothermal experiment nucleation and growth as expressed by the JMAK kinetics gives a peak (except for the rare case $n < 1$), while normal growth gives a monotonically decreasing signal, thus this is an indication whether nucleation and growth or only growth take place [Chen09].

2.10.8 Experimental Realisation of the DSC Measurements

For the DSC measurements a Netzsch DSC 204 Phoenix was used present in our research group. A Netzsch TASC 414/4 served as controller and cooling was done with a Netzsch CC200 L using gaseous nitrogen. The DSC samples were heated two times from room temperature to 500°C with a rate of 20 K/min and cooled down with a rate of 20 K/min. At the beginning of each heating or cooling step some deviation from the baseline in the form of an oscillation can be noticed, as the device needs some time to reach a linear heating rate. Therefore the very beginning has to be omitted for the final results. As no reversible process occurs in FeAl, the cooling curves contain no information. The DSC curve obtained during the first heating shows exothermic peaks corresponding to processes that release heat. The second heating run was used as a base line (this can be done as no reversible processes are present and all irreversible transformations happened already in the first run). Subtracting the baseline is very important as there is some deviation of the baseline from a straight line, which can influence results when determining peak areas. Before starting with the actual measurements the empty DSC was heated to 500°C and cooled twice to make sure that vapour or other kind of dirt would evaporate. Furthermore care was taken to use only samples with a mass greater than 10 mg to obtain a good signal to noise ratio.

3 Advanced Transmission Electron Microscopy Tools for Nanocrystalline Materials

“Seeing is believing.”

– *Manfred Von Heimendahl*

3.1 Focused Local Profile Analysis by Electron Diffraction

3.1.1 The Need for PASAD

For inhomogeneous nanocrystalline materials [Ciuca10, Sauvage07, Wei02] it is necessary to obtain local quantitative information on the microstructural parameters (e.g.: grain size, domain size and order parameter). Up till now quantitative integral information can be gained by standard X-ray diffraction profile analysis (XPA) methods whereas quantitative local profile analysis of selected features was not readily accessible. For XPA of nanomaterials methods and evaluation procedures have been improved over the past years [Ungar04, Schafner05]. Still, for inhomogeneous nanostructured materials, nanocomposites, nanoparticles or nanolayers [Nanu05] it is necessary to apply new methods for the quantitative characterization of the microstructure on a local scale. Furthermore bulk nanostructured materials made by different methods of severe plastic deformation [Zhilyaev08, Valiev06a, Morris02a] are frequently inhomogeneous [Ciuca10, Sauvage07, Wei02, Revesz06, Morris02b, Peterlechner09b, Rentenberger05, Geist10]. In all these cases where microstructural information of selected features is needed it is necessary to apply TEM methods yielding quantitative results. This is shown in Figure 3.1. Whereas XPA provides an integral information on the sample, quantitative profile analysis of nanomaterials based on electron diffraction can be carried out focused on the areas of interest that are selected in TEM images at high magnifications. To achieve this, a profile analysis of the SAD pattern (PASAD) is carried out.

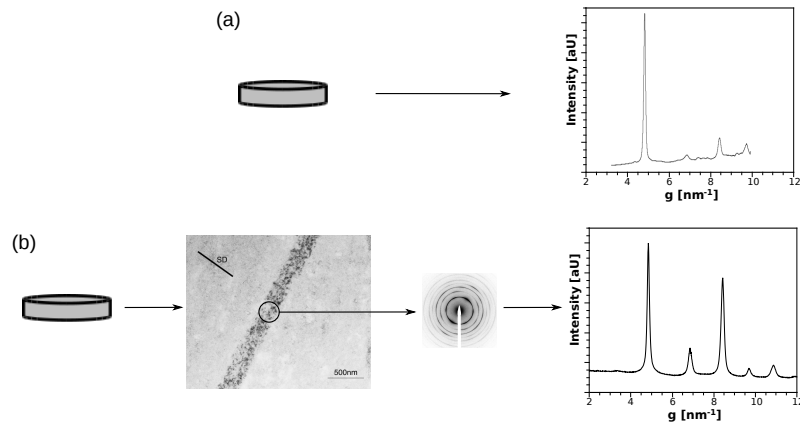


Figure 3.1: (a) X-ray profile analysis provides an integral information on the sample. (b) By using selected area electron diffraction it is possible to perform profile analysis of areas selected in the TEM images.

3.1.2 Performing a PASAD Evaluation

PASAD is performed in three steps: (i) A SAD pattern is recorded from the area of interest. (ii) An intensity profile (intensity versus diffraction vector \vec{g}) can be achieved from the SAD pattern by azimuthal integration. (iii) The microstructural parameters are determined by profile analysis in an analogous way as done in XPA.

To record the diffraction pattern, care has to be taken that the illumination is parallel as a convergent illumination would lead to additional peak broadening. A good approach is to first focus the sample, then go to diffraction mode and use the demagnetize function to reset the lenses. After that it is best to remove the selected area aperture and change the illumination area until the central spot is as sharp as possible. The microscope should always be well aligned and there should not be any astigmatism in the diffraction pattern.

It is also important that the recording device has a sufficient resolution. Figure 3.2 shows the measured peak width for different resolutions of the imaging device. If the resolution is not sufficient the measured peak width is larger than the true peak width. This is usually not a problem for modern CCD cameras. For a quantitative evaluation it is important that all intensities lie in the linear dynamic range of the recording device. Therefore no pixel should be oversaturated but the recording time should be adjusted in such a way that the dynamic range is utilized.

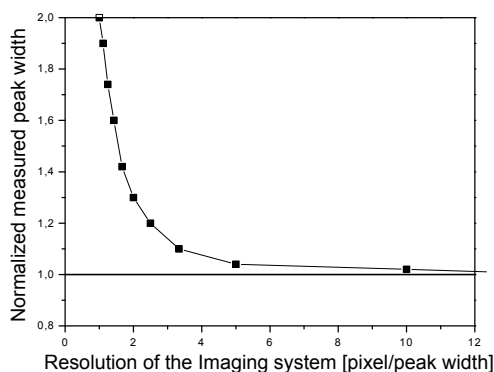


Figure 3.2: Measured peak width divided by the true peak width in dependence of the resolution of the imaging device. If the resolution is not sufficient the measured peak width is larger than the true peak width.

As the central beam is very bright it is best to cover it with the beam stop. Care has to be taken when recording images on a film as the characteristic curve of the film is not linear but has a sigmoidal shape. This is demonstrated in Figure 3.3, where radial averages of two diffraction patterns are shown, one acquired with a rather short exposure time and the second one with a longer exposure time. In the image recorded with a long exposure time, the first strong peak is overexposed whereas in the other case the weak peaks are underexposed.

After having recorded a good diffraction pattern, the azimuthal integration is performed. For this step it is crucial to use the correct centre of integration, as any deviation has a huge impact on the resulting profile. When the centre of integration is the true centre of the SAD pattern, the resulting profile shows sharp peaks (cf. Fig. 3.4a), whereas a deviation from the correct centre of integration can cause artificial peak broadening and even double peaks as shown in Figure 3.4b. Therefore in an implementation of PASAD, special care is taken that the centre is refined automatically by the program. A good method to refine the centre can be deduced from Figure 3.4. Whereas the azimuthal integral shows sharp and thus very high peaks when the centre is correct it shows broad but not so high peaks when the centre of integration is shifted. Thus by shifting the centre around until the peak height reaches a maximum the true centre can be found. Figure 3.5 shows the peak height against the 2D deviation from the true centre for a typical diffraction pattern. It can be seen that the true centre really gives a sharp maximum.

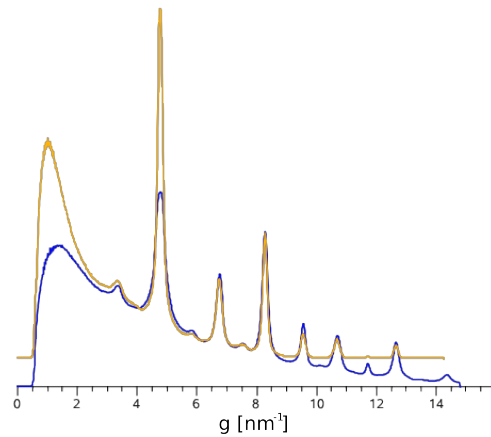


Figure 3.3: This image demonstrates the nonlinearity of conventional films. Radial averages of two diffraction patterns are shown. One acquired with a rather short exposure time and the second one with a longer exposure time. In the image recorded with a long exposure time, the first strong peak is overexposed whereas in the other case the weak peaks are underexposed. The peaks right in the middle of the intensity regime can be trusted. This can be explained as films do not have a linear characteristic curve but rather a sigmoidal one.

The resulting profile can now be used for a profile analysis. As unfiltered electron diffraction patterns show a significant background, the background has to be subtracted. After that the peak parameters of all the peaks can be subtracted from all the Bragg peaks by fitting some peak function (such as a pseudo-Voigt function). These parameters can be used for a profile analysis in the same way as done in X-ray. To ensure reproducibility and to make the routine automatic, it is important to determine the background and fit the peaks automatically using some stable and precise routines.

It should be noted that the resulting peak-widths are a convolution of the instrumental broadening and the broadening due to the sample. Therefore it is important to deconvolute the peak-widths for the instrumental peak broadening. In the present work Voigt deconvolution was used. The deconvolution was performed by recording a diffraction pattern from a single crystalline sample using the same parameters and fitting pseudo-Voigt functions to the diffraction spots. It should be mentioned that there was no significant variation in the width of the diffraction spots or central beam, indicating that there is no significant dependence of the instrumental broadening on the diffraction angle.

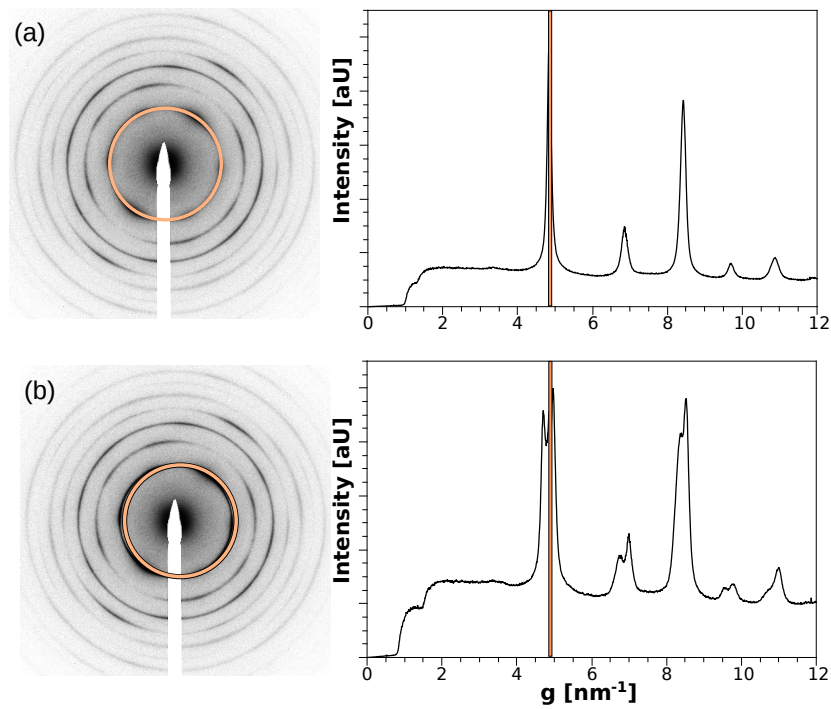


Figure 3.4: (a) When the centre of integration corresponds to the true centre the profile resulting from the azimuthal integration shows sharp peaks. One integration ring is indicated in the diffraction pattern. (b) If the centre of integration is slightly shifted, the resulting profile shows artificial peak broadening or even double peaks.

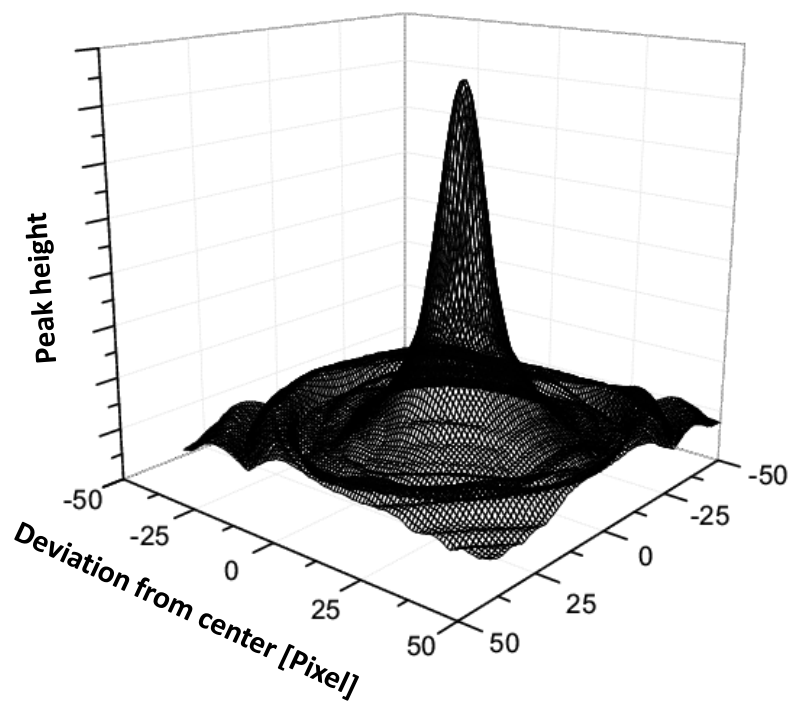


Figure 3.5: Plot showing the peak height observed in the azimuthal integral against the deviation of the centre of integration from the correct centre. As this curve has a sharp maximum it can be used to refine the centre of integration.

3.1.3 The DigitalMicrograph Plugin PASAD-Tools: Functions and Usage

As shown in the previous chapter for a precise PASAD evaluation it is important to use computer assisted routines for the centre determination, the azimuthal integration and the peak fitting. To provide a software for that PASAD-tools was written. It was programmed as a DigitalMicrograph plugin with graphical interface, as this is the most popular software used amongst electron microscopists for recording images. Therefore PASAD can be performed without having to open any additional software. The software can be used free of charge under the condition a reference is made to the publication [Gammer10]. PASAD-tools can be downloaded from the homepage www.univie.ac.at/pasad. If there are any questions, bug reports or feature requests please feel free to contact the author using the e-mail address christoph.gammer@univie.ac.at. For an improved speed the PASAD-tools were programmed in C++, therefore they do not only consist of a DigitalMicrograph script file but also of a dynamic link library. To install the PASAD tools copy the files "PASAD-tools.dll" and "PASAD-tools.gt1" to the DigitalMicrograph plugins directory (C:/Program Files/Gatan/DigitalMicrograph/Plugins). Menu entries called "PASAD-tools" and "PASAD preferences" will be created in the Custom Menu. To uninstall PASAD-tools just delete the files from the DigitalMicrograph plugins directory. Please note that the software provides useful information in the "Results" and "Progress"-windows.

A screenshot is shown in Figure 3.6. Screenshots of the PASAD menu and the preferences menu are shown in Figure 3.7a and b, respectively. The menu offers a variety of functions. Using the dialog box "Adjust image", the SAD pattern can be cropped inverted or calibrated easily. To crop the SAD pattern select the desired region with the DigitalMicrograph ROI tool and press "Crop Image", the SAD pattern can be calibrated to reciprocal lattice distance in crystallographer units. The calibration menu (cf. Fig 3.7c) provides different methods: (i) If a scanned film or imaging plate is used, the user has to enter voltage, camera length and resolution (in dpi) to calibrate the image. (ii) For a CCD camera this is done by providing the pixel size, camera length and acceleration voltage. (iii) There is also the possibility to define two custom microscopes and calibrate different camera lengths for these microscopes. After this was done, the user only has to enter the voltage and select the camera length for the desired microscope. Up to ten camera lengths can be calibrated for each TEM. To calibrate a camera length, use a known specimen, measure the position of a known reflection in pixel (R),

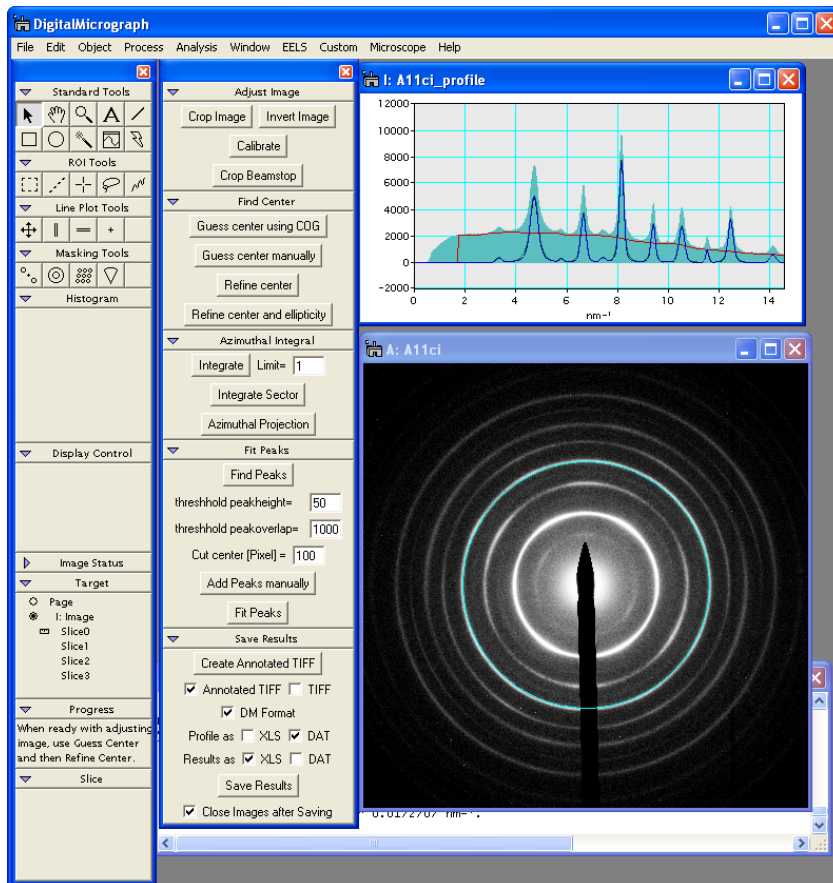


Figure 3.6: Screenshot of the software PASAD-tools. The software provides a graphical user interface for all functions and is fully integrated into DigitalMicrograph.

calculate the reciprocal lattice distance (g) and calculate the ratio (g [nm^{-1}])/(R [Pixel]) to get the calibration factor. As this value also depends on the voltage it has to be multiplied with the wavelength [nm] at which the calibration was performed. Now enter the camera length together with the corresponding calculated value (calibration-wavelength). Repeat this for all desired camera lengths. (iv) Furthermore the software offers the possibility to calibrate the SAD pattern from a known distance. This is done by selecting a reflection with a known reciprocal lattice distance either in the SAD pattern or in the integrated profile. The script tries to get as much information as possible from the image tags. The calibration is written to the image. If a calibration is already present, it will be used.

Furthermore the beamstop can be cropped, which is very important if integration with high precision is performed. As the beamstop influences the integration it is important to crop the beamstop (cf. Fig. 3.8). There are two different possibilities: (i) Select “Crop Beamstop” and click on a point of the beamstop. All points with intensities lower than the intensity at this pixel multiplied with a factor (crop-beamstop factor) will be set to 0. The selected region will be dilated by a certain amount (dilate beamstop) in order to exclude the edge of the beamstop. Both values can be changed in the PASAD preferences. (ii) Use the DigitalMicrograph Magic Wand tool to select the beamstop (the region indicated in the histogram can be changed for fine-tuning). When ready select “Crop Beamstop”.

Using the dialog box “Find center”, the centre of the SAD pattern can be found (cf. Fig. 3.9). A guess for the centre can be selected manually using the ROI (region of interest) tools; either using the cross or by drawing a square around it. A second possibility of selecting the centre manually is to draw a circle along a ring. The centre can also be guessed by choosing three points on a ring. The centre can also be guessed automatically using the centre of gravity (COG). The guess will be indicated by drawing a circle along the strongest ring. The ring can be changed manually if wanted. After guessing the centre, the centre can be refined to a sub-pixel precision using “Refine Center”. If no centre was guessed, the middle of the image will be used as a first guess. For a roughly centred SAD pattern this is usually sufficient. The centre refinement is done using the Downhill-Simplex-algorithm. The most intense ring is chosen, and the centre of integration is moved until the peak in the azimuthal integral is maximally sharp, which is the case if the peak height reaches its maximum as explained in the previous chapter. The method is extremely fast (about a second per image) and very robust. It can also

be applied to sectors of SAD patterns, that can be very useful if higher orders are to be studied without losing the possibility of determining the peak width precisely. Furthermore it gives much better results than fitting a circle into a ring or using the Hough Transform. In addition to refining the centre, the distortion of the projector lens, which can lead to an elliptical diffraction pattern, can be corrected by integration along an ellipse instead of along a circle. Distortion correction is also done using the Downhill-Simplex-algorithm. The orientation and distortion of the ellipse are varied until the integral gives a maximum. The refined centre and elliptical distortion will be written into the Image Tag of the SAD pattern using the same convention as used by Diffpack. To use some manual values simply edit this Tags.

After having a precise centre, the azimuthal integration can be performed using the dialog box “Fit peaks”. This can either be done using the whole image or just a sector between two angles (e.g. from 45° - 90°). The angles are measured in the mathematical sense (anti-clockwise, starting from the x-axis). The resulting diffraction profile will be normalized so that the maximum value is set to 10000. To obtain an azimuthal average rather than an azimuthal integral press the “Integrate” button while holding the ALT key. It is also possible to map the diffraction pattern to an image containing radius vs. angle by selecting “Azimuthal Projection” (cf. Fig. 3.10). Holding the ALT button gives a full resolution image.

Now that the electron diffraction profile was obtained by azimuthal integration, the dialog box “Fit peaks” allows fitting peaks to the profile. In a first step the desired region has to be selected using the region of interest tool. After that the peaks can be determined automatically using the “Find Peaks” button. The peakheight threshold determines the minimum height necessary for a peak to be detected. Splinepoints are put in between the peaks if the peaks do not overlap, which is determined by the peak-overlap threshold. The background determined by a monotone piecewise cubic spline is subtracted from the profile. The peaks are pre-fitted using a Voigt peak-fit and peaks as well as the background are plotted (cf. Fig. 3.11). It is also possible to add and delete peaks or splinepoints manually. After selecting “Add Peaks manually” peaks are indicated by ROIs and splinepoints are indicated by small circles in the profile (cf. Fig. 3.12). To add a peak click on the desired position using the left mouse-button. Click on a peak using the left mouse-button while holding ALT to delete this peak. To add a splinepoint click on the desired position using the middle mouse-button. Click on a splinepoint using the middle

mouse-button while holding ALT to delete this splinepoint. When ready press ESC. For help press “h”. When ready select “Fit peaks” to fit a model including all the peaks to the background subtracted profile. The splinepoints are moved according to the value of the fit and a second fit is performed to the corrected profile. Peak-parameters are stored in a hidden image. As all images are found by their name it is important not to change any image names or close the hidden images.

PASAD-tools provides various possibilities to save the results using the dialog box “Save results”. By selecting “Create Annotated TIFF” a SAD pattern with an inserted background subtracted profile is created (cf. Fig. 3.13). Furthermore the profile and the peakparameters can be exported as Excel-sheet or DAT-file (Exporting a large amount of data to an Excel sheet can take some time). It is possible to save all data at once by selecting the desired points in the dialog.

3.1.4 Outlook

In addition to the focused local profile analysis of inhomogeneous nanocrystalline (NC) materials, PASAD can be applied to study ultrathin NC films and nanoparticles where standard X-ray investigations yield an insufficient signal to noise ratio. The reason is that for electron diffraction the diffracted intensity is about a factor 10^4 larger than that of XRD which corresponds to the difference of the scattering factors. Due to the short exposure times needed, electron diffraction also facilitates a quick and detailed focused analysis including the possibility to obtain 3D information by tilting the sample and to perform in-situ TEM experiments (e.g. in-situ deformation or heating) with time resolved parameters. This is currently achieved with synchrotron experiments [Budrovic04]. Still, most important is the possibility in the TEM to combine the information gained from the image mode by taking bright-field or dark-field images of a selected region with the PASAD information of exactly the same region. This makes the interpretation of the results obtained by diffraction straightforward and more precise. Investigations of the local variations of the degree of long-range order are possible by studying the diffraction rings of superlattice reflections. The analysis of diffracted rings of amorphous material [Borisenko09] is another potential application for PASAD, since in the case of diffuse rings it is not trivial to determine their centre exactly. In general, PASAD is a very powerful method for quickly analysing NC materials quantitatively on a local scale by correlating the results with regions specifically selected by TEM images. Finally, the method is extendible and due to its clear and automatic routine

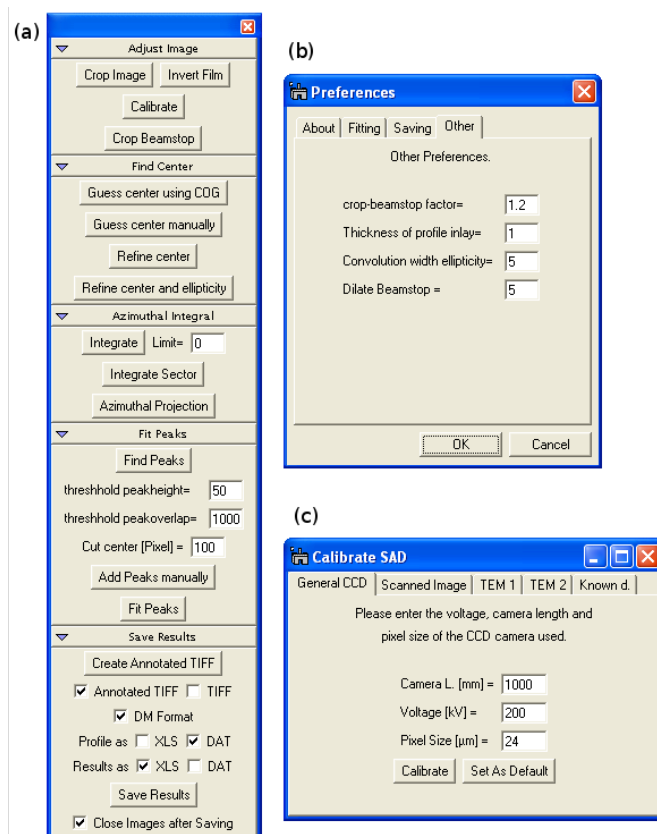


Figure 3.7: Menus of the software PASAD-tools. (a) The main menu is opened as a side bar and contains all functions that are needed. (b) In the preferences default values can be adjusted. (c) The dialog for the calibration of SAD patterns contains various methods.



Figure 3.8: The software PASAD-tools allows to crop the beamstop.

it has the potential for a broad spectrum of applications.

3.2 Dark Field Scanning

For a precise grain size determination it is important to measure local orientation variations in a material. Electron backscatter diffraction (EBSD) used in scanning electron microscopes (SEM) offers a simple automatic method to obtain orientation maps of large sample areas with grain sizes down to 100 nm [Humphreys04]. Still for HPT deformed FeAl the small grain size and the large density of dislocations demand for a method with a greater spacial resolution. A TEM offers a much better resolution as compared to a SEM, therefore the development of a method that allows to generate orientation maps in a TEM is of big interest for the characterization of nanocrystalline materials [Wu09]. Furthermore the TEM offers the possibility to image the microstructure in addition to mapping the crystal orientations.

One approach for orientation imaging in the TEM is to use convergent beam electron diffraction with a small convergence angle. By scanning across the sample and evaluating the recorded diffraction pattern it is possible to generate an orien-

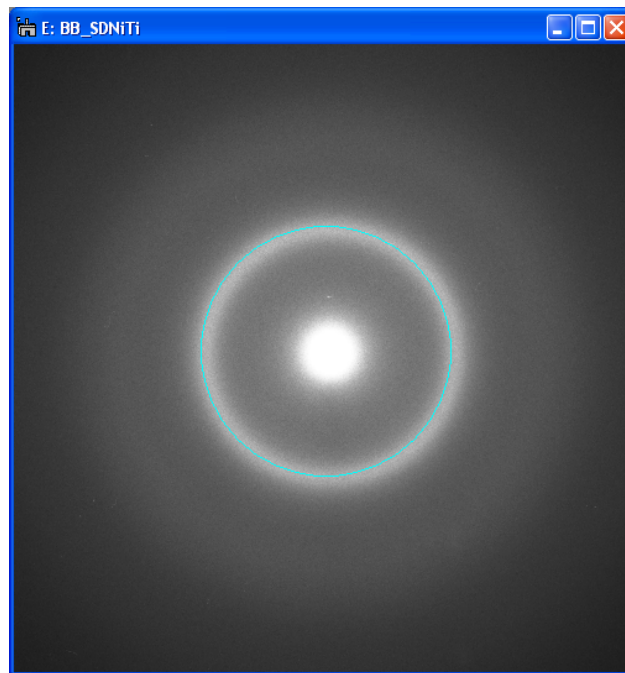


Figure 3.9: PASAD-tools refines the centre automatically. To allow the user to check if the centre has been detected correctly, the brightest ring is marked.

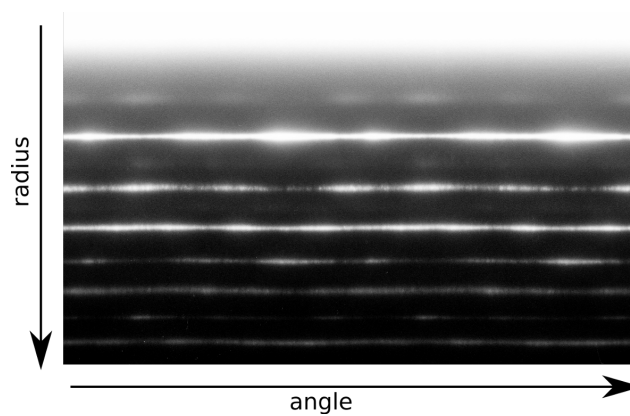


Figure 3.10: PASAD-tools allows to map the diffraction pattern to a radius against angle plot.

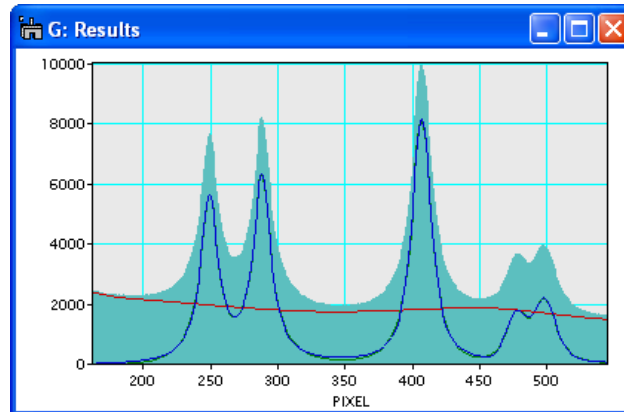


Figure 3.11: Typical diffraction profile obtained after fitting in PASAD-tools. The filled curve represents the raw data, the background is indicated by a line, the curve-fit (green) shows a very good agreement with the background subtracted data (blue) therefore these two curves are not distinguishable.

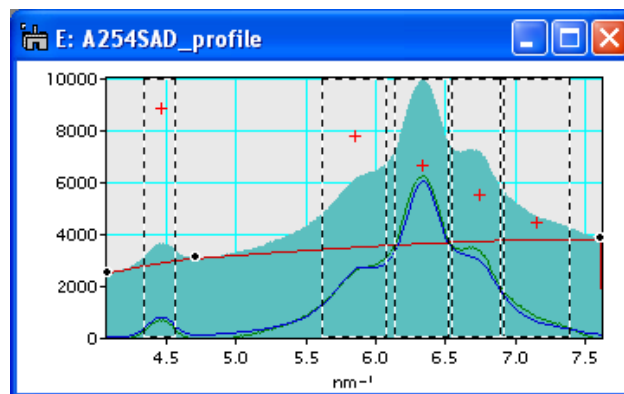


Figure 3.12: For the “Add Peaks manually” function peaks are indicated by ROIs and splinepoints are indicated by small circles in the profile. By using the mouse, peaks and splinepoints can be moved, added or deleted.

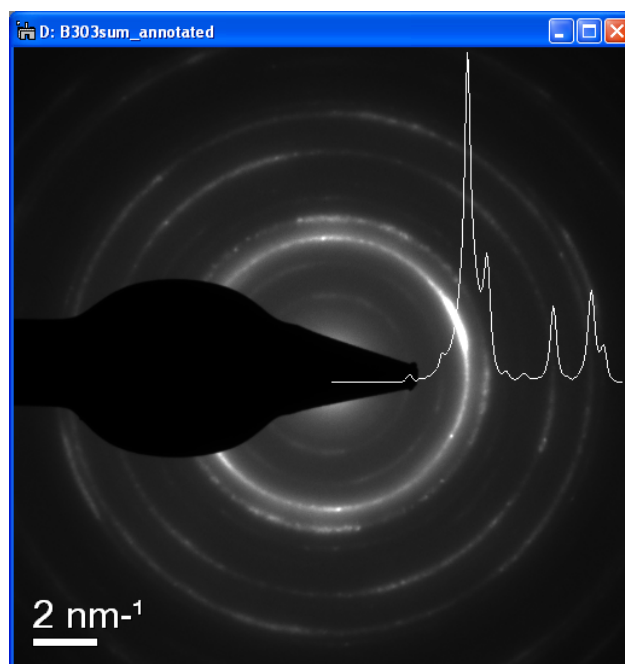


Figure 3.13: PASAD-tools provides the possibility to create automatically an annotated diffraction pattern containing a scale bar and an overlaid profile.

tation map. A commercial implementation of this method is available [ASTAR]. This approach scans in the real space and records in the reciprocal space similar to the way EBSD works in the SEM.

An alternative and very elegant approach is to scan in the reciprocal space and record in the real space also recording the full data cube [Dingley06, Liu11]. Figure 3.14 shows a schematic representation of this method. In conventional diffraction the problem is that many grains give rise to diffraction spots leading to the typical ring pattern that is observed in SAD diffraction of nanocrystalline materials. Two grains are highlighted in this schematic drawing (one in dark grey and one in light grey) both of which give rise to a spot pattern, that is hidden in the diffraction pattern (cf. Fig. 3.14a). When using dark-field imaging, a grain only lights up if the aperture position lies on a diffraction spot. In Figure 3.14b the aperture position is on a diffraction spot corresponding to the dark grey grain and thus only this grain lights up. The same is valid in Figure 3.14c for the light grey grain. By taking dark-field images with the aperture position moving across the entire reciprocal space it is possible to reconstruct a diffraction pattern for each pixel in the real space. This is simply done by examining at which aperture positions the pixel is lighting up.

Therefore for a practical implementation of orientation imaging by dark-field scanning, a large set of dark-field scanning has to be acquired. This was achieved by writing a DigitalMicrograph script that uses the tilt coils to acquire tilted dark-field images from a selected range of the reciprocal space. The images are stored to a selected folder, while all parameters are recorded as image tags. To correct for drift, bright-field images are recorded in between the dark-field images and using a cross correlation allows to calculate the drift. To reconstruct a diffraction pattern, a set of areas can be selected in the bright-field area and diffraction patterns are reconstructed from the dark-field images. After recording the full set of dark-field images it is therefore possible to do “selected area diffraction” from areas with an arbitrary shape and a size down to a nanometre. Indexing the reconstructed diffraction patterns allows to do orientation imaging down to a nanometre resolution. It should be noted that a big limitation of orientation imaging is the overlapping signal of overlapping grains, which can be overcome by using very thin samples in the TEM.

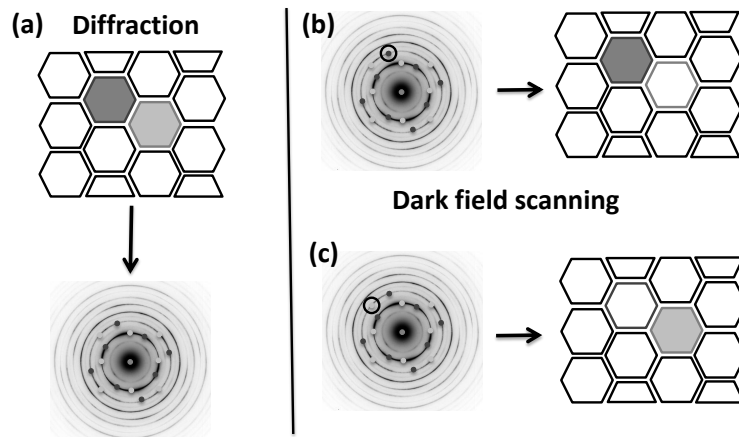


Figure 3.14: Diffraction pattern reconstruction by dark-field scanning. (a) Two grains are highlighted in this schematic drawing (one in dark grey and one in light grey) both of which give rise to a spot pattern, that is hidden in the diffraction pattern. When using dark-field imaging, a grain only lights up if the aperture position lies on a diffraction spot. (b) The aperture is sitting on a diffraction spot corresponding to the dark-grey grain and therefore this grain lights up but the light grey grain does not light up. (c) If a diffraction spot corresponding to the light-grey grain is selected the situation is the other way round. Therefore it is possible to reconstruct a diffraction pattern for a grain by evaluating at which dark-field images it lights up.

4 Nanocrystallisation of FeAl by High Pressure Torsion Deformation¹

“There is plenty of room at the bottom.”

– Richard Feynman

4.1 Evolution of the Nanocrystalline Structure

4.1.1 TEM Investigations

HPT can be used as a method of severe plastic deformation to make a bulk nanocrystalline material since a gradual grain refinement is expected to occur with increasing deformation [Zhilyaev08]. When deforming single crystalline FeAl, the situation is rather different. This is shown by preparing TEM samples of HPT discs deformed to different deformation grades. The TEM bright-field images and corresponding SAD patterns shown in Figure 4.1 illustrate the evolution of the nanocrystalline structure as a function of shear strain γ . At $\gamma = (1200 \pm 300)\%$ narrow bands containing a nanocrystalline (NC) structure are observed (cf. Fig. 4.1a and b). At this strain the volume fraction of the NC structure is small ($\sim 1\%$ of the specimen as estimated from TEM images). With increasing γ , the volume fraction of the NC material increases and is $\sim 50\%$ at $\gamma = (2300 \pm 400)\%$ (cf. Fig. 4.1c and d). At $\gamma > 5000\%$ the whole volume of the specimen contains the NC structure, this is shown in Figure 4.1e and f corresponding to $\gamma = (7100 \pm 1100)\%$. The TEM bright-field images show that the grain boundaries in the NC structure are not

¹ A detailed treatment of the inhomogeneous formation of the nanocrystalline structure can be found in [Mangler09]. The results included in this chapter were published in the following peer-reviewed papers:

- The quantitative focused profile analysis in [Gammer10].
- The the 3D analysis of the nanocrystalline structure in [Gammer11b].

well defined which is typical for nanocrystalline materials made by severe plastic deformation [Zhilyaev08, Rentenberger04].

4.1.2 Using PASAD for a Focused Local Analysis

It is very surprising that the evolution of the nanocrystalline structure occurs in a non-homogeneous way. To study the evolution in more detail it is the aim to analyse locally the nanocrystalline structure as a function of strain and to determine quantitatively the evolution of the coherently scattering domain (CSD) size. In chapter 3.1 it was shown that quantitative local profile analysis of nanomaterials based on electron diffraction can be carried out focused on the areas of interest that are selected in TEM images at high magnifications using PASAD.

For the quantitative local analysis focused on the regions containing the NC structure, SAD patterns (cf. Fig. 4.1b,d,f) were taken from the areas of interest selected in the TEM images (cf. Fig. 4.1a,c,e). The SAD patterns of the NC material show rings as grain orientations are randomly distributed in the sample; as compared to the undeformed material the superlattice reflections are missing (e.g. $\{100\}$), which indicates that the NC material is disordered in contrast to the starting material that is B2 long-range ordered. The peak profiles obtained by azimuthal integration of the SAD patterns from the samples deformed to different strains are shown in Figure 4.2, the profiles are used for the following analysis. The strong interaction of electrons with matter leads to a very high signal to noise ratio and thus to a smooth profile. The peaks are rather broad indicating that the CSD size is small.

The full width at half maximum (FWHM) of the peaks was determined from the fitted curve using the PASAD-tools. The evaluation can also be carried out focused on other parameters, e.g. the integral width. The instrumental peak broadening was deduced from spots of undeformed material. To compensate for it, all values of the NC structures were deconvoluted with the instrumental peak broadening, leading to the corrected FWHM. To obtain a good statistical analysis at least 10 SAD patterns were analysed for each sample and the mean value and the standard deviation were calculated. The SAD patterns were recorded from different areas having a diameter of 180 or 910 nm.

The volume weighted mean CSD size ($\langle D \rangle_V$) was calculated from the corrected FWHM (Δg) of the diffraction peaks using a Williamson-Hall plot [Williamson53] (cf. Fig. 4.3). For the Williamson-Hall plot only the $\{110\}$, $\{211\}$ and $\{220\}$

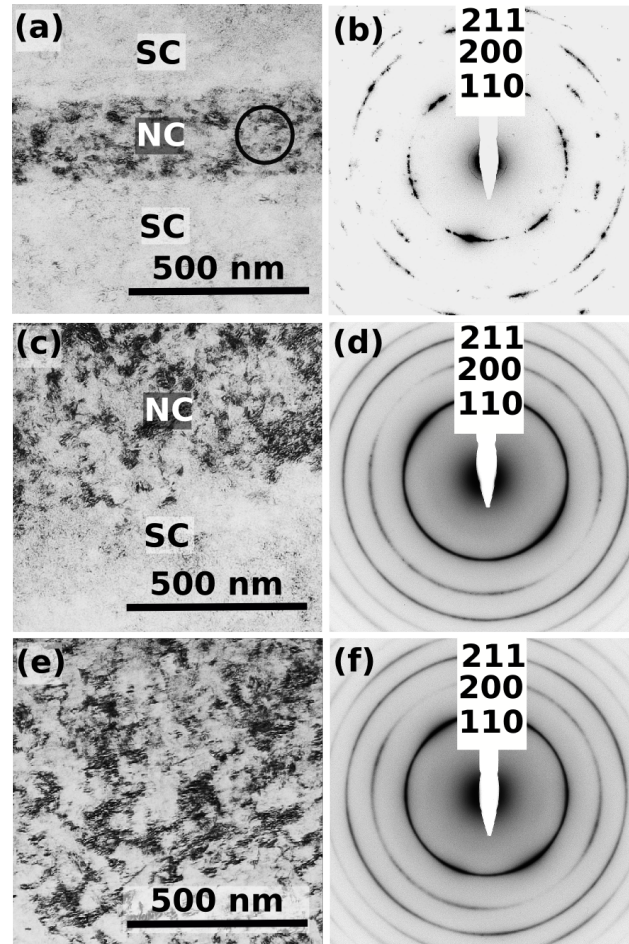


Figure 4.1: TEM study of the NC structures occurring in HPT deformed FeAl as a function of shear strain γ . (a) $\gamma \sim 1200\%$; bright-field (BF) image showing a band containing disordered NC material embedded in the single crystalline (SC) material. (b) SAD of the area indicated in (a). (c) $\gamma \sim 2300\%$; the BF-image shows two distinct structural phases: NC and SC. (d) SAD of the NC region of (c). (e) At $\gamma \sim 7100\%$ the sample is homogeneously NC. (f) SAD of (e).

peaks were used; the $\{200\}$ peaks were not considered, as the anisotropic strain broadening caused by dislocations leads to a higher strain broadening for the $\{200\}$ reflections than for the other ones [Ungar99]. (The lines represent linear regressions through the $\{110\}$, $\{211\}$ and $\{220\}$ reflections.) Details on the Williamson-Hall plot are given in chapter 2.6.8. As the grains are highly fragmented (cf. Fig. 4.1), the relevant size obtained in peak broadening analysis represents the CSD size and not the grain size [Schaffler05]. In NC materials effects of dynamic diffraction are small as the CSD size is small compared to the extinction length. Still dynamic effects can influence the intensities of diffracted beams but they do not influence this analysis. In the present case the intensities and not the width of the peaks are affected since integrating over peaks with different intensities but equal peak width yields the same peak width.

Using PASAD we obtain CSD sizes of 15 ± 3 , 17 ± 3 and 18 ± 4 nm for the samples deformed 1200, 2300 and 7100%, respectively. As the CSD size does not change significantly with the deformation, it is concluded that the nanograins are not further refined during the deformation. This means that the NC regions locally formed during the early stages of deformation ($\gamma \sim 1200\%$) must have similar structures as the homogeneous NC materials finally achieved at high strains ($\gamma > 5000\%$).

For the homogeneous nanocrystalline sample the PASAD results can be compared with those from X-ray measurements of the CSD size, leading to a good agreement (18 ± 4 nm using PASAD and 14 ± 7 nm using XRD). This demonstrates that electron diffraction is a valid tool for determining quantitative CSD sizes of selected local regions in NC materials. Analysing the grain sizes statistically directly from the TEM images would not have been an alternative, since due to the severe plastic deformation the grains are frequently fragmented and have highly irregular fuzzy grain boundaries (cf. Fig. 4.1). This makes segmentation very difficult and it is further disturbed by strong moiré effects of overlapping nanograins frequently observed in TEM images of bulk NC materials [Rentenberger04].

4.1.3 Modified Williamson-Hall Plot

With the installation of a new CCD camera on the CM200 it became possible to record diffraction patterns up to higher reflections. Figure 4.4a shows an electron diffraction profile deduced from the SAD ring pattern of homogeneously nanocrystalline sample by azimuthal integration. Seven fundamental reflections (indicated

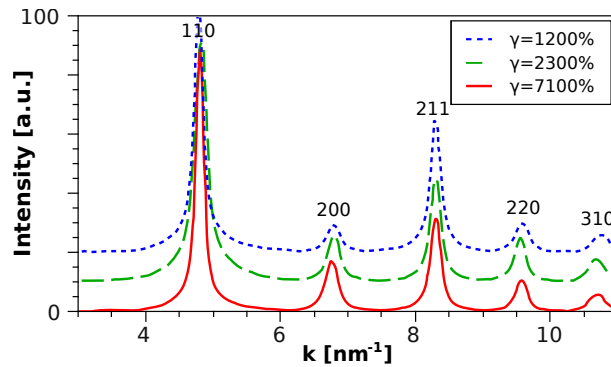


Figure 4.2: Background subtracted diffraction profiles of the NC regions in FeAl deformed by HPT to shear strains of 1200, 2300 and 7100%, respectively. The three profiles are very similar indicating that the NC structure does not change with increasing shear strain.

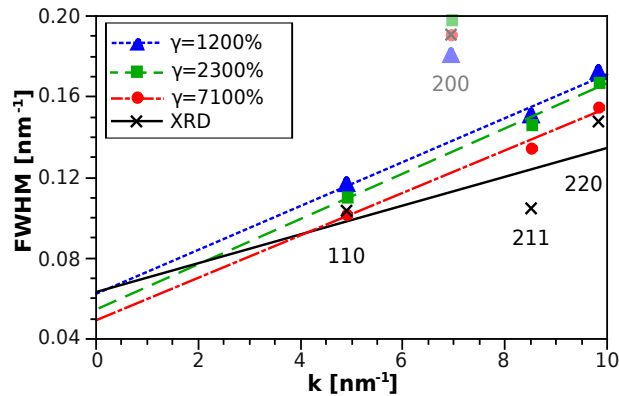


Figure 4.3: Williamson-Hall plot of the NC regions in HPT-deformed FeAl to separate the size broadening from the strain broadening. From the size broadening the median CSD sizes were calculated indicating that the samples with different shear strains have similar CSD sizes. The resulting CSD sizes are 15 ± 3 , 17 ± 3 and 18 ± 4 nm for the samples deformed 1200, 2300 and 7100%, respectively. The latter is consistent with the CSD size determined by X-ray diffraction (14 ± 7 nm). The {200} reflections were not considered as they show a higher strain broadening from dislocations than the other reflections [Ungar99].

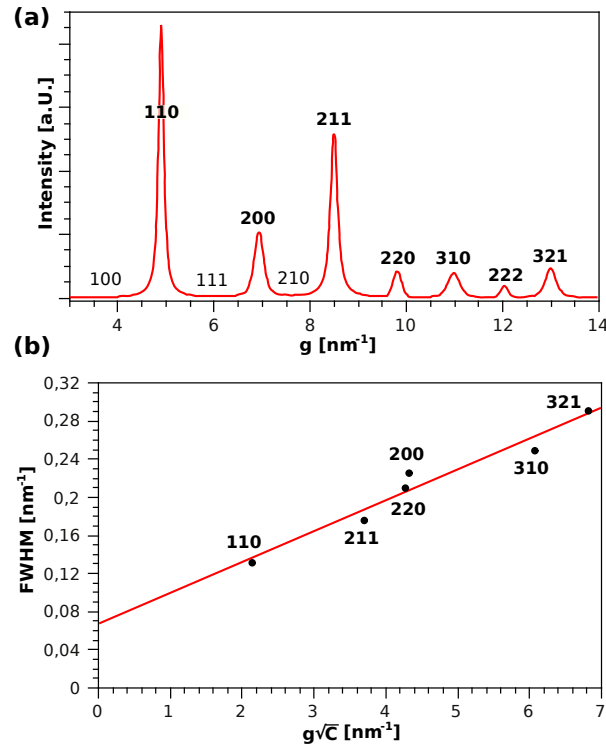


Figure 4.4: (a) Diffraction profile of nanocrystalline FeAl produced by high pressure torsion. The diffraction profile was deduced from a SAD pattern taken from the plan view of the sample. (b) Corresponding modified Williamson-Hall plot. The volume weighted mean coherently scattering domain size ($\langle D \rangle_V$) can be calculated from the intercept corresponding to the size broadening.

in bold) are visible, the superlattice reflections are absent as the sample is disordered. To further increase the precision, a modified Williamson-Hall was used, where the contrast factors of the dislocations [Ungar99] are taken into account (cf. chapter 2.6.8). Figure 4.4b shows the modified Williamson-Hall plot deduced from the electron diffraction profile shown in Figure 4.4a. The solid line represents the linear regression. From this analysis a resulting $\langle D \rangle_V = 20 \pm 2$ nm is deduced. The error was calculated from the linear regression. This value is slightly different from the value determined in the previous chapter as the modified Williamson-Hall plot was used. Although this value is more accurate it should be noted that the results presented in the previous chapter still remain valid as they were mainly used for a comparison between the different nanocrystalline regions.

Microscope	untilted	tilted to +30°
CM200	20 ± 2 nm	18 ± 1 nm
G20	20 ± 1 nm	17 ± 2 nm
G20, energy filtered	19 ± 2 nm	18 ± 2 nm

Table 4.1: Comparison of the volume weighted mean CSD size obtained from different microscopes at two different tilt positions

4.1.4 Reproducibility of the PASAD Analysis

To check the dependence of the CSD size on the acquisition parameters, SAD patterns were recorded from sample areas with different thicknesses and using different illuminated areas. The results did not differ significantly, but by using thicker samples an increased background can be noted. The area of diffraction that can be used is limited by the maximum size of parallel illumination in the TEM.

To exclude any influence of inelastic scattering on the measured peak width energy filtered SAD patterns were recorded with a slit width of 1 eV for both, an untitled position and a position where the sample was tilted to +30°. Integrating the entire SAD pattern, the volume weighted mean CSD size was determined. For a comparison the energy filter was switched off and the measurement was repeated. As shown in Table 4.1, the values measured on the Tecnai G20 lie within the errors of the values obtained on the CM200 when the instrumental peak broadening is taken into account. This indicates that neither energy filtering nor the microscope used have much influence on the results of the measured CSD size. It should be mentioned however that energy filtering leads to a reduction of the background in the diffraction profile. This might be beneficial for complicated profiles with overlapping peaks, where it is not straightforward to subtract the background.

4.2 3D Analysis of the Nanocrystalline Structure

4.2.1 TEM Investigations

The TEM studies presented previously have been based on plan view samples only and provide only information on a projection of the nanostructures. Also in literature most TEM investigations of samples made by HPT have been based on plan view samples only, probably due to experimental difficulties in preparing cross-section TEM specimens of the rather thin HPT samples. Still, for nanocrystalline structures with non-equiaxed grains, the analysis of different TEM sections would

be necessary for a 3D analysis of the nanostructures [Huang07, Peterlechner09b]. Therefore as described in chapter 2.3 from the deformed samples TEM specimens were cut in two different ways: (i) plan view sections and (ii) tangential cross sections both of them correlated to the geometry of the deformed samples in a given way. The tangential cross section has its plane normal parallel to the radial direction of the HPT disc.

Figure 4.1e,f shows a bright-field image and diffraction pattern of a TEM specimen of HPT deformed FeAl having plan-view orientation. The specimen is nanocrystalline, the grain boundaries are not well defined and the grains are about equiaxed and contain a high density of defects. The contrast features observed are dominated by strong moiré effects [Rentenberger04]. Figure 4.5 shows a bright-field and dark-field image of a tangential cross section of HPT deformed FeAl. The grains are elongated in the shear direction indicating that the grains have a platelet shape. The platelets lie almost parallel to the shear plane in the HPT disk (their inclination angle is only $\sim 10^\circ$). The nanocrystalline grains are rather homogeneous in size, show fuzzy non-equilibrium grain boundaries and a high density of defects. An estimation of the size of the grains from the TEM images shows that the grains have a length of about 80 ± 20 nm and a height of around 20 ± 10 nm, which is in good agreement with previous studies on HPT deformed FeAl [Mangler10].

The contrast features in the TEM bright-field image of Figure 4.5a are complex, but when comparing them with the TEM image taken from plan view (cf. Fig. 4.1e) it is clearly visible that moiré effects are less dominant in the cross section image. In plan view the platelet shaped grains overlap very strongly whereas in the cross section view the platelets are standing vertically expanding in many cases through the entire TEM foil. Therefore, it can be concluded that TEM images from the cross section are necessary to study features that are linked to the shear plane.

Figure 4.5b shows a TEM dark-field image taken from the same region as Figure 4.5a. The dark-field image was recorded using a small section of the $\{110\}$ reflection ring. To avoid complex contrasts from neighbouring orientations, a small aperture was used for imaging (0.6 nm^{-1} diameter in reciprocal space). A comparison of the TEM bright-field image with the dark-field image shows that isolated regions lighting up in the dark-field image are much smaller than the grains seen in the bright-field image. Therefore it can be concluded that the grains contain substructures caused by the high density of dislocations, e.g.: small-angle grain boundaries.

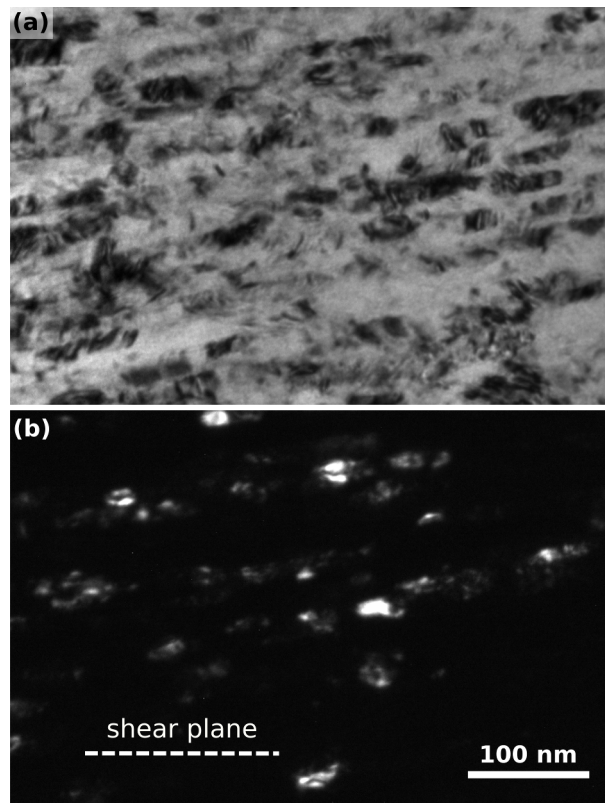


Figure 4.5: Tangential cross-section of high pressure torsion deformed FeAl. (a) TEM bright-field image showing elongated grains. (b) In the TEM dark-field image taken from the same region small areas show up that correspond to coherently scattering domains. The shear plane is indicated by a dashed line.

4.2.2 3D Analysis by Electron Diffraction

Figure 4.6a shows a proposed average shape of a CSD. From the top view the CSD is equiaxed whereas in the cross-section it is elongated. The value of $\langle D \rangle_V$ deduced from the profile analysis represents the CSD size parallel to the diffraction vector, i.e. the volume weighted size of horizontal cuts through the CSD. When the CSD is untilted, it is cut through its longest axes and the resulting $\langle D \rangle_V$ value has its maximum. When tilting the sample (cf. Fig. 4.6b), the value of $\langle D \rangle_V$ is reduced.

To obtain a quantitative information on the average CSD size in 3D it is necessary to analyse each SAD pattern along the tilt axis and the axis normal to that separately. As shown in Figure 4.6a and b, $\langle D \rangle_V$ measured along the tilt axis (indicated by f) does not change when tilting the sample, whereas for an elongated CSD $\langle D \rangle_V$ measured along the axis normal to the tilt axis (indicated by e) is reduced. Therefore, two sets of diffraction profiles were deduced from selected regions of the SAD patterns only. As shown in Figure 4c a region of 10 degrees around the tilt axis was taken into account and in addition a region around the axis normal to that. For both sets of diffraction profiles a modified Williamson-Hall plot was used to determine the volume weighted mean CSD size.

Figure 4.7a shows the plot of $\langle D \rangle_V$ measured in the direction normal to the tilt axis as a function of the tilt angle. A plan view specimen was used and SAD patterns were recorded within a large range of tilt angles: Tilting angles of the incident beam ranging from -52.5° to $+52.5^\circ$ in steps of 5° were applied. Assuming that the CSD has an ellipsoid shape allows to calculate the variation of $\langle D \rangle_V$ with the tilt angle. The model for ellipsoidal shaped CSD is fitted to the experimental data (cf. solid line in Fig. 4.7a) showing a good agreement. From the fit it is deduced that the platelet shaped CSD have a length of 18 ± 1 and a height of 10 ± 1 nm. This leads to an aspect ratio of 1.8. Figure 4.7b shows the plot of $\langle D \rangle_V$ against the tilt angle for the measurement along the tilt axis. The data show some scattering but no trend can be deduced. As expected, $\langle D \rangle_V$ measured along the tilt axis does not change when tilting. The mean of all data points is 19 ± 2 nm. Therefore it can be deduced from the diffraction analysis that the assumption of an ellipsoid average shape for the CSD is valid and that the CSD has a width of 19 ± 2 nm, a length of 18 ± 1 nm and a height of 10 ± 1 nm.

The method presented here allows to determine the average width of the CSD in 3D by evaluating the SAD pattern along different directions with respect to the tilt axis for a large range of tilt angles. The fact that $\langle D \rangle_V$ measured along the

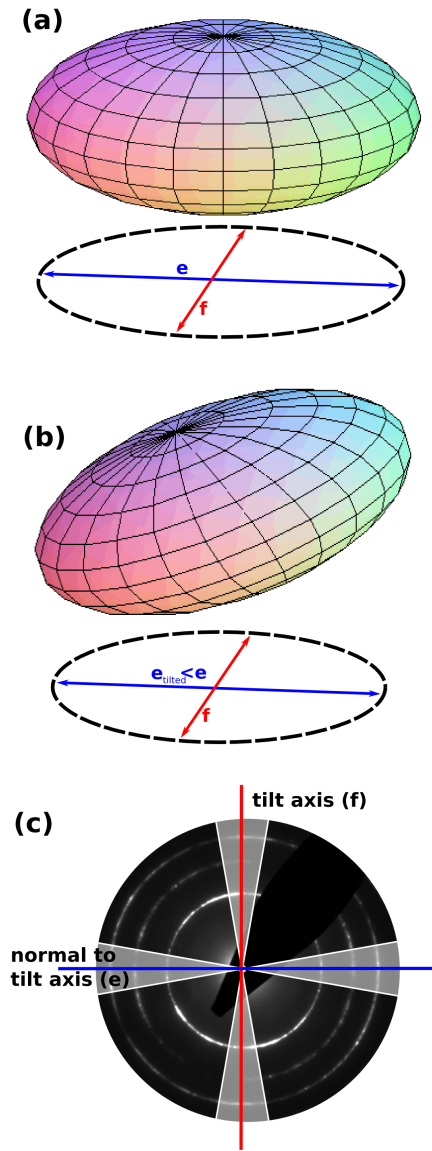


Figure 4.6: Schematic representation of a platelet shaped ellipsoidal CSD. The effect of tilting on the measured volume weighted mean coherently scattering domain sizes ($\langle D \rangle_V$) is shown. (a) $\langle D \rangle_V$ measured in the direction of the tilt axis f and the direction normal to that e are shown. (b) Tilting the sample leads to a reduction of e whereas f stays constant. (c) The regions of the SAD pattern used for the evaluation of e and f are shown.

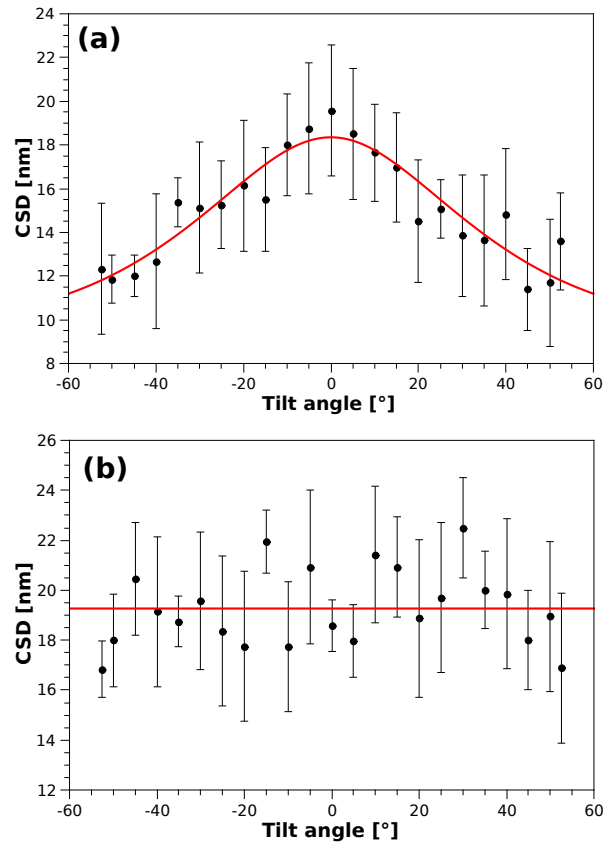


Figure 4.7: Variation of the volume weighted mean coherently scattering domain (CSD) sizes ($\langle D \rangle_V$) with the tilt angle. (a) $\langle D \rangle_V$ measured along the axis normal to the tilt axis (cf. axis e in Fig. 4.6). The line is calculated for ellipsoidal CSD and shows good agreement to the experimental data. (b) $\langle D \rangle_V$ measured along the tilt axis (cf. axis f in Fig. 4.6). No clear trend of the change with the tilt angle is observed. The solid line represents the mean value.

tilt axis does not change when tilting while a large change is seen when measuring along the axis normal indicates the validity of the method. While the elongation of the average CSD size could have been determined by using less tilting angles, the fine sampling has the advantage of reducing the error of the overall measurement. Using TEM for the diffraction experiment allows a quick and automatic acquisition of tilt series due to the short exposure time needed to collect diffraction patterns and the possibility to use scripting for the microscope control [Kolb07].

The quantitative 3D result of Figure 4.7 confirms the estimate resulting of the dark-field image of the specimen with cross section view (cf. Fig. 4.5b). The result that the dimensions of the CSD are smaller and less elongated than those of the grains is related to the occurrence of substructures (e.g.: small-angle grain boundaries) that fragment the elongated grain into smaller less elongated CSD. Also the present results of FeAl agree with those of Ti [Zhu03] indicating that in nanocrystalline materials produced by severe plastic deformation it is important to distinguish between CSD and grain sizes.

4.2.3 Applicability of 3D Profile Analysis

The method presented here is different from 3D reconstructions using tomography methods found in the literature [Midgley09, Arslan05]. These methods are based on TEM images showing a contrast that is a monotonic function of some physical property (e.g. mass diffraction contrast as in the case of biological specimens). In these cases the sample is tilted and images are recorded thus allowing to reconstruct isolated or embedded nanostructures. Still these methods can not be applied to nanocrystalline materials as their contrast is dominated by the specific diffraction condition during the tilting series. In contrast the method presented here is based on electron diffraction and allows the reconstruction of the size and shape of the average coherently scattering domain. It should be noted that the evaluation of $\langle D \rangle_V$ is based on the fact that a large number of CSD is present in the illuminated area. The set of CSD that contributes to the broadening of a diffraction peak changes with the tilt position since tilting leads to a change of the diffraction condition. But the information that is obtained only from the set of CSD having a reflecting plane near Bragg condition is sufficient due to the large number of CSD present. Therefore, the method is applicable to all kinds of nanocrystalline materials allowing to determine the average size and morphology of the CSD without the need to prepare multiple sections.

Analysing the CSD sizes statistically directly from the TEM images would not have been an alternative because complex contrast features are frequently observed in TEM images of bulk nanocrystalline materials due to high dislocation densities in the fragmented grains and strong moiré effects of overlapping nanograins or CSD [Rentenberger04]. Therefore, the segmentation of the CSD in the dark-field images can be quite difficult. In contrast grain sizes can only be determined from TEM images. Therefore the possibility of TEM to switch between imaging and diffraction mode allows to acquire information on both the CSD size and the grain size. Electron back scattered diffraction is frequently applied to cross sections of HPT discs to determine the elongation of the grains [Pippan10], however in the case of intermetallic compounds the grain size reached after HPT is too small and the dislocation density too large for the applicability of this method.

5 Thermal Stability of Nanocrystalline FeAl¹

“Tantum elementa queunt permutato ordine solo.”

– *Titus Lucretius Carus*

5.1 DSC and TEM Investigations

To investigate the thermal stability of nanocrystalline FeAl, DSC measurements were conducted. Figure 5.1 shows a DSC curve from a homogeneous nanocrystalline sample. Three peaks are visible corresponding to three exothermic processes. To determine which processes are occurring, TEM investigations were conducted of a deformed sample and samples that were deformed and then heated to 220°C, 370°C and 500°C. These temperatures were chosen as they lie right between the peaks as indicated with an arrow in Figure 5.1.

Figure 5.2 shows a sample deformed by HPT to a shear strain of $\gamma = 63 \pm 7$. The sample is homogeneously nanocrystalline. The bright-field image (cf. Fig. 5.2a) shows very complicated contrasts that are typically observed in nanocrystalline samples. The nanograins contain a high density of dislocations and small-angle grain boundaries resulting in frequent moiré contrasts. In the dark-field image the grains are more clearly visible. The grains are around 80 nm in size and contain many substructures. Figure 5.2b shows a dark-field image of a nanograin that was encircled for a better visibility. The corresponding SAD pattern from a region of 1.2 μm (cf. Fig. 5.2c) shows a ring pattern as the sample is nanocrystalline. No pronounced texture is observable. The diffraction pattern shows clearly that the sample is disordered as the superstructure is absent.

¹ The results included in this chapter were published in the following peer-reviewed papers:

- The DSC and TEM studies in [Mangler10].
- The studies on the reordering of nanocrystalline FeAl in [Gammer11a].

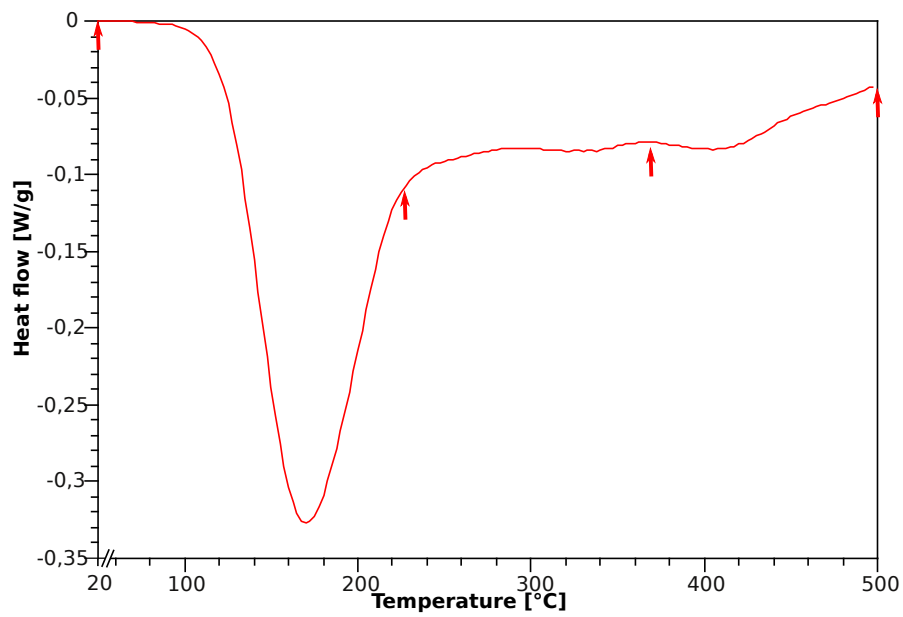


Figure 5.1: Baseline corrected DSC curve of nanocrystalline FeAl obtained by HPT deformation, recorded using a heating rate of 20 K/min. Three exothermic peaks can be observed. To analyse the exothermic processes, TEM investigations were conducted of samples heated to different temperatures (indicated in the image by arrows).

TEM images of a sample deformed to a shear strain of $\gamma = 63 \pm 7$ and subsequently heated to 220°C are shown in Figure 5.3. No significant changes are visible in the bright- and dark-field images as compared to the deformed sample. In the diffraction pattern however it can be noticed that superlattice reflections start to appear. This is even more clearly visible in the diffraction profile shown as an insert in the SAD pattern. Thus it can be concluded that the first exothermic peak in the DSC curve corresponds to the reordering process.

Figure 5.4 shows a sample deformed to a shear strain of $\gamma = 67 \pm 7$ and heated to 370°C . From the bright-field images it can be seen that most of the dislocations have annealed out. The corresponding dark-field image shows this even more clearly as grains with a homogeneous contrast are visible. The nanograins have rather sharp grain boundaries and are free of dislocations. Therefore it can be deduced that the second very broad exothermic peak in the DSC curve corresponds to the annihilation of dislocations. It is very surprising that the grains as deduced from the dark-field image have a size of around 35 nm only, meaning the grain size is reduced upon annealing by a factor of 0.5. The grain size reduction will be analysed in more detail in the next chapter. The diffraction pattern shows that still some ordering occurs between 220°C and 370°C leading to the conclusion that the ordering peak is not symmetric but extended towards higher temperatures.

Figure 5.5 shows a sample deformed to a shear strain of $\gamma = 63 \pm 7$ and heated to 500°C . The bright-field image shows that the grains have already grown considerably. The grains are now completely free of dislocations and have very sharp grain boundaries. In the diffraction pattern no continuous rings are visible but rather distinct spots, as now less orientations are present in the area that was used for taking the SAD pattern. Therefore it can be concluded that the third peak in the DSC-curve corresponds to grain growth.

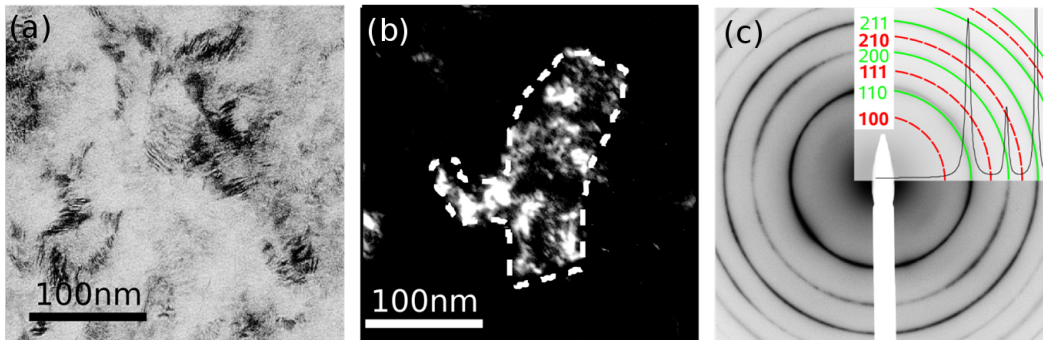


Figure 5.2: (a) Bright-field image of a FeAl sample after HPT deformation. The grains are not clearly defined showing complex contrasts. (b) Corresponding dark-field image. A grain can be seen, it is surrounded by a dashed line for better visibility. The grain contains a lot of defects. (c) The diffraction ring pattern shows no superlattice reflections (indicated by dashed lines) as the sample is disordered.

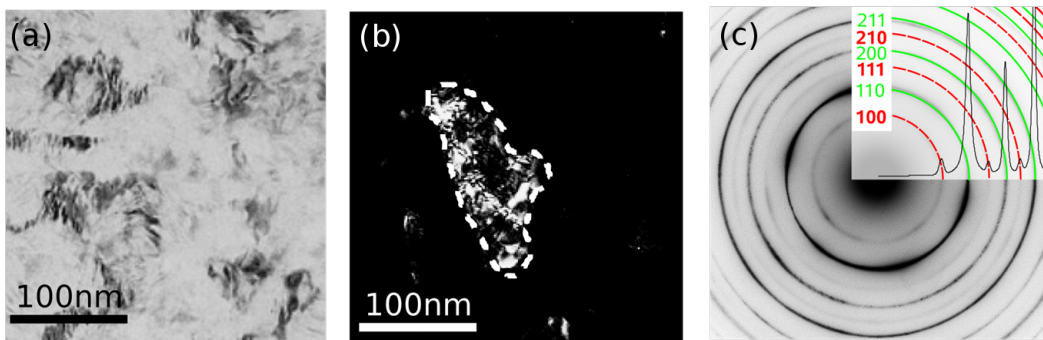


Figure 5.3: (a) Bright-field image of a FeAl sample after HPT deformation and subsequent heating to 220°C. The grains are not clearly defined showing complex contrasts. (b) Corresponding dark-field image. A grain can be seen, it is surrounded by a dashed line for better visibility. The grain contains a lot of defects. The structure looks the same as that of the as-deformed sample. (c) The diffraction ring pattern shows superlattice reflections (indicated by dashed lines) as the sample is partially ordered.

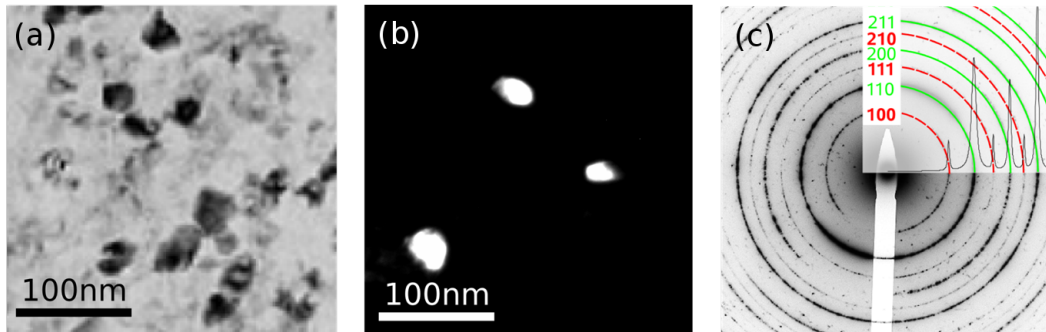


Figure 5.4: (a) Bright-field image of a FeAl sample after HPT deformation and subsequent heating to 370°C. The grains are clearly defined, only few dislocations are visible. (b) Corresponding dark-field image. Three grain are visible showing a homogeneous contrast thus indicating that they are free of dislocations. (c) The diffraction pattern shows a clear presence of superlattice reflections (indicated by dashed lines) as the sample is ordered.

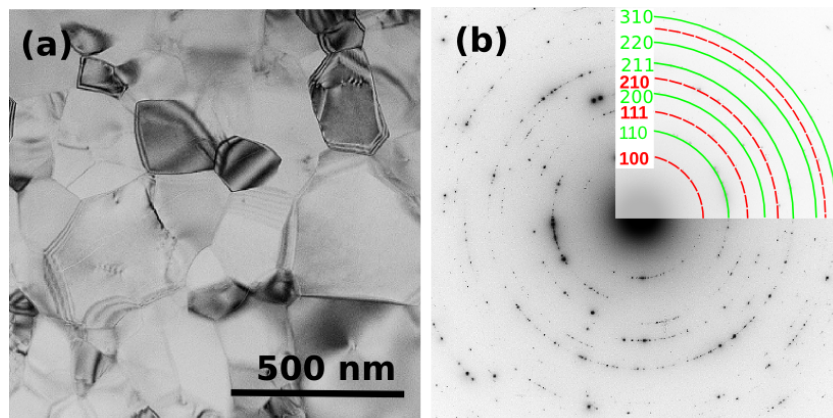


Figure 5.5: (a) Bright-field image of a FeAl sample after HPT deformation and subsequent heating to 500°C. Rather large grains are visible that are free of dislocations and have sharp grain boundaries. (b) The diffraction pattern shows spots rather than rings due to the large grain size. The sample is ordered as can be deduced from the presence of superlattice reflections (indicated by dashed lines).

From the TEM investigations of samples heated to 220°C, 370°C and 500°C it is therefore possible to understand all three exothermic processes occurring during heating of nanocrystalline FeAl, produced by HPT deformation [Mangler09]. Figure 5.6 shows a schematic fit of the three processes to a DSC-curve. The first peak that is caused by reordering is centred around 170°C and asymmetric. An approximate peak shape is indicated in the DSC-curve using a solid line. Its large area can be explained by the high ordering energy of FeAl. The second very broad peak, centred around 320°C that is caused by annihilation of defects is indicated by a dashed line in the DSC curve. The third peak centred around 420°C is due to grain growth. It is indicated in the DSC curve with a dotted line.

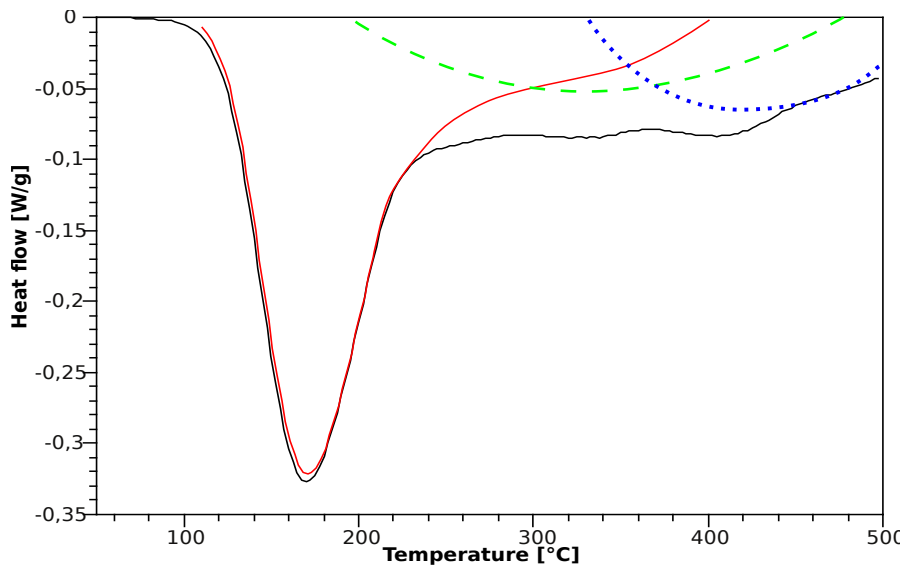


Figure 5.6: Separation of the different processes in the DSC curve of HPT deformed nanocrystalline FeAl. Three exothermic peaks are visible. The first peak, caused by reordering is indicated using a solid line. The second peak, caused by the annealing of dislocations is indicated using a dashed line and the third peak that is due to grain growth is indicated by a dotted line. [Gammer11d]

5.2 Grain Size Evolution During Heating

To study the evolution of the grain size, grain size histograms were determined from dark-field images using the free image-processing software ImageJ. In Figure 5.7 as an example two histograms are shown, the histogram of the sample heated to 220°C

and that of the sample heated to 370°C. The histograms are rather different. While the sample heated to 220°C shows a rather broad range of grain sizes that range up to 200 nm and are most frequently somewhere around 60 nm, the sample heated to 370°C shows a quite narrow histogram with much smaller grain sizes ranging most frequently around 30 nm.

The volume weighted grain sizes of the as-deformed sample and those heated to 170°C, 220°C, 370°C and 500°C were computed from the data. The results are summarized in Figure 5.8. It should be noted that the error bars are asymmetric as by grain size determination from dark-field images grain sizes can easily be underestimated.

5.3 Using Dark Field Series to Determine the Grain Size Reduction

It is very surprising that the grain size decreases upon heating between 220°C and 370°C. To check that the grain size reduction is not an artefact of the dark-field image segmentation it is necessary to use a method that can measure tilt angles with a high precision. Figure 5.9 shows a TEM study of HPT deformed FeAl. As already shown in the previous chapter, the TEM bright-field image (cf. Fig. 5.9a) shows strong contrast variations indicating that the sample is nanocrystalline. The grain boundaries are not well defined and the grains contain a high density of defects. The corresponding SAD (cf. Fig. 5.9c) shows no superlattice reflections (e.g. $\{100\}$) as the sample is disordered. Figure 5.9b shows a TEM dark-field image taken from the same region as Figure 5.9a. The position of the aperture used for the dark-field image is indicated in the SAD pattern (cf. Fig. 5.9c). The contrasts in the dark-field image are very complicated as the defect density is very high.

To determine whether the intensity variations are due to dislocations, grain boundaries or sub-grain boundaries it is necessary to measure small local orientation variations. Standard methods to determine orientation variations are electron backscatter diffraction used in scanning electron microscopes; in TEM SAD patterns, Kichuchi diffraction patterns or small-angle convergent beam electron diffraction are used. In the case of highly deformed nanocrystalline materials it is not always possible to apply these methods successfully. As shown in chapter 3.2, by using dark-field scanning local orientations can be measured even in a highly deformed material.

Consider e.g. the dark-field image in Figure 5.9b. Only crystals that are near

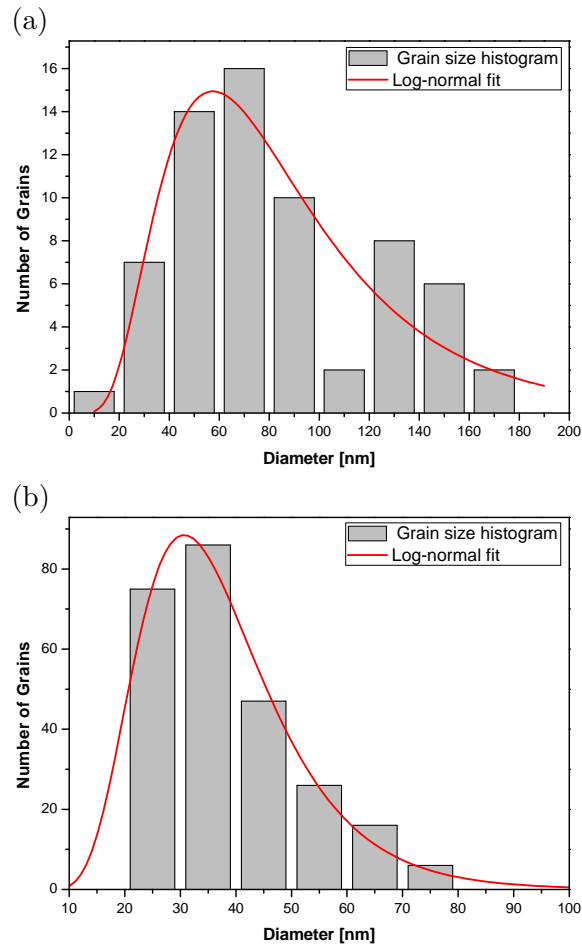


Figure 5.7: (a) Grain size histogram of a HPT deformed FeAl sample after heating to 220°C. (b) Grain size histogram of a HPT deformed FeAl sample after heating to 370°C. A log-normal distribution is fitted to the grain size histograms.

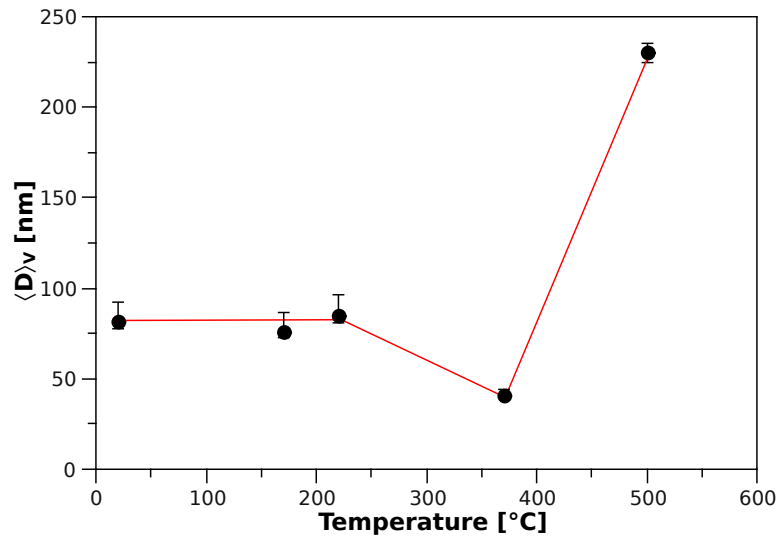


Figure 5.8: Evolution of the volume weighted grain size with heating temperature. No change is visible when heating up to 220°C. By heating to 370°C the grain size is reduced. Heating to 500°C leads to grain growth.

Bragg-position for the given aperture position (cf. Fig. 5.9c) light up. In the present dark-field image the region indicated as d lights up whereas the region indicated as e does not light up. In order to allow a precise reconstruction of the diffraction patterns more than 300 dark-field images were recorded, scanning along the $\{110\}$ and $\{200\}$ diffraction rings (drift correction was performed by recording intermediate bright-field images). For each dark-field image the mean intensity in the selected region was evaluated to find out the corresponding intensity in the diffraction pattern. As the diffraction rings were heavily oversampled, it is possible to deconvolute for the size of the aperture, thus obtaining the position of the diffraction spots with a high precision.

Figure 5.9d represents the reconstructed diffraction pattern corresponding to region d. (The intensities of the diffraction spots are indicated by their size.) The diffraction pattern corresponds to a $[100]$ orientation. Figure 5.9e represents the reconstructed diffraction pattern corresponding to region e again showing a $[100]$ orientation, but is rotated by 8° with respect to region d. Therefore it is concluded that the two regions are separated by a small-angle grain boundary. In a similar way the tilt between other regions was measured revealing again the presence of small-angle grain boundaries (cf. Fig. 5.9b). In addition to the presented grain, further

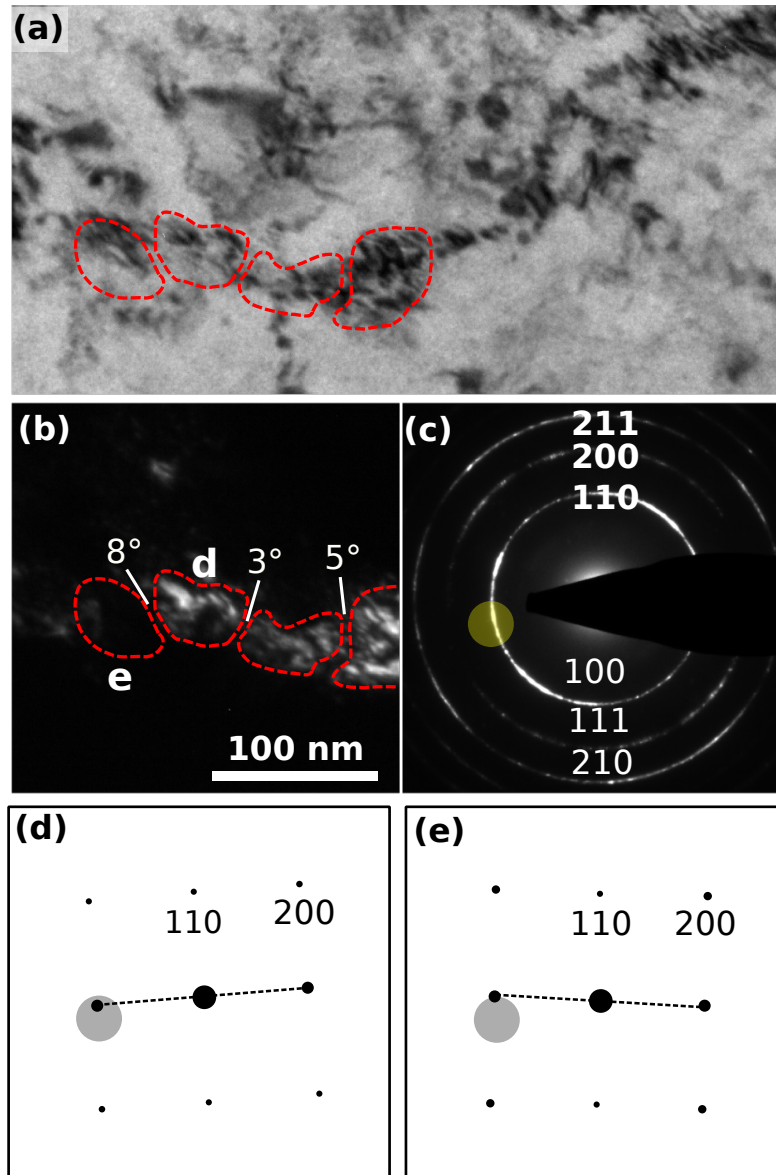


Figure 5.9: Nanocrystalline FeAl processed by HPT. (a) Bright-field image (b) dark-field image and (c) diffraction pattern of the as-deformed sample. (d-e) Reconstructed diffraction patterns of areas d and e encircled in (b) indicate the presence of small-angle grain boundaries.

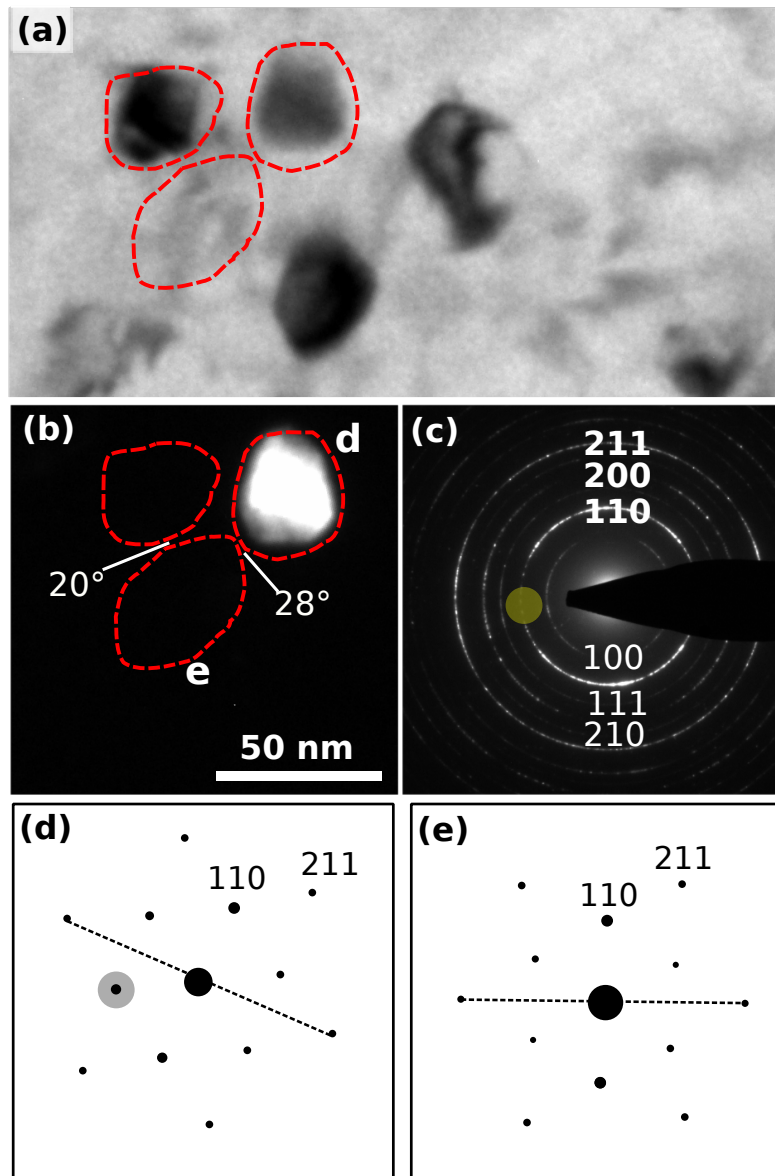


Figure 5.10: Nanocrystalline FeAl processed by HPT and heated up to 370°C. (a) Bright-field image (b) dark-field image and (c) diffraction pattern of the heated sample. (d-e) Reconstructed diffraction patterns of the grains d and e indicated in (b) showing a large-angle grain boundary.

grains were studied showing the presence of small-angle grain boundaries within the grains. It should be pointed out that grains are defined as being separated by large-angle grain boundaries (i.e. grain boundaries $\geq 15^\circ$).

Figure 5.10 shows a TEM study of HPT deformed FeAl heated to 370°C. As already shown in the previous chapter, the TEM bright-field image (cf. Fig. 5.10a) shows that the dislocation density is strongly reduced and most grains show rather sharp grain boundaries. This is also confirmed in the TEM dark-field image (cf. Fig. 5.10b), where an isolated grain showing rather homogeneous contrast lights up. The corresponding SAD pattern (cf. Fig. 5.10c) shows superlattice reflections (e.g. $\{100\}$) indicating that long-range order was restored during annealing of the sample.

To ensure that the region lighting up in the TEM dark-field image (cf. Fig. 5.10b) really represents a grain, it is necessary to show that it is separated by a large-angle grain boundary from the neighbouring regions. Thus the orientation differences have been measured by reconstructing diffraction patterns. More than 450 dark-field images were recorded, scanning along the $\{110\}$, $\{200\}$ and $\{211\}$ diffraction rings. Figures 5.10d and e show the reconstructed diffraction patterns corresponding to the regions indicated as d and e in the the TEM dark-field image (cf. Fig. 5.10b). Both diffraction patterns show a $[111]$ orientation, but they are rotated against each other by 28° , thus clearly being separated by a large-angle grain boundary. An additional large-angle grain boundary is indicated in Figure 5.10b and it should be mentioned that many areas of the sample were studied giving similar results.

5.4 Evolution of the Coherently Scattering Domain Size

In addition to the grain size measured by TEM images it is of interest to study the coherently scattering domain size. X-ray profile analysis (XPA) is widely used for determining the CSD size of nanomaterials [Schafner05]. As shown in chapter 3.1 it is possible to perform profile analysis based on SAD patterns by PASAD. Electron diffraction profiles were deduced from the SAD patterns by azimuthal integration (cf. Fig. 5.11).

The full width half maximum (FWHM) of the diffraction peaks were deduced by fitting pseudo-Voigt functions to all the peaks using the PASAD-tools [Gammer10]. All FWHM values were deconvoluted for the instrumental peak broadening. A

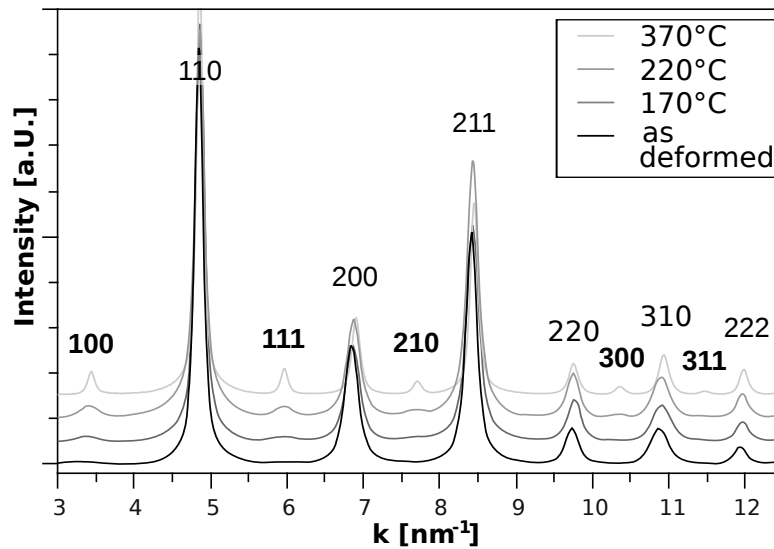


Figure 5.11: Diffraction profiles of HPT deformed FeAl. The profiles were obtained by azimuthal integration of TEM diffraction patterns taken from the as deformed state and from samples heated to 170, 220 and 500°C. The fundamental reflections ($\{110\}$, $\{200\}$, $\{211\}$ and $\{220\}$) are present in all temperatures whereas the intensity of the superlattice reflections (indicated in bold) rises with increasing temperature.

modified Williamson-Hall plot using only the fundamental reflections was used to determine the volume weighted mean CSD size ($\langle D \rangle_V$). To obtain a good statistical analysis at least 10 SAD patterns were analysed for each sample and the mean value and the standard deviation were computed. Figure 5.12 shows the evolution of the coherently scattering domain size with heating. $\langle D \rangle_V$ increases with increasing temperature.

5.5 Growth of Nanosized Ordered Domains

In addition to the fundamental reflections that were used in the previous chapter to determine the evolution of the CSD size with temperature, the rise of superlattice reflections with temperature can be observed in the diffraction profiles (the corresponding indices are indicated in bold in Fig. 5.11). In the profile of the as-deformed sample the superlattice reflections are not observed clearly; only a very broad hump near the position of the $\{100\}$ peak gives some indication of residual order. Heating the sample leads to a clear appearance of the superlattice reflections

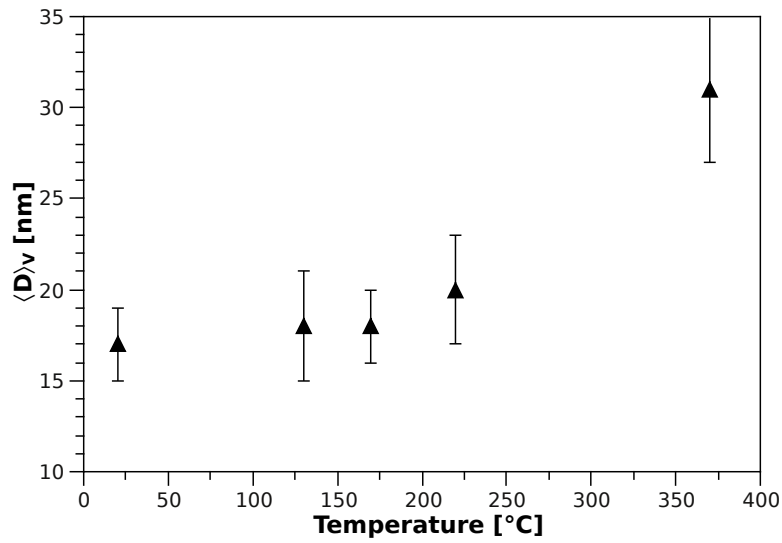


Figure 5.12: Evolution of the volume weighted mean coherently scattering domain size with temperature.

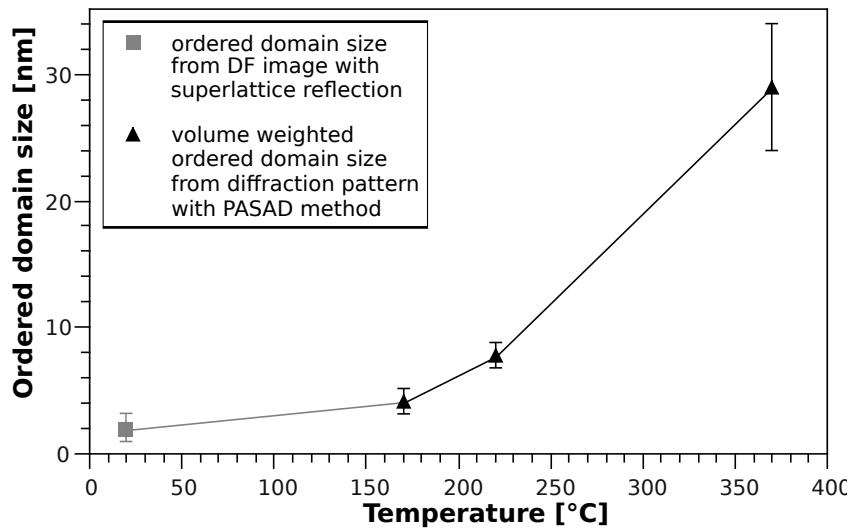


Figure 5.13: Variation of the ordered domain size of FeAl deformed by high pressure torsion and heated to different temperatures. The increase reveals that reordering takes place by the growth of ordered domains until they reach the size of the grains.

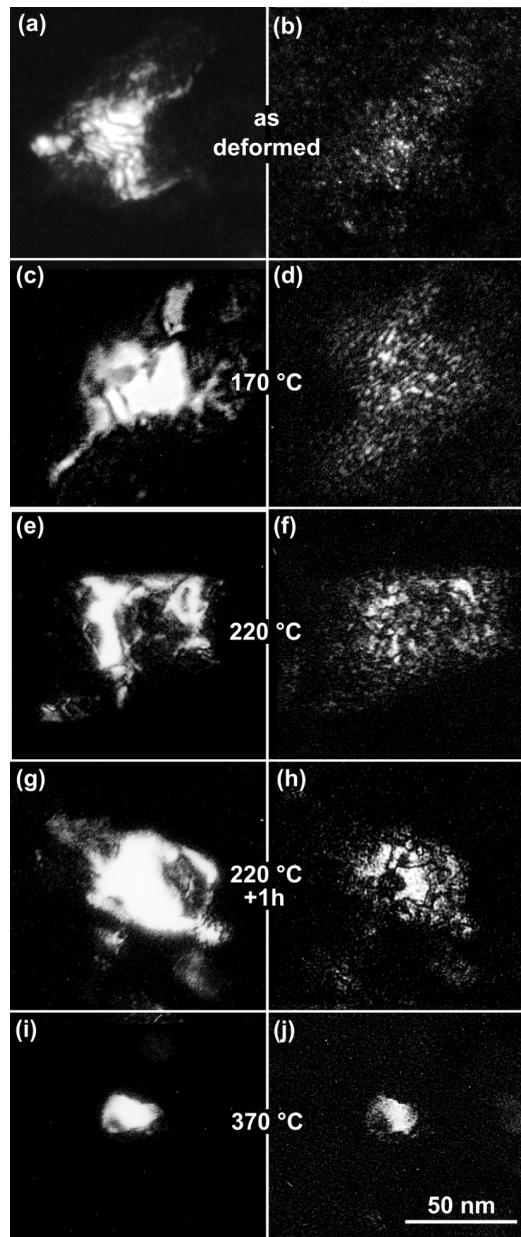


Figure 5.14: TEM dark-field images of nanocrystalline FeAl taken with the $\{200\}$ fundamental reflection (left column) and images of the same grain taken with the corresponding $\{100\}$ superlattice reflection (right column) to reveal the ordered domains. (a, b) show the as-deformed state; (c, d) and (e, f) samples heated to 170 and 220°C, respectively. (g, h) show a sample annealed for one hour at 220°C and (i, j) a sample heated to 370°C. The ordered domains grow with temperature and time until they reach the size of the grains as shown in (i) and (j).

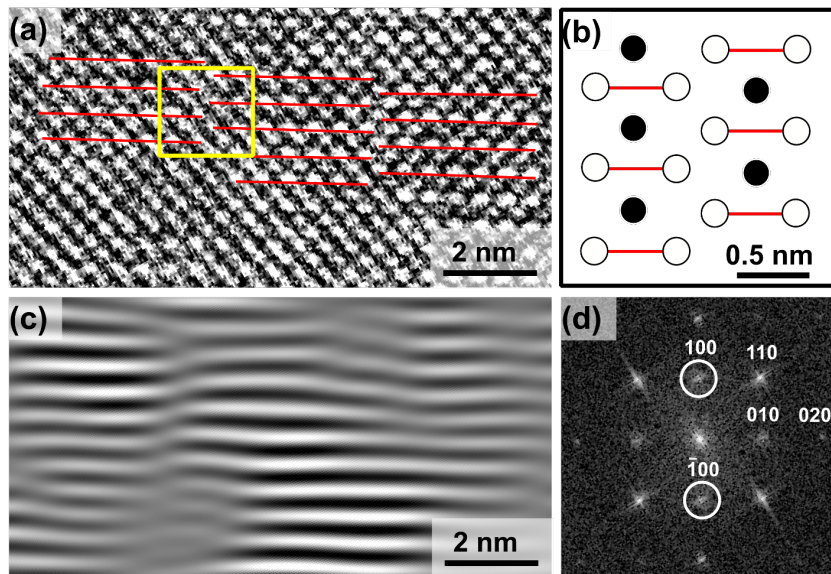


Figure 5.15: FeAl deformed by high pressure torsion and annealed to 170°C. (a) High resolution TEM image revealing the presence of long-range ordered domains ($\{100\}$ lattice planes are marked by lines). (b) Sketch of the atomic structure of the region indicated by a square in (a) showing an APB fault. (c) Fourier filtered image of (a) to make the ordered domains clearly visible. This image is formed using two $\{100\}$ superlattice reflections indicated in the diffractogram (d).

(e.g. the $\{100\}$, $\{111\}$ reflection) in the diffraction profiles giving evidence of the restoration of the B2 superstructure. With increasing temperature the intensity of the superlattice reflections rises according to an increase in long-range order. From the width of the superlattice reflection, it can be concluded that the chemically ordered domains are still very small at 170°C and grow during further heating as indicated by the sharpening of superlattice reflections.

For a quantitative analysis of the size of the chemically ordered domains again a modified Williamson-Hall plot [Williamson53, Ungar96] was used, but this time taking into account the superlattice reflections only. The volume weighted mean ordered domain size ($\langle D \rangle_{ord}$) was determined from the FWHM of the $\{100\}$, $\{111\}$ and $\{210\}$ superlattice diffraction peaks of the diffraction profile. At least 10 SAD patterns were analysed for each sample and the mean value and the standard deviation were computed. All values were deconvoluted for the instrumental peak broadening. It should be pointed out that a direct comparison of the present profiles with X-ray profiles measured on the same samples reveals that the strong interaction of electrons with matter compared to X-rays facilitates the detection of superlattice peaks especially at the early stages of reordering. In the case of the as-deformed sample the superlattice reflections are not clearly observable as they are very broad and weak due to the small ordered domain size; therefore the value of $\langle D \rangle_{ord}$ had to be estimated from dark-field images of the ordered domains. The increase of the ordered domain size with temperature is plotted in Figure 5.13: At 170°C, the ordered domains are 4.1 ± 1 nm, growing to 7.8 ± 1 nm at 220°C and to 29 ± 5 nm at 370°C. These results show that reordering is linked to the growth of ordered domains. The process of domain coarsening proceeds until the order is fully restored within the grains.

In addition the evolution of the nanosized ordered domains was monitored in dark-field images of samples heated up to different temperatures. For each structural state dark-field images were taken using the $\{200\}$ fundamental reflection and the corresponding $\{100\}$ superlattice reflection (cf. Fig. 5.14). The contrast features appearing in the superlattice reflection are sensitive to both structural defects and the chemical long-range order whereas contrasts visible in the fundamental reflection depend on structural defects only. Since in B2 alloys the APB faults are pure chemical faults as indicated by pair potential calculations [Yamaguchi81] it can be concluded that the contrasts appearing in the image formed by superlattice reflection but not in that formed by the fundamental reflection are caused

by APB faults. Figures 5.14a and b show dark-field images of the as-deformed sample. Figure 5.14a obtained by using a fundamental reflection shows contrast variations within one grain indicating some fragmentation of the grain due to subgrains. Figure 5.14b shows a dark-field image taken with the $\{100\}$ superlattice reflection. Although only a weak hump is observed in the intensity profile deduced from the diffraction ring pattern, the dark-field image reveals clearly the presence of very small chemically ordered domains of medium range size (~ 2 nm) in the as-deformed state.

Due to their small size and their very weak and broad peak in the diffraction pattern, this state is different from that of a sample with residual long-range order. The residual order can not be explained by a statistically partially ordered structure, but rather by a structure composed of chemically ordered nanodomains of medium range size. These nanodomains are densely distributed within the grain and quite homogeneous in size. Therefore, it can be concluded that severe plastic deformation of FeAl, an intermetallic compound with a high ordering energy, does not destroy the long-range order completely but leads to a high density of APB and thus to the formation of chemically ordered nanodomains. This result is consistent with that of the deformation-induced process of fragmentation of ordered domains in Cu_3Au as observed by TEM dark-field images [Rentenberger08].

Heating the sample to 170°C shows significant differences in the dark-field image taken using the superlattice reflection indicating that the ordered domains have grown (cf. Fig. 5.14d). In the sample heated to 220°C further coarsening of ordered domains is observed (cf. Fig. 5.14f). This result agrees well with that obtained from the diffraction data. When annealing the sample for one hour at 220°C the ordered domains grow even further (cf. Fig. 5.14h) indicating the time dependent mean domain size at constant temperature. Therefore, for the determination of the temperature dependent domain size a well defined heating procedure (e.g. as it is used in a DSC) is essential. It should be noted that even the comparison of samples stored for different times at room temperature show that storage times of several months change the domain structure. Heating the sample up to 370°C , the dark-field images taken using the superlattice and the fundamental reflection show similar contrasts of the same region, indicating that the ordered domain size has reached the grain size (cf. Fig. 5.14i+j). Again a reduction of the grain size when heating to 370°C is observed. It should be emphasised that the quantitative results for the ordered domain size resulting from PASAD agree very well with the size

deduced from the dark-field images using superlattice reflections. Therefore, the results deduced from both, diffraction patterns and dark-field images provide clear evidence that the reordering process occurs by coarsening of chemically ordered domains by reducing APB faults.

The small nanosized ordered domains present in the sample heated up to 170°C were studied in more detail using high resolution TEM. In Figure 5.15a the superlattice is visible (marked by lines along $\{100\}$ lattice planes). The $\{100\}$ lattice planes are interrupted by APB faults; the atomic structure at one APB fault (indicated by a square in Figure 5.15a) is drawn in detail in Figure 5.15b. The presence of chemical long-range order is evident from the power spectrum of the high resolution TEM image, showing $\{100\}$ superlattice reflections (cf. Fig. 5.15d). To enhance the visibility of the ordered domains, a Fourier filtered image using only two (100) superlattice reflections (marked in Figure 5.15d) is presented in Figure 5.15c. Therefore, the results show that chemically ordered domains are separated by sharp APB faults. This result is in good accordance with that of dark-field images (cf. Fig. 5.14d) showing densely and homogeneously distributed nanosized ordered domains of similar size deduced from electron diffraction results.

The results of the present study can be compared with the results of DSC measurements (cf. Fig. 5.1) revealing that the heating induced growth of the ordered domains starts at temperatures of about 130°C and continues up to 370°C. For comparison in-situ neutron diffraction experiments of mechanically milled Fe-30at%Al indicate that the growth of the ordered domains starts at considerably larger temperatures of 340°C [Apinaniz03]. Furthermore, it should be pointed out that the process of reordering by growth of the chemically ordered domains as encountered in the present study is different to the change of the long-range order parameter that takes place in other B2 structured alloys that have an order-disorder transition below the melting temperature (e.g. CuZn [Shewmon69]).

It should be pointed out that in the present case it is safe to assume that the structure of the ordered nanodomains in the as-deformed samples is hardly influenced by the temperature rise caused by the HPT deformation. Based on the experimental conditions and the experimental findings it is concluded that this temperature rise is less than 30 K. The reasons are as follows: (i) The speed of the HPT deformation is low (5 min/revolution). (ii) The surface temperature of the anvils of the HPT sample stays at room temperature. Assuming that the total deformation energy turns into heat, the calculated temperature rise of the sample is well below

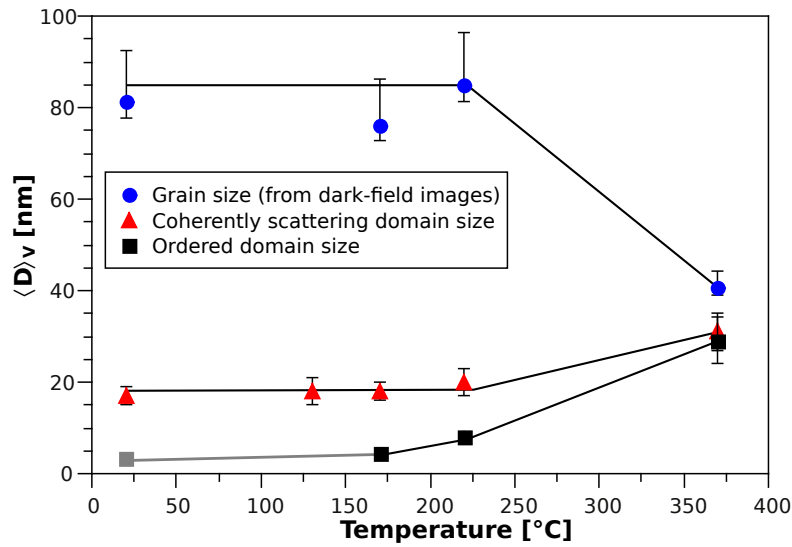


Figure 5.16: Evolution of the ordered domain size, the coherently scattering domain size and the grain size with temperature.

30 K at the present conditions. (iii) The fact that the domain structure of the as-deformed sample is affected when they are stored at room temperature (several months) indicates that the samples have not been exposed to a temperature much above room temperature. (iv) In the samples deformed by HPT in the same way, the change in the deformation-induced ferromagnetism indicates structural changes when heated up to 50°C [Mangler11]. However, when different conditions for the HPT deformation are used, it is possible, that considerable heating of the samples can occur as it was reported [Edalati09].

5.6 Grain Size Reduction by Heating

The complete TEM analysis leads to the following picture of recrystallization in HPT deformed FeAl. Figure 5.16 shows the evolution of the ordered domain size, the CSD size and the grain size with temperature. From these results a schematic model of the different processes occurring in the course of grain size reduction was developed. Figure 5.17a shows the situation prior to heating: One grain (large-angle grain boundaries are indicated by thick black lines) is separated into two subgrains by a small-angle grain boundary (indicated by the dashed line). The small-angle grain boundary is formed by dislocations. The subgrains are divided

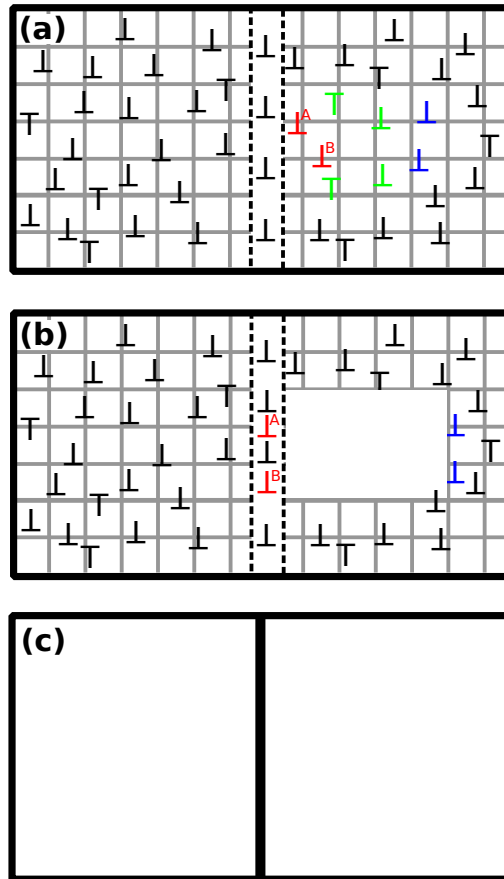


Figure 5.17: Schematic model of the different processes occurring in the course of grain size reduction. (a) Prior to heating a grain (thick black lines) is separated into two subgrains by a small-angle grain boundary (indicated by the dashed line). The subgrains are divided into small ordered domains (grey lines). (b) Upon heating a coarsening of the ordered domains occurs. The growth of only one ordered domain is shown schematically. Some dislocations annihilate (indicated green), but others (indicated in blue and red) are moved by the APB into the grain and subgrain boundaries. The dislocations indicated with a superscript are incorporated into the subgrain boundary thus increasing the dislocation density at the subgrain boundary and increasing the tilt angle thus transforming it eventually into a large-angle grain boundary (c).

into small ordered domains by APB (grey lines) and contain a large density of dislocations that interact with the APB. Heating leads to a drastic growth of the ordered domains, but the grain and subgrain size stays about constant. This means that the temperature is well below the temperature at which grain growth starts. As the dislocations strongly interact with the APB, movement of the APB and dislocations are coupled. Figure 5.17b shows schematically the growth of one ordered domain. Some dislocations annihilate (indicated green), but others (indicated in blue and red) are moved by the APB into the grain and subgrain boundaries. The dislocations indicated with a superscript are incorporated into the subgrain boundary thus increasing the dislocation density at the subgrain boundary and increasing the tilt angle. This process does not just occur for one ordered domain but across the entire grain. By this process, once there are enough dislocations in the subgrain boundary, the subgrain boundaries can transform into large-angle grain boundaries (cf. Fig. 5.17c). Due to this mechanism it is possible that starting from large grains containing a high dislocation density, APB and sub-grain boundaries, recrystallization leads to smaller, fully ordered grains that are almost free of dislocations.

Annealing metals usually leads to the rearrangement of dislocations and to the annihilation of dislocation of opposite sign, further annealing leads to grain growth. The situation presented here is different. Dislocations do not only move through a thermal activation, but their movement is coupled very strongly to the movement of the APB. As FeAl shows a strong tendency to reorder, this leads to the movement of dislocations already at very low temperatures, far below the temperature where grain growth starts to occur. As the energy of the APB acts as strong driving force for the rearrangement of dislocations dislocations of the same sign move into the subgrain boundaries and low energy dislocation structures are formed. Thus it can be concluded that grain size reduction by thermal annealing is possible for SPD deformed intermetallics with a high ordering energy if a heating treatment below the temperature of grain growth is applied.

6 Modelling the Reordering

“Give me four parameters and I can fit an elephant, give me five and I can make him wiggle his trunk.”

– John von Neumann

6.1 Kinetics of the Vacancy Diffusion

The reordering of a solid takes place by diffusion, i.e. by the change of lattice places of atoms or vacancies. The simplest diffusion process is the interchange between a vacancy and an atom. Figure 6.1 shows the evolution of the energy during the jump of an atom into a vacancy. At the lattice positions the atom has its energy minimum, while during the jump it has to cross an energy barrier. Atoms in a solid constantly oscillate around their equilibrium position. The mean frequency of atomic vibration is called attempt frequency ν_0 and can be approximated well by the Debye frequency ($\approx 10^{13} \text{ s}^{-1}$). The atom can pass the energy barrier ΔE only if its energy is large enough. The Boltzmann factor determines the probability for the atom to have an energy E at the temperature T

$$P(T,E) = \exp\left(-\frac{E}{k_B \cdot T}\right), \quad (6.1)$$

where k_B denotes the Boltzmann constant. Successful jumps of atoms can be determined by multiplying the attempt frequency and the probability for the atom to overcome the barrier, leading to the following jump frequency

$$\nu = \nu_0 \cdot \exp\left(-\frac{\Delta E}{k_B \cdot T}\right). \quad (6.2)$$

The process of diffusion is usually described as the movement of vacancies through the solid and the energy barrier is called vacancy migration enthalpy H_V^M . Other

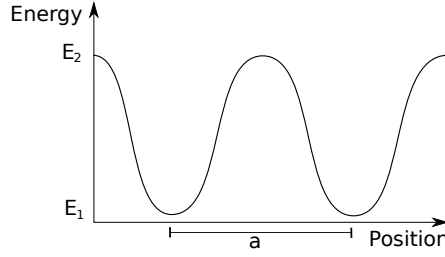


Figure 6.1: Schematic representation of the change of lattice place of an atom with a vacancy. At the lattice position the atom is in an energy minimum. During the jump the atom has to overcome an energetically unfavourable position until returning again to a lattice position.

diffusion processes like the the direct exchange of two neighbouring atoms are very unlikely in solids.

6.2 Reordering via Ordering Jumps

In a statistically disordered material, disorder means that some Fe-atoms occupy Al-lattice position and vice versa (cf. chapter 1.1.2). As the atoms cannot change place with their neighbours, a vacancy is used to order the material by moving the atoms onto the correct sublattice. To reorder the material the vacancy has to meet an atom that is sitting on the wrong lattice position. The fraction of atoms on the wrong sublattice can be related to the order parameter using the relation (cf. chapter 1.1.2)

$$p_{\alpha,\beta} = 1 - p_{\alpha,\alpha} = \frac{1}{2}(1 - S). \quad (6.3)$$

The jump frequency of a vacancy ν was derived in the previous chapter. For FeAl it has to be taken into account that the energy barrier for a vacancy jump depends on the local environment of the vacancy which depends on the order parameter. Using the mean field-theory after Girifalco [Girifalco64] the vacancy migration enthalpy can be expressed in terms of the order parameter S

$$H_V^M = H_{V,S=0}^M + a \cdot S^2. \quad (6.4)$$

In total the rate of ordering jumps $\frac{dS}{dt}$ (neglecting the factor $\frac{1}{2}$) results in

$$\frac{dS(t)}{dt} = (1 - S(t)) \cdot c_V \cdot \nu_0 \cdot \exp\left(-\frac{H_{V,S=0}^M + a \cdot S(t)^2}{k_B \cdot T(t)}\right), \quad (6.5)$$

where c_V denotes the vacancy concentration. It should be noted that this equation takes into account only jumps that lead to a reordering of the material. Furthermore jumps back to the wrong sublattice are ignored as they are energetically more unfavourable.

The model was used by Reimann [Reimann02] to simulate the reordering in nanocrystalline FeAl produced by ball-milling. The simulated long-range order parameter S was fitted to values of S determined by XRD measurements. This approach is very complicated, as it requires precise XRD measurements of many samples annealed at different temperatures. In the diploma thesis [Gammer11d] this model was adapted to describe the heat flow of the DSC. Due to the experimental results obtained by TEM (cf. chapter 5.5) a new reordering model is derived that is based on the coarsening of ordered domains.

6.3 Reordering via the Coarsening of Ordered Domains

6.3.1 Derivation of the Model

As shown in chapter 5.5, HPT deformed FeAl is not statistically disordered but rather contains very small ordered domains (~ 2 nm). The reordering does not occur by atoms changing to the correct sublattice, but through the coarsening of the ordered domains. As shown in Figure 6.2, a vacancy can shift the APB by diffusion. Two APB can meet and annihilate or an APB can be pushed into a grain boundary, leading to the coarsening of the ordered domains (cf. the TEM images in Fig. 5.14 and the schematic drawing in Fig. 6.3).

The system can be described by the APB density ρ_{APB} , but for simulation it is easier to use the fraction of atoms in APB f_{APB} , a parameter without a unit. To convert the APB density measured in m^{-2} to the fraction of atoms in APB it is necessary to calculate the average spacing of the atoms in FeAl. The unit cell of FeAl contains 2 atoms and therefore the average spacing can be calculated from the lattice parameter $d_0/\sqrt[3]{2} = 2.28 \cdot 10^{-10}$ m leading to

$$f_{APB} = 2.28 \cdot 10^{-10} \rho_{APB}. \quad (6.6)$$

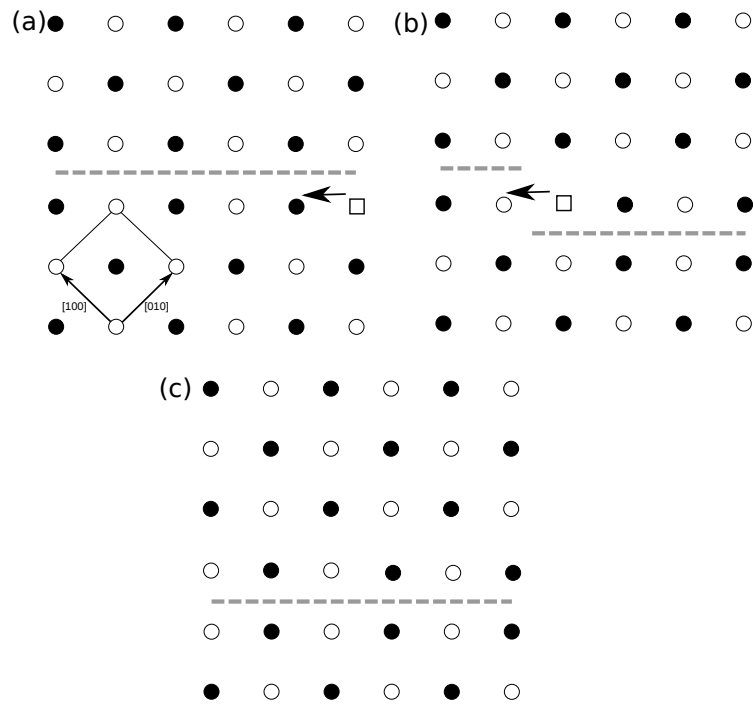


Figure 6.2: Schematic representation of the shift of an APB by vacancy diffusion. (a) shows an APB. (b) A vacancy moves along the APB shifting the atoms and thus moves the APB. (c) The position of the APB is shifted by one atomic plane. [Gammer11d]

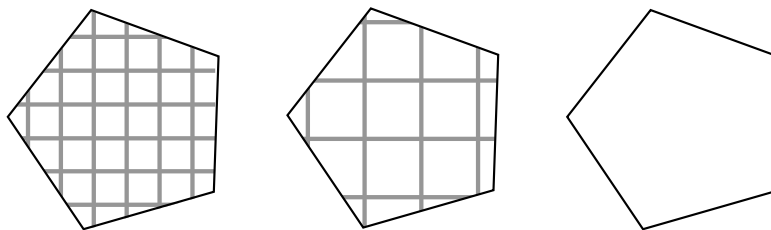


Figure 6.3: Schematic representation of the coarsening of the ordered domains. The grain is cut into small ordered domains by APB (gray lines). With increasing temperature the APB annihilate leading to a growth of the ordered domains until all APB have been annihilated.

The movement of the APB can be best described by a random walk. Assuming the APB have a distance of D atoms, then it takes D^2 jumps for two atoms in APB to meet and to annihilate. The average spacing of two APB is $D = f_{APB}^{-1}$ atoms. For the simulation it is easier to use the fraction of atoms not in APB ($f_S = 1 - f_{APB}$) as parameter. Therefore on average

$$\frac{\text{jumps}}{\text{ordering jump}} = \frac{1}{2}(1 - f_S)^{-2}. \quad (6.7)$$

In equation 6.2 the jump frequency was derived as

$$\frac{\text{jumps}}{\text{time}} = c_V \cdot \nu_0 \cdot \exp\left(-\frac{H_V^M}{k_B \cdot T}\right). \quad (6.8)$$

Combining the expressions we get

$$\frac{df_S(t)}{dt} = \frac{\text{ordering jumps}}{\text{time}} = 2(1 - f_S(t))^2 \cdot c_V \cdot \nu_0 \cdot \exp\left(-\frac{H_V^M}{k_B \cdot T(t)}\right) \quad (6.9)$$

The fraction of APB will not be 100% after deformation. Instead there is a value f_S^0 representing the fraction of atoms not in APB after deformation. This value acts as boundary condition to the differential equation

$$f_S(0) = f_S^0. \quad (6.10)$$

Furthermore it is expected that the vacancy concentration after deformation is much higher than the equilibrium concentration. Therefore a dynamic vacancy concentration $c_V(f_S(t))$ is used. The initial vacancy concentration c_V^0 is taken as free parameter, while for the equilibrium vacancy concentration a value of $c_V^{eq} = 3 \cdot 10^{-6}$ is used. Assuming a linear decrease with f_S and taking into account the starting value of f_S leads to

$$c_V(f_S) = c_V^0 + \frac{f_S - f_S^0}{1 - f_S^0} \cdot (c_V^{eq} - c_V^0). \quad (6.11)$$

To convert $\frac{df_S(t)}{dt}$ to a heat flow $W(t)$ it is necessary to calculate how many joules are in a gram of FeAl that is completely filled with APB. As can be seen from the density, one gram of FeAl corresponds to $(5.80 \cdot 10^6)^{-1} \text{m}^3$, which can be converted to an area of $(5.80 \cdot 10^6 \cdot 2.28 \cdot 10^{-10})^{-1} \text{m}^2$. Multiplying with an APB energy of

$\gamma = 0.3 \text{ Jm}^{-2}$ [Westbrook00a] yields a value of $c = 226 \text{ J/g}$. Furthermore the following correspondence can be derived

$$W(t) = c \cdot \frac{df_S(t)}{dt}. \quad (6.12)$$

The average radius of the ordered domains can be derived by assuming spherical ordered domains. The fraction of surface to volume yields $\frac{6}{d}$, or rather $\frac{3}{d}$ as one surface of a sphere always counts for two ordered domains. Converting the fraction of atoms into a length measure we yield

$$d_{ord} = 3 \frac{2.28 \cdot 10^{-10}}{f_{APB}} \text{m}. \quad (6.13)$$

For the most general case any temperature program $T(t)$ can be used in the differential equation (cf. equation 6.9), but in the following only two special cases will be regarded. Firstly a isothermal annealing at a temperature T_0 . In this case the model reads

$$\frac{df_S(t)}{dt} = 2(1 - f_S(t))^2 \cdot c_V(f_S(t)) \cdot \nu_0 \cdot \exp\left(\frac{-H_V^M}{k_B \cdot T_0}\right) \quad (6.14)$$

and in the case of isochronal heating with a heating rate $T(t) = h \cdot t$

$$h \cdot \frac{df_S(T)}{dT} = 2(1 - f_S(T))^2 \cdot c_V(f_S(T)) \cdot \nu_0 \cdot \exp\left(\frac{-H_V^M}{k_B \cdot T}\right). \quad (6.15)$$

6.3.2 Parameters

In the following we will fit the model to a isochronal DSC-curve. Summarizing the model we get

$$\begin{aligned} h \cdot \frac{df_S(T)}{dT} &= 2(1 - f_S(T))^2 \cdot c_V(f_S(T)) \cdot \nu_0 \cdot \exp\left(\frac{-H_V^M}{k_B \cdot T}\right) \\ W(T) &= c \cdot h \cdot \frac{df_S(T)}{dT} \\ f_S(0) &= f_S^0 \end{aligned} \quad (6.16)$$

The differential equation was solved using the software MAPLE™. A summary of variables and fit parameters used in the model is given in the following table:

variables	
W	heat flow
$f_S = (1 - f_{APB})$	fraction of atoms not in APB
T	temperature
constants	
$k_B = 8.6 \cdot 10^{-5} \text{ eV}$	Boltzmann constant
$\nu_0 = 10^{13} \text{ s}^{-1}$	attempt frequency
$c = 226 \text{ J/g}$	specific energy of FeAl completely filled with APB
$h = 20 \text{ K/min}$	heating rate (can be changed)
$c_v^{eq} = 3 \cdot 10^{-6}$	equilibrium vacancy concentration
fit parameters	
H_V^M	vacancy migration enthalpy
c_V^0	vacancy concentration after deformation
f_S^0	fraction of atoms not in APB after deformation

6.3.3 Influence of Parameter Changes

In the following the influence of a parameter change on the model will be discussed. There are three fit parameters: H_V^M , c_V^0 and f_S^0 . Two fit parameters will be kept fixed while the third is varied. The simulated heat flow, ordered domain size and APB density will be compared for the different parameter values.

Figure 6.4a shows the influence of the change of the vacancy migration enthalpy H_V^M on the simulated heat flow. This parameter has a very strong effect on the peak temperature. Furthermore the width of the peak increases with increasing H_V^M . This behaviour is reasonable, an increase in the energy barrier for the vacancy jump means that a higher temperature is needed for vacancy diffusion to take place. The evolution of the ordered domain size and the APB density also reflects the shift to higher temperatures (cf. Fig. 6.4b+c).

The influence of the vacancy concentration c_V^0 on the simulated heat flow is shown in Figure 6.5a. Again a change of the parameter has an influence on the peak temperature; increasing the vacancy concentration leads to a decrease of the peak temperature. But in the case of the vacancy concentration the effect on the peak width is much stronger than in the case of the vacancy migration enthalpy leading to a strongly increased peak width with decreasing vacancy concentration. The reason is that decreasing the vacancy concentration slows down the reordering process because there are less vacancies to move the APB. The simulated APB

density and ordered domain size reflects this result (cf. Fig. 6.5b+c).

The initial fraction of atoms not in APB, i.e. the initial ordered domain size, is changed in Figure 6.6. The simulated heat flow is shown in Figure 6.6a. Increasing the initial ordered domain size leads to a decrease in the area of the peaks. This can be explained as the area under the curve represents the energy of the total amount of APB in the material. Some shift of the peak position and an increase of the peak width can also be observed, but not in such a strong manner as in the case of the previous parameters. Figure 6.5b+c shows that the initial ordered domain size and initial APB density is changed but the curves approach at higher temperatures.

It is interesting to note that the variation of all the parameters has only little effect on the asymmetry of the heat flow peak. In all cases the fraction of the area before the maximum is $38.5 \pm 0.4\%$. The problem contains three parameters and the heat flow shows three very distinct features (the position of the maximum, the peak width and the area of the peak), therefore fitting the model to a DSC curve works well. The initial fraction of APB can be estimated very precisely from the fit, because a small change has a strong effect on the area and thus height of the peak. An estimation yields an error of about 5% when fitting to a DSC curve (assuming an error in the DSC curve of 0.1 mW and a sample mass of 10 mg). As the vacancy concentration and the vacancy migration enthalpy act differently on the width and position of the peak in the heat flow, it is possible to fit them simultaneously. A change in the vacancy migration enthalpy has a big effect and thus it can be concluded that H_V^M can be determined with a very high precision (about 2% error). Changing the vacancy density has less effect and thus the precision is lower (about 10% error).

6.4 Fitting the Model to a DSC Curve

The fit parameters (H_V^M , c_V^0 , f_S^0) were varied until the simulated heat flow gave the best correspondence to an experimental DSC curve of HPT deformed nanocrystalline FeAl. As shown in chapter 5.1, there are three distinct processes giving rise to the exothermic signal in the DSC curve (cf. Fig. 5.6). For the fit the first peak was used, as it can be attributed to the reordering process. Figure 6.7 shows the best fit. The following values were determined for the fit parameters (the errors are estimated from the parameter dependence):

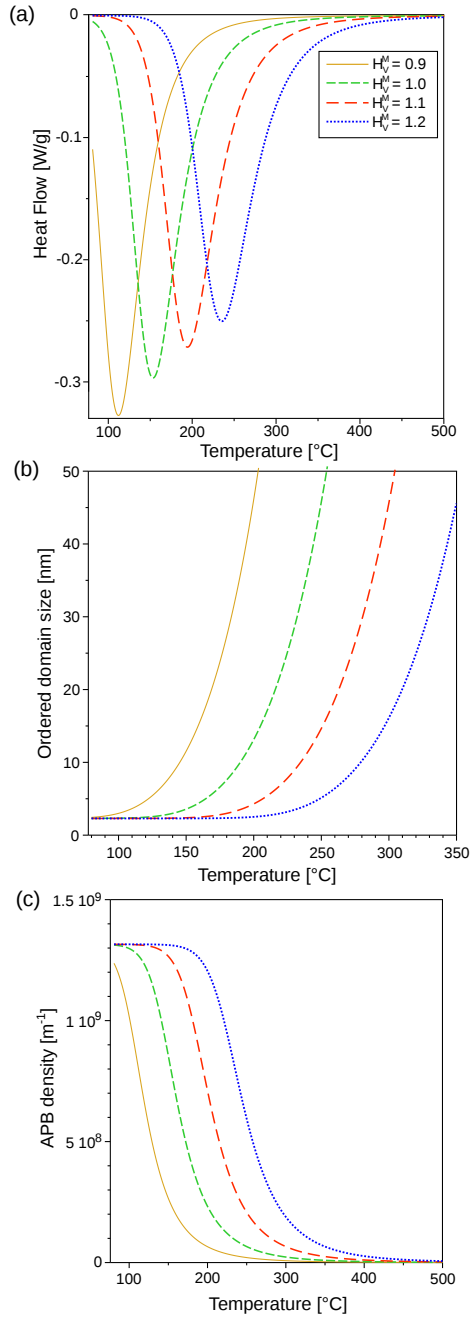


Figure 6.4: (a) Dependence of the simulated heat flow on the vacancy migration enthalpy H_V^M . (b) Simulated ordered domain size and (c) APB density in dependence on H_V^M . An increase in H_V^M leads to a shift of the reordering to higher temperatures. The remaining parameters were kept fixed during the simulations ($c_V^0=10^{-2}$, $f_S^0=0.67$).

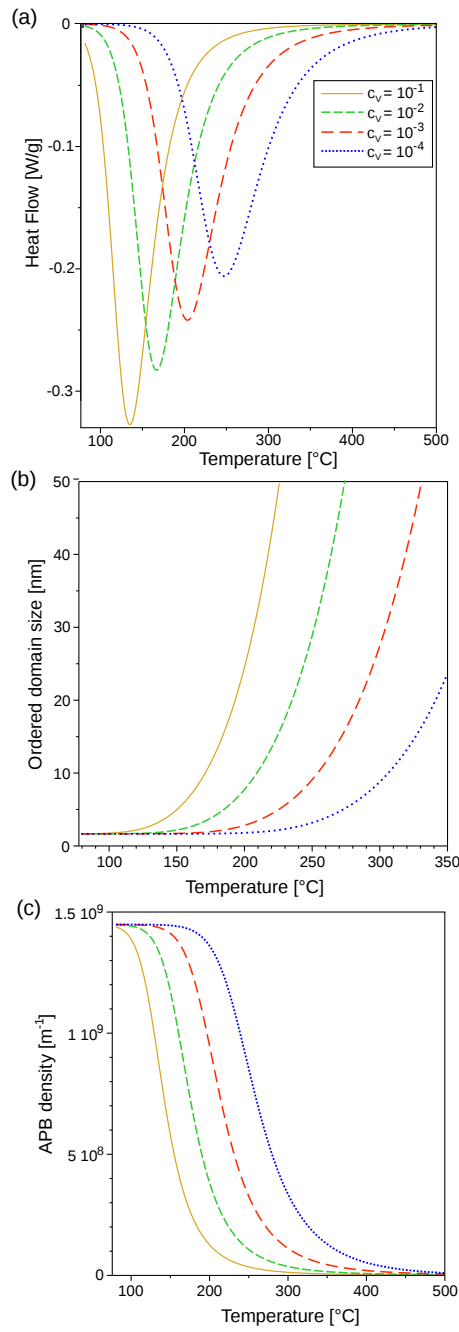


Figure 6.5: Dependence of (a) the simulated heat flow, (b) the ordered domain size and (c) the APB density in dependence on the vacancy concentration after deformation c_V^0 . An increase in c_V^0 leads to a shift of the reordering to lower temperatures and to a strongly reduced peak width. The remaining parameters were kept fixed during the simulations ($H_V^M=1.04$ eV, $f_S^0=0.67$).

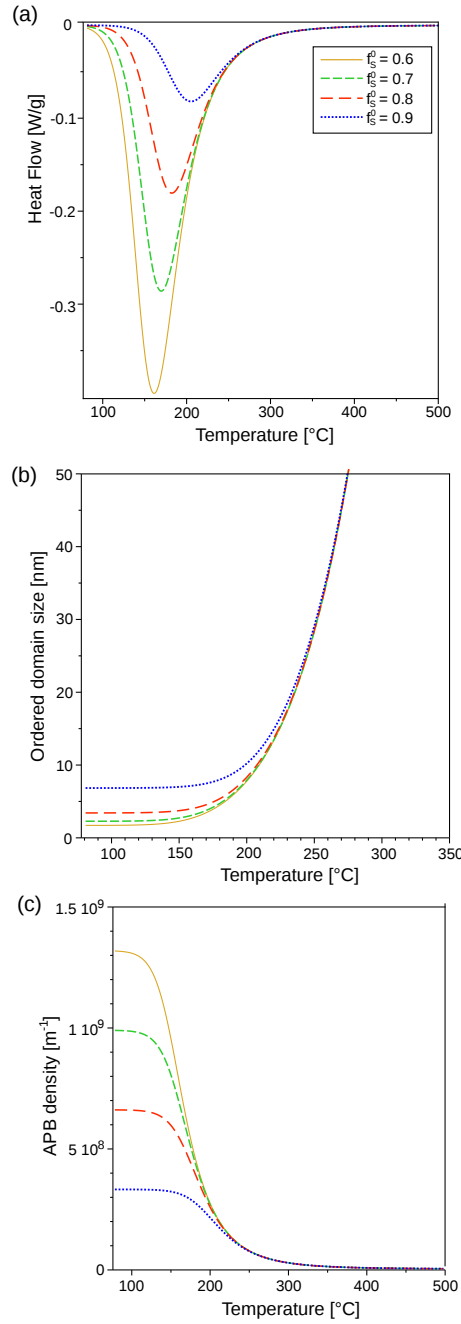


Figure 6.6: (a) Simulated heat flow, (b) ordered domain size and (c) APB density in dependence on the initial fraction of atoms that are not in APB f_S^0 . Changing f_S^0 changes the initial APB density and initial ordered domain size. In the simulated heat flow the area under the peak decreases with increasing f_S^0 . The remaining parameters were kept fixed during the simulations ($H_V^M=1.04$ eV, $c_V^0=10^{-2}$).

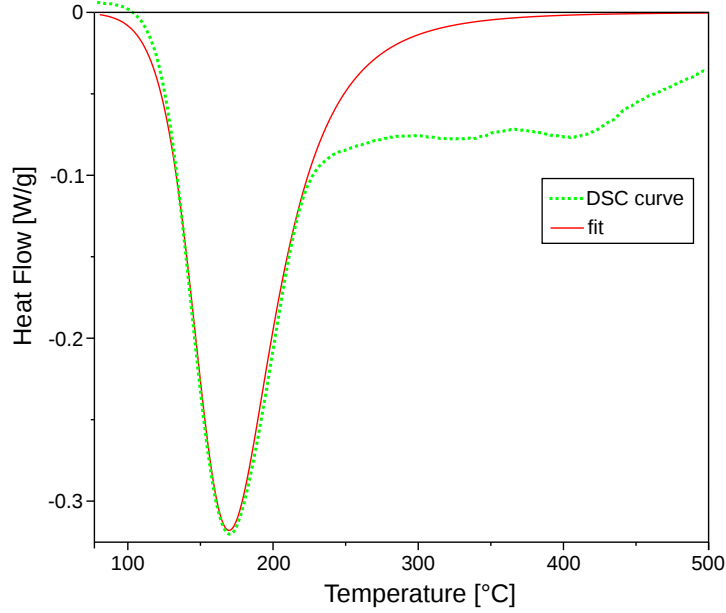


Figure 6.7: Fit of the reordering model to an experimental DSC curve of HPT deformed FeAl. Only the first peak was taken into account for the fit because it represents the heat flow caused by the reordering process.

parameter	value
c_V	$(2 \pm 0.5) \cdot 10^{-3}$
H_V^M	1.04 ± 0.02 eV
f_S^0	0.67 ± 0.01

Figure 6.8 shows the evolution of the ordered domain size with temperature. The simulation was done using the parameters from the fit. The simulation is compared to the values of the ordered domain size obtained experimentally in chapter 5.5. For HPT deformed FeAl measured directly after deformation and after heating to 170°C there is a good accordance between the simulation and the experimental data. It should be noted that for the initial ordered domain size there is a perfect agreement strongly supporting the assumption of disordering by APB. The ordered domain size measured for the sample heated to 220°C is significantly smaller than the result from the simulation. This is not surprising, as the model presented here takes only into account APB but not dislocations and other effects. In chapter 5.6 it was shown that the APB and the dislocations interact. While before around 200°C heating leads to a reordering by the coarsening of the APB only, at higher temperatures the

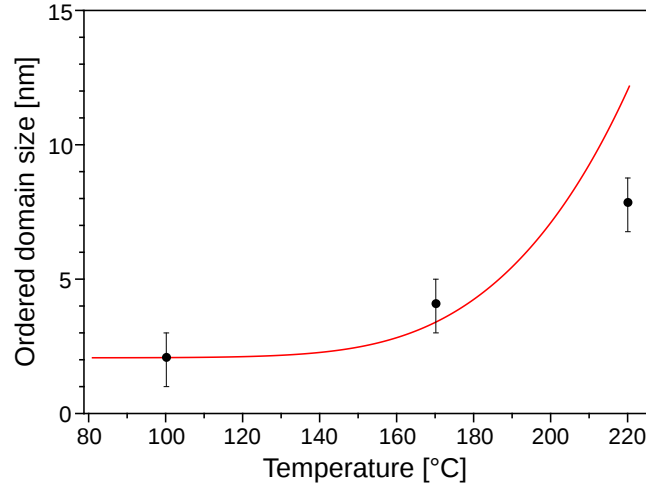


Figure 6.8: Simulated ordered domain size in dependence of temperature. The simulation is compared with experimental data taken from chapter 5.5. While the model shows a good accordance at low temperatures, where purely reordering takes place, a deviation can be observed at higher temperatures.

movement of the APB starts to be strongly hindered by dislocations and small-angle grain boundaries slowing down the reordering process.

The evolution of the APB density with temperature is shown in Figure 6.9. The initial density is very high due to the severe plastic deformation. Heating leads to a rapid decay of the APB density. At higher temperatures the decay slows down as the APB need to travel a larger distance to annihilate.

6.5 Fitting the Model to a DSC Curve of an Annealed Sample

It is also possible to fit the model to the DSC curve of nanocrystalline FeAl that was preannealed. When the sample is annealed, the ordered domain size grows and therefore an other starting value for the f_S has to be used. This means that in equation 6.16 the boundary condition changes to

$$f_S(0) = f_S^*, \quad (6.17)$$

where f_S^* is the fraction of atoms not in APB after the annealing treatment. (It should be noted that in the expression for the vacancy concentration, f_S^0 still represents the value directly after deformation because c_V^0 also represents the vacancy

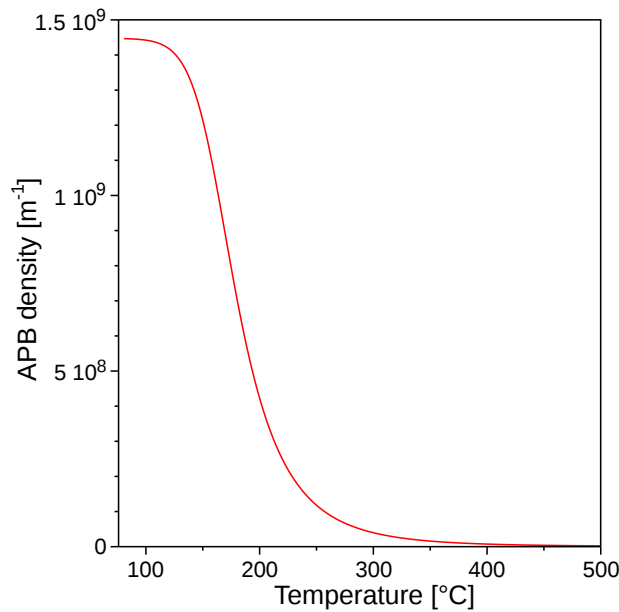


Figure 6.9: Simulated APB density in dependence of temperature. Initially the density is very high due to the severe plastic deformation but drops quickly when increasing the temperature.

density after deformation.)

To determine f_S^* the reordering model is used to calculate f_S for the specific treatment. Heating to 220°C leads for example to $f_S^* = f_S(220^\circ\text{C})$. More complicated annealing programs containing multiple isothermal and isochronal steps can be solved by using the corresponding models after each other.

To check the reliability of the model two samples were used, one annealed at 185°C and a second one annealed at 220°C. For the annealing treatment a DSC was used. The samples were heated to the desired temperature with a rate of 20 K/min followed by an annealing step for 10 minutes and subsequently cooled back to room temperature with 20 K/min. While directly after deformation f_S is 0.67, after annealing at 185°C it rises to $f_S^* = 0.957$. Annealing at 220°C decreases the APB density even more leading to a $f_S^* = 0.983$.

Figure 6.10 shows the DSC curves of the annealed samples and the corresponding simulated heat flow. It is important to note that for the simulations no parameters were adjusted. The parameters used are those obtained in chapter 6.4 and the boundary condition f_S^* was obtained from solving the model. The onset of the

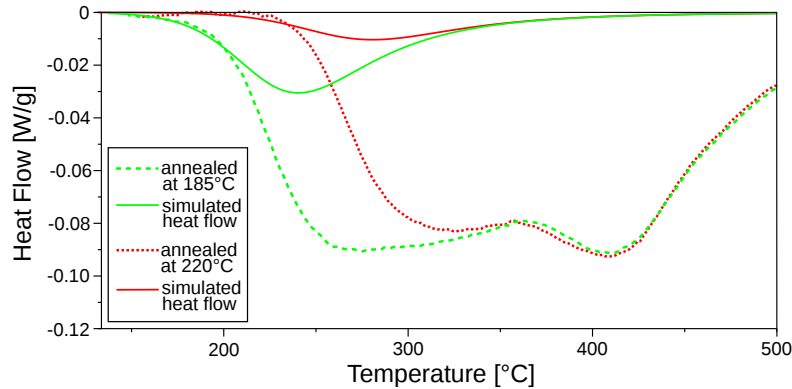


Figure 6.10: DSC curves of HPT deformed FeAl samples annealed for 10 minutes at 185°C and at 220°C. The simulated curves were obtained using the parameters determined in chapter 6.4 without adjusting any free parameters. The onset of the curves is represented well by the simulations, but there is a big difference in the area of the curves that can be explained because of the heat flow coming from recovery and grain growth taking place after 220°C.

curves is represented well by the simulations. The big differences between the DSC curves and the simulations can be explained because recovery and grain growth take place after 220°C (cf. Fig. 5.6).

6.6 Comparison of the Values with Literature Data

In the following the parameters determined from the model are compared with values from the literature. A vacancy concentration of 10^{-4} is typically observed in metals close to the melting temperature. In FeAl the situation is quite different, vacancy densities as high $5 \cdot 10^{-3}$ can be reached after quenching from the melt [Jordan03]. During severe plastic deformation and especially HPT deformation it is assumed that a very high vacancy concentration is reached [Sauvage05]. In this light the value of $2 \cdot 10^{-3}$ determined in this work is realistic.

For highly deformed materials, vacancy densities $> 10^{-3}$ cannot be determined experimentally. In positron annihilation vacancy concentrations in the range of around 10^{-6} to 10^{-3} can be measured [Krause92]. To determine quenched-in thermal vacancies there are other experimental methods, e.g. the measurement of

density changes. These methods are not applicable to deformed materials, as deformed materials usually contain a wide range of different kinds of defects that cannot be separated from each other. Therefore the possibility to measure the vacancy concentration in intermetallic compounds by fitting a reordering model to a DSC curve gives very valuable insight into HPT deformed materials.

The fraction of atoms not in APB after deformation of 0.67 is best expressed as an ordered domain size of 2.07 nm. This value is plausible as shown in the TEM investigations (cf. chapter 5.5) but it is not possible to compare the value with literature data from ball-milled FeAl, as the disordering by APB was not described in the literature prior to this work.

When comparing the vacancy migration enthalpy H_M^V with literature data, it is important to remember that H_M^V strongly depends on the order parameter S . A review of experimental values measured for FeAl is given in [Jordan03] and most measured values lie around 1.7 eV. The significantly lower value of 1.04 eV measured in this work can be explained as the vacancies have to move along the APB rather than through the ordered material. Therefore the value determined here represents the value for disordered FeAl.

6.7 The Effect of Pressure on the Reordering

In a next step the reordering of FeAl under pressure is investigated. When a hydrostatic pressure p is applied to the sample the vacancy migration is hindered, because the enthalpy increases to

$$H_V^M + p \cdot V_V^M. \quad (6.18)$$

Here V_V^M denotes the vacancy migration volume, i.e. the volume change during the migration jump.

Figure 6.11 shows DSC curves of HPT deformed FeAl samples that were annealed for 10 minutes at 220°C, one sample was annealed at ambient pressure, one at 4 GPa and one at 8 GPa. The annealing under pressure was done using the HPT machine. For the hydrostatic pressure the sample was compressed between the HPT anvils and heating was achieved by a induction coil while the temperature was measured using a pyrometer.

The DSC curves of the samples annealed under pressure show an onset at lower temperatures as compared to the sample annealed at ambient pressure. This can

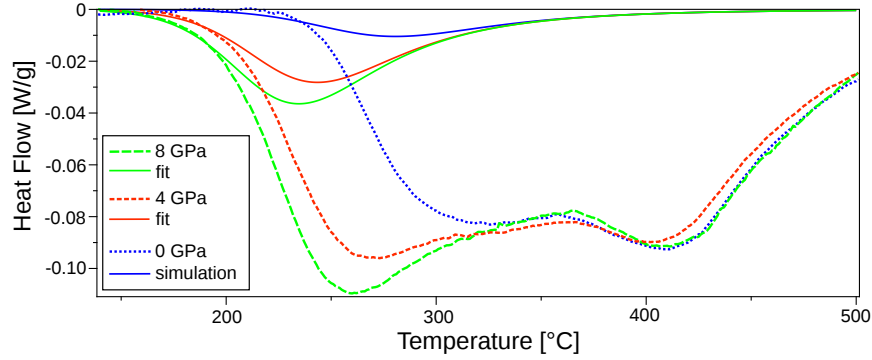


Figure 6.11: DSC curves of HPT deformed FeAl that was annealed at 220°C under various hydrostatic pressures. With increasing pressure the onset is shifted to lower temperatures. The reason is that due to the increase of the vacancy migration enthalpy with pressure, the reordering during annealing is slowed down. The fits of the reordering model to the DSC curves were used to determine the change in the vacancy migration enthalpy.

be explained as the reordering under pressure is more difficult. Therefore less reordering is achieved, i.e. a smaller f_S^* is reached. As shown in Figure 6.6 a smaller initial f_S leads to an onset of the heat flow at lower temperature.

The fraction of atoms not in APB after annealing under pressure f_S^* was determined by fitting the reordering model to the DSC curves (cf. Fig. 6.11). In the fit it was tried to reach a good agreement to the onset. The area of the curve was not taken into account as in this temperature region the heat flow due to relaxation and grain growth starts to be of importance. For the sample annealed at 8 GPa a value of $f_S^* = 0.95$ was determined and for that annealed at 4 GPa a value of $f_S^* = 0.96$. These values are smaller as compared to the value simulated for the sample annealed at ambient pressure $f_S^* = 0.983$ (cf. chapter 6.5). It is interesting to note annealing at 220°C under a pressure of 8 GPa has about the same effect as annealing at a considerably lower temperature of 185°C at ambient pressure ($f_S^* = 0.95$ and 0.957 respectively).

After determining the vacancy migration enthalpy in dependence of the pressure it is possible to determine the vacancy migration volume. Figure 6.12 shows a plot of $p \cdot V_V^M$ against p . From a linear fit V_V^M was determined to be 0.013 ± 0.002 eV/GPa or $(2.1 \pm 0.3) \cdot 10^{-30}$ m³. Expressing the volume in terms of the average atom volume

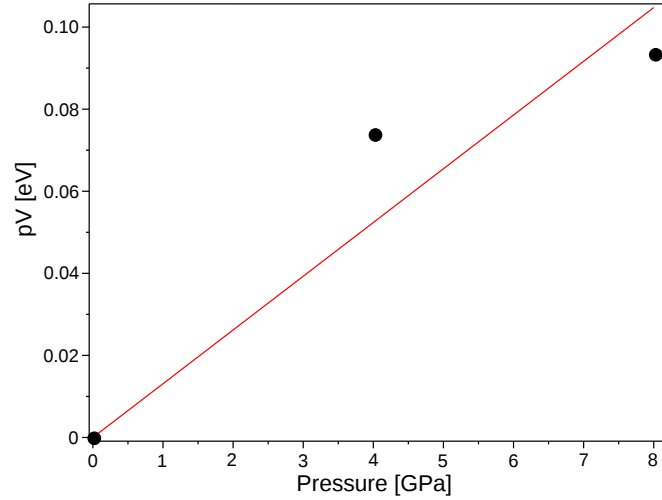


Figure 6.12: Plot of the change in the vacancy migration enthalpy due to the hydrostatic pressure $p \cdot V_V^M$ in dependence of the pressure p . The points should lie on a straight line where the slope corresponds to the vacancy migration volume V_V^M . The line represents a linear regression that was used to determine V_V^M .

V_a yields

$$V_V^M = (0.175 \pm 0.025) \cdot V_a. \quad (6.19)$$

This value is in the range expected for vacancy migration volumes. A value of $0.15 \cdot V_a$ was reported in the case of gold [Emrick61] and aluminium [Mendeleev07]. Measurements of V_V^M in ordered Fe39at.%Al by positron annihilation report a value as high as $4.6 \cdot V_a$ [Müller00, Müller01]. This value is explained by a complex diffusion process in the ordered compound and by divacancies. The value determined in the present work on the other hand is linked to single vacancy jumps in the APB.

6.8 The Effect of Unloading

The possibility to determine the vacancy concentration indirectly from the reordering behaviour allows to study the vacancy concentration after the HPT deformation. HPT deformation is carried out under a very high pressure, therefore the defect concentration and especially the vacancy concentration that can accumulate is much higher than in conventional deformation processes, because annihilation is

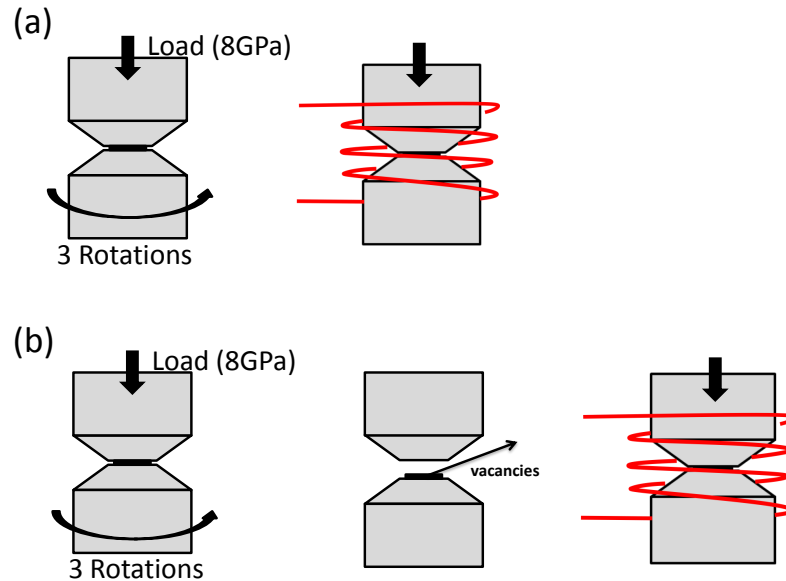


Figure 6.13: Experimental setup for the determination of the vacancy concentration in HPT deformed FeAl before and after unloading. While in (a) a sample is deformed and annealing is performed without unloading, in (b) the sample is unloaded before annealing thus allowing vacancies to leave the material. The difference in the vacancy concentration can be determined as it has an effect on the reordering during annealing.

more difficult under pressure. It is expected that a lot of non-equilibrium vacancies are lost upon unloading. Therefore it is of interest to compare the vacancy concentration in HPT deformed FeAl before and after unloading.

Figure 6.13 shows the experimental setup used to study the effect of unloading. In a first experiment HPT deformation is carried out followed by an annealing treatment at 220°C without releasing the pressure (cf. Fig. 6.13a). In the second experiment the sample is unloaded after deformation. Upon unloading the vacancy concentration decreases. After unloading, the sample is loaded again and the annealing is performed in the same way as in the previous experiment (cf. Fig. 6.13b). Therefore, the only difference is the unloading step and thus the change in vacancy concentration.

In Figure 6.14 the resulting DSC curves are shown. The DSC curve of the sample annealed at 8 GPa after unloading was already shown in Figure 6.11. The onset

of the DSC curve of the sample not unloaded before annealing shows a shift to higher temperatures. The reason for that is the higher vacancy concentration after deformation c_V^0 causing a higher reordering and at the given pressure thus a higher f_S^* . As shown in Figure 6.6 a bigger initial f_S shifts the onset of the heat flow to higher temperatures. To quantify the change, a model with an increased vacancy concentration was fitted to the DSC curve of the sample that was not unloaded (the higher vacancy concentration has to be used also for modelling the annealing treatment). The onset of the fitted curve is reproduced well by the modelled heat flow. From the fit the vacancy concentration prior to unloading was determined

$$c_V^0(\text{prior to unloading}) = 4.3 \cdot 10^{-3}.$$

This value is about a factor 2 larger than the value determined after unloading ($2 \cdot 10^{-3}$), meaning that about half of the vacancies leave the sample upon unloading. It is important to note that vacancies leaving the sample upon unloading do not participate in the reordering as they use fast pathways such as dislocation networks and end up very quickly in sinks. To check the effect of the unloading time two samples were annealed under pressure. One that has been unloaded for 1 second and one that has been unloaded for 1 hour. No difference was visible between the samples and therefore it can be concluded that the vacancies leave the sample very quickly after unloading.

The role of hydrostatic pressure and the effect of unloading is a widely discussed issue in the field of SPD and especially HPT deformation [Zehetbauer03]. Recently synchrotron experiments of deformed Cu samples frozen in liquid nitrogen prior to unloading have shown a considerable effect of the unloading on the microstructure [Schafner10, Schafner11]. In the present result, the vacancy decrease upon unloading and the slowed down vacancy migration were verified experimentally. This results give new insight into the effect of the hydrostatic pressure.

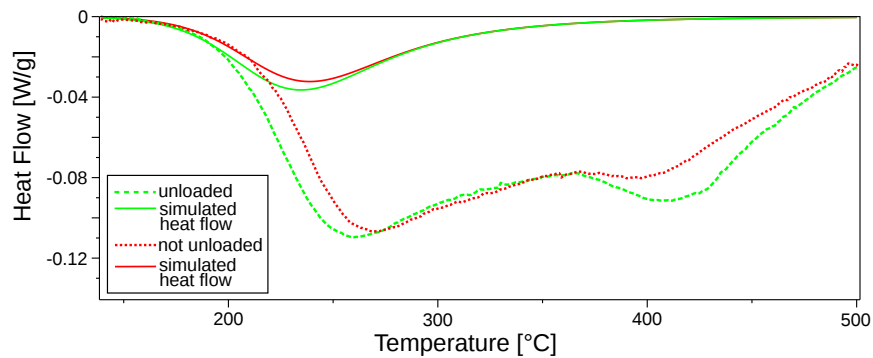


Figure 6.14: DSC curves of HPT deformed FeAl that was annealed at 220°C under a pressure of 8 GPa. One curve was obtained from a sample unloaded prior to annealing while the other sample was not unloaded. The onset of the DSC curve of the sample that was not unloaded is shifted to higher temperatures. The higher vacancy density prior to unloading leads to an increased reordering during annealing (and thus to a higher f_S^*). A fit of the reordering model to the curves is shown. It was used to determine the vacancy concentration prior to unloading.

7 Summary and Conclusions

“It’s more fun to arrive at a conclusion than to justify it.”

– Malcolm Forbes

Transmission electron microscopy (TEM) is a valuable tool for the structural characterization of bulk nanocrystalline materials produced by severe plastic deformation (SPD). In the present work, by applying state-of-the-art and newly developed TEM methods combining imaging and diffraction contrast, an in-depth structural analysis of nanostructured FeAl is obtained. Profile analysis using selected area diffraction patterns (PASAD) is successfully applied for a quantitative analysis of nanocrystalline FeAl. In addition PASAD is applicable to various nanomaterials. A selected area diffraction pattern is recorded from the area of interest that is selected in TEM images at high magnifications. The large amount of nanograins present in the selected area aperture gives rise to a ring pattern in the diffraction plane. An intensity profile can be obtained from the ring pattern by azimuthal integration. Key microstructural parameters can be determined from the diffracted intensity by profile analysis as it has been done previously only for X-ray diffraction. A state-of-the-art profile analysis using the modified Williamson-Hall plot was carried out to get the coherently scattering domain (CSD) size. Diffraction patterns were recorded on a 7 megapixel CCD-camera, allowing to obtain diffraction profiles up to very high angles. In order to achieve a high precision, computer assisted routines for the centre determination, the azimuthal integration and the peak fitting were developed. To make the method widely available, an elaborate software with more than 7500 lines of code was written and implemented as a plugin for DigitalMicrograph. The software has an intuitive graphical user interface and was released for free to the community.

The B2 ordered intermetallic Fe-45at.%Al alloy was made by induction melting from pure components and was grown to a single crystal using a modified Bridgman method. Slices of the single crystal were deformed by high pressure torsion (HPT)

to achieve a nanocrystalline structure. Samples were cut from the deformed disks and thinned for the TEM investigations using twin-jet electropolishing. In the case of FeAl, the evolution of the nanocrystalline structure occurs in an inhomogeneous way. In the beginning of the deformation narrow bands (~ 300 nm wide) containing a nanocrystalline structure are observed. With increasing shear strain γ the volume fraction of the nanocrystalline material increases until at $\gamma > 5000\%$ the whole volume of the specimen is nanocrystalline. PASAD was used to determine the evolution of the CSD size in the small nanocrystalline regions that are formed during deformation. As a main result it was found that the CSD size is not changing as a function of strain, which is rather unexpected. It should be pointed out that the result obtained in the case of the band-shaped nanostructure could only be obtained by using a local profile analysis as developed in this work. In the case of the homogeneously nanocrystalline sample, the results were compared with those of X-ray diffraction showing a good agreement.

To analyse nanocrystalline structures quantitatively in 3D a novel method was developed based on electron diffraction. It allows to reconstruct the average size and morphology of the CSD in a straightforward way using a single TEM specimen. PASAD is applied using different tilt positions of the sample. As a result the average CSD size in three orthogonal directions is obtained. This is achieved by integrating over the corresponding sector of the diffraction rings. Standard tomography can not be applied to the analysis of bulk nanocrystalline materials since the contrast of the grains sensitively depends on the tilt of the specimen. Contrary to that the present method can be successfully applied to bulk nanocrystalline materials, as shown in the case of nanocrystalline FeAl, where the average size of the CSD was determined in 3D. It was deduced that the CSD are elongated parallel to the shear plane, having a width of 19 ± 2 nm, a length of 18 ± 1 nm and a height of 10 ± 1 nm. A comparison with TEM images obtained from cross-section samples showed that the dimensions of the average CSD are smaller and less elongated than those of the grains indicating the occurrence of subgrain boundaries.

To study the thermal stability, methods of TEM and differential scanning calorimetry (DSC) were applied to nanocrystalline FeAl. The signal obtained from an isochronal DSC measurement shows three overlapping exothermic peaks. The three exothermic peaks correspond to reordering, the recovery of dislocations and grain growth. For a systematic TEM study samples were heated to different temperatures.

It was reported in the literature that in FeAl the B2 long-range order is lost during SPD. In contrast the present work revealed that the disorder is not complete. The partial destruction of the long-range order in FeAl caused by HPT deformation and the process of reordering by heating were analysed in detail. TEM methods combining the findings of diffraction contrast (using PASAD), dark-field images (taken with both fundamental and superlattice reflections) and high resolution images (including Fourier filtered images of selected superlattice reflections) were used. For ordered domains >3 nm diffraction methods can be applied to determine the size of the ordered domains whereas for smaller ordered domains TEM dark-field images with superlattice reflections have to be used to reveal the ordered domains clearly. It was shown that by HPT deformation ordered nanodomains of about 2 nm (the typical length scale of medium range order) are formed. The nanodomains, separated by antiphase boundaries (APB), are densely packed and homogeneously distributed within the grains. Upon heating, reordering occurs by the coarsening of the nanodomains until the ordered domains reach the size of the grains. The deformation induced disordering by nanodomains separated by sharp APB is different from a thermally induced one occurring in other alloys with a order-disorder transition.

Thermal treatment does not only lead to chemical reordering, but also to the recovery of dislocations and the rearrangement of grain boundaries. To study these processes, the ordered domain size, the CSD size and the grain size were monitored at the same time during annealing. The grain size was determined from dark-field images, while the CSD size was determined by PASAD. Using diffraction pattern reconstruction from dark-field images it was shown that the grains of the as-deformed state contain substructures separated by small-angle grain boundaries. Annealing up to 220°C leads to reordering by the growth of nanosized ordered domains. The dislocation density is reduced while the grain and subgrain size stays constant. The movement of the dislocations is linked to the movement of the APB. Annealing further to 370°C leads to a reduction in grain size by a factor of 2, while the CSD size increases by a factor of 2 and the ordered domain size by a factor of 15. Diffraction pattern reconstruction revealed that only large-angle grain boundaries are present in the annealed sample. The grain size reduction is explained by the following model: A high density of dislocations is present in the sample after SPD. The coarsening of the ordered domains acts as a driving force moving the dislocations to the subgrain boundaries and the large-angle boundaries thus

converting the subgrain boundaries into large-angle boundaries. The reordering starts at temperatures as low as 130°C. Therefore the driving force is effective at a temperature below the temperature at which the dislocations annihilate by climb. Furthermore, the present results help to clarify a widely discussed discrepancy between the grain size and the crystallite size (equal to the CSD size). Both values were measured in the TEM from the same regions of the sample. In the case of as-deformed FeAl the CSD size is smaller or equal than the grain size, because the nanograins contain subgrain boundaries, but they approach a common value upon heating. This leads to the result that the crystallite size is smaller than the grain size.

Based on the coarsening of the chemically ordered nanodomains, a model for the reordering process was developed that can be fitted to the exothermal heat flow measured by DSC using a constant heating rate. From the results of the modelling the vacancy migration enthalpy, the vacancy concentration after deformation, the APB density after deformation and their effects on the reordering process were determined. From the APB density after deformation an ordered domain size of 2 nm was deduced, which is in good accordance with the value measured by TEM investigations. The rather low vacancy migration enthalpy of 1.04 eV represents the value for disordered FeAl as the vacancies have to move along the APB rather than through the ordered material. A high vacancy concentration of $2 \cdot 10^{-3}$ was obtained as it is expected after HPT deformation. The present model allows to determine important macroscopic parameters in intermetallics, e.g. the vacancy densities after SPD, which are usually very difficult to measure experimentally. Applying the model to a sample that was preannealed also allows to determine the APB density after the annealing treatment.

An extended model was used to investigate the reordering of FeAl under pressure. When a hydrostatic pressure is applied to the sample the vacancy migration is hindered because the vacancy migration enthalpy increases. To anneal the samples under high pressures, a heating element was mounted on the HPT machine. It was shown that the APB density after annealing at 220°C changes when pressure is applied during the heat treatment. The higher the pressure, the less reordering is achieved. This can be explained by the fact that processes of reordering under pressure are hindered as compared to those occurring without pressure. By applying different pressures it was determined that the vacancy migration volume is 17.5% of the average atom volume. This value is in the range that is expected for vacancy

migration volumes.

The possibility to determine the vacancy concentration from the reordering behaviour allows to study the effect of pressure release on the vacancy concentration. HPT deformation is carried out under a very high pressure, therefore the defect concentration and especially the vacancy concentration that can accumulate is much higher than in conventional deformation processes. It is expected that a large fraction of the non-equilibrium vacancies is lost upon unloading. To compare the vacancy concentration in HPT deformed FeAl before and after unloading, HPT deformation was carried out followed by an annealing treatment at 220°C without releasing the pressure. In a second experiment, the pressure was released and after unloading the sample was loaded again and the annealing was performed in the same way as in the experiment without unloading. From the fit the vacancy concentration prior to unloading was determined to be about a factor 2 larger than the value determined after unloading. The role of hydrostatic pressure for HPT deformation and the effect of unloading is widely discussed. In the present work, the decrease of the vacancy concentration upon unloading and the reduced vacancy migration were verified experimentally.

Included Publications

- [Gammer10] C. Gammer, C. Mangler, C. Rentenberger and H.P. Karnthaler. Quantitative local profile analysis of nanomaterials by electron diffraction. *Scripta Materialia*. 63:312–315, 2010. doi:10.1016/j.scriptamat.2010.04.019
- [Gammer11a] C. Gammer, C. Mangler, C. Rentenberger and H.P. Karnthaler. Growth of nanosized chemically ordered domains in intermetallic FeAl made nanocrystalline by severe plastic deformation. *Scripta Materialia*. 65:57–60, 2011. doi:10.1016/j.scriptamat.2011.03.002
- [Gammer11b] C. Gammer, C. Mangler, C. Rentenberger and H.P. Karnthaler. 3D Analysis by Electron Diffraction Methods of Nanocrystalline Materials. *Microscopy and Microanalysis*, in print, 2011. doi:10.1017/S1431927611011962
- [Mangler10] C. Mangler, C. Gammer, C. Rentenberger and H.P. Karnthaler. Structural modifications during heating of bulk nanocrystalline FeAl produced by high-pressure torsion. *Acta Materialia*. 58:5631–5638, 2010. doi:10.1016/j.actamat.2010.06.036
- [Mangler11] C. Mangler, C. Gammer, K. Hiebl, H.P. Karnthaler and C. Rentenberger. Thermally induced transition from a ferromagnetic to a paramagnetic state in nanocrystalline FeAl processed by high-pressure torsion. *Journal of Alloys and Compounds*. 509:S389–S392, 2011. doi:10.1016/j.jallcom.2010.12.023

Bibliography

- [Abbe1873] E. Abbe. Beiträge zur Theorie des Mikroskops und der mikroskopischen Wahrnehmung. *Archiv für mikroskopische Anatomie*. 9:413, 1973. ISSN:0176-7364
- [Amils00] X. Amils, J. Nogues, S. Surinach, M.D. Baro, M.A. Munoz-Morris and D.G. Morris. Hardening and softening of FeAl during milling and annealing. *Intermetallics*. 8:805–813, 2000. doi:10.1016/S0966-9795(00)00013-3
- [Amils01] X. Amils, J.S. Garitaonandia, J. Nogues, S. Surinach, F. Plazaola, J.S. Munoz and M.D. Baróa. Micro- and macroscopic magnetic study of the disordering (ball milling) and posterior reordering (annealing) of Fe-40 at.%Al. *Journal of Non-Crystalline Solids*. 287:272–276, 2001. doi:10.1016/S0022-3093(01)00586-5
- [Amils99] X. Amils, J. Nogues, J.S. Munoz, S. Surinach and M.D. Baro. Correlation between Magnetic and Structural Parameters in Fe-40Alat.% Nanostructured Alloys. *Materials Science Forum*. 312:513–538, 1999. doi:10.4028/www.scientific.net/JMNM.2-6.531
- [AnizC] A. Borbely. AnizC – Computer program for the calculation of dislocation orientation factors in anisotropic cubic, hexagonal and trigonal crystals. <http://metal.elte.hu/anizc>
- [Apinaniz03] E. Apinaniz, F. Plazaola, J. S. Garitaonandia, D. Martin, G. Cuello, J. A. Jimenez, J. I. Perez-Landazabal and V. Recarte. Systematic study of the reordering process in FeAl alloys by neutron diffraction. *Journal of Non-Crystalline Solids*. 329:39–42, 2003. doi:10.1016/j.jnoncrysol.2003.08.009
- [Ashby70] M.F. Ashby. The deformation of plastically non-homogeneous materials. *Philosophical Magazine*. 21:399–424, 2006. doi:10.1080/14786437008238426

- [Arslan05] I. Arslan, T.J.V. Yates, N.D. Browning and P.A. Midgley. Embedded nanostructures revealed in three dimensions. *Science*. 309:2195–2198, 2005. doi:10.1126/science.1116745
- [ASTAR] Nanomegas. ASTAR – Automatic phase and orientation mapping for TEM. www.nanomegas.com
- [Avrami39] M. Avrami. Kinetics of Phase Change I: General Theory. *Journal of Chemical Physics*. 7:1103–1112, 1939. doi:10.1063/1.1750380
- [Bakker95] H. Bakker, G. F. Zhou and H. Yang. Mechanically driven disorder and phase transformations in alloys. *Progress in Materials Science*. 39:159–241, 1995. doi:10.1016/0079-6425(95)00001-1
- [Balogh06] L. Balogh, G. Ribárik, and T. Ungár. Stacking faults and twin boundaries in fcc crystals determined by x-ray diffraction profile analysis. *Journal of Applied Physics*. 100:023512, 2006. doi:10.1063/1.2216195
- [Balzar93] D. Balzar and H. Ledbetter. Voigt-function modeling in Fourier analysis of size- and strain-broadened X-ray diffraction peaks. *Journal of Applied Crystallography*. 26:97–103, 1993. doi:10.1107/S0021889892008987
- [Balzar96] D. Balzar and S. Popovic. Reliability of the Simplified Integral-Breadth Methods in Diffraction Line-Broadening Analysis. *Journal of Applied Crystallography*. 29:16–23, 1996. doi:10.1107/S0021889895008478
- [Balzar99] D. Balzar, in *Defect and Microstructure Analysis from Diffraction*, edited by R.L. Snyder, H.J. Bunge, and J. Fiala, International Union of Crystallography Monographs on Crystallography No. 10 (pp. 94–126). Oxford University Press, New York, 1999. ISBN:9780198501893
- [Bei08] H. Bei, S. Shima, G.M. Pharr and E.P. George. Effects of pre-strain on the compressive stress–strain response of Mo-alloy single-crystal micropillars. *Acta Materialia*, 56:4762–4770, 2008. doi:10.1016/j.actamat.2008.05.030
- [Beyerlein11] K.R. Beyerlein, R.L. Snyder and P. Scardi. Powder diffraction line profiles from the size and shape of nanocrystallites. *Journal of Applied Crystallography*. 44:945–953, 2011. doi:10.1107/S0021889811030743

- [Borbely01] A. Borbely and I. Groma. Variance method for the evaluation of particle size and dislocation density from x-ray Bragg peaks. *Applied Physics Letters* 79:1772, 2001. doi:10.1063/1.1404134
- [Borisenko09] K.B. Borisenko, Y. Chen, S.A. Song, D. Nguyen-Manh and D.J.H. Cockayne. A concerted rational crystallization/amorphization mechanism of $\text{Ge}_2\text{Sb}_2\text{Te}_5$. *Journal of Non-Crystalline Solids*. 355:2122–2126, 2009. doi:10.1016/j.jnoncrysol.2009.06.029
- [Born80] M. Born and E. Wolf. *Principles of Optics*. Pergamon Press, Oxford, 1980. ISBN:9780521784498
- [Bragg34] W.L. Bragg and E.J. Williams. The effect of thermal agitation on atomic arrangement in alloys. *Proceedings of the Royal Society of London. Series A*. 145:699–730, 1934. doi:10.1098/rspa.1934.0132
- [Bragg35] W.L. Bragg and E.J. Williams. The effect of thermal agitation on atomic arrangement in alloys II. *Proceedings of the Royal Society of London. Series A*. 151:540–566, 1935. doi:10.1098/rspa.1935.0165
- [Breadth] D. Balzar. Breadth – A PC program for analyzing diffraction-line broadening. <http://mysite.du.edu/~balzar/breadth.htm>
- [Bridgman43] P.W. Bridgman. On Torsion Combined with Compression. *Journal of Applied Physics*. 14:273, 1943. doi:10.1063/1.1714987
- [Broglie25] L. de Broglie. Recherches sur la Théorie des Quanta. *Annales de Physique*. 10e t.III, 1925. ISSN:0003-4169
- [Budrovic04] Z. Budrovic, H. Van Swygenhoven, P.M. Derlet, S. Van Petegem and B. Schmitt. Plastic Deformation with Reversible Peak Broadening in Nanocrystalline Nickel. *Science*. 304:273–276, 2004 doi:10.1126/science.1095071
- [Cahn02] R. Cahn. How does long-range order affect creep of alloys? *Materials Science and Engineering A*. 324:1–4, 2002. doi:10.1016/S0921-5093(01)01273-4
- [Cai99] B. Cai, Q.P. Kong, L. Lu and K. Lu. Interface controlled diffusional creep of nanocrystalline pure copper. *Scripta Materialia*. 41:755–759, 1999. doi:10.1016/S1359-6462(99)00213-4

- [Carlton07] C.E. Carlton and P.J. Ferreira. What is behind the inverse Hall–Petch effect. *Acta Materialia*. 55:3749–3756, 2007. doi:10.1016/j.actamat.2007.02.021
- [Cerny00] R. Cerný, J.M. Joubert, M. Latroche, A. Percheron-Guégan and K. Yvon. Anisotropic diffraction peak broadening and dislocation substructure in hydrogen-cycled LaNi_5 and substitutional derivatives. *Journal of Applied Crystallography*. 33:997–1005, 2000. doi:10.1107/S0021889800004556
- [Chen03] M. Chen, E. Ma, K.J. Hemker, H. Sheng, Y. Wang and X. Cheng. Deformation twinning in nanocrystalline aluminum. *Science*. 300:1275–1277, 2003. doi:10.1126/science.1083727
- [Chen09] L.C. Chen and F. Spaepen. Analysis of calorimetric measurements of grain growth. *Journal of Applied Physics*. 69:679–688, 2009. doi:10.1063/1.347349
- [Chokshi89] A.H. Chokshi, A. Rosen, J. Karch and H. Gleiter. On the validity of the hall-etch relationship in nanocrystalline materials. *Scripta Metallurgica*. 23:1679–1683, 1989. doi:10.1016/0036-9748(89)90342-6
- [Christian65] J.W. Christian. *The Theory of Transformations in Metals and Alloys*. Pergamon Press, First edition, 1965. ISBN:9780080440194
- [Ciuca10] O. Ciuca, K. Tsuchiya, Y. Yokoyama, Y. Todaka and M. Umemoto. Heterogeneous Process of Disordering and Structural Refinement in Ni_3Al during Severe Plastic Deformation by High-Pressure Torsion. *Materials Transactions*. 51:14–22, 2010. doi:10.2320/matertrans.MB200915
- [Coble63] R.L. Coble. A Model for Boundary Diffusion Controlled Creep in Polycrystalline Materials. *Journal of Applied Physics*. 34:1679–1682, 1963. doi:10.1063/1.1702656
- [Correa10] R. Bernal-Correa, A. Rosales-Rivera, P. Pineda-Gomez and N.A. Salazar. Structural and magnetic properties of $\text{Fe}_{60}\text{Al}_{40}$ alloys prepared by means of a magnetic mill. *Journal of Alloys and Compounds*. 495:491–494, 2010. doi:10.1016/j.jallcom.2009.08.085

- [Cowley95] J.M. Cowley. *Diffraction Physics, Third Edition*. North Holland, 1995. ISBN:9780444822185
- [Dahmen09] U. Dahmen, R. Erin , V. Radmilovic, C. Kisielowsk, M.-D. Rossell and P. Denes. Background, status and future of the Transmission Electron Aberration-corrected Microscope project. *Philosophical Transactions A*. 367:3795–3808, 2009. doi:10.1098/rsta.2009.0094
- [Davisson27] C. J. Davisson and L. H. Germer. Diffraction of Electrons by a Crystal of Nickel. *Physical Review*. 30:705–740, 1927. doi:10.1103/PhysRev.30.705
- [Deevi96] S.C. Deevi and V.K. Sikka. Nickel and iron aluminides: an overview on properties, processing, and applications. *Intermetallics*. 4:357–375, 1996. doi:10.1016/0966-9795(95)00056-9
- [DeGraef03] M. De Graef *Introduction to Conventional Transmission Electron Microscopy*. Cambridge University Press, 2003. ISBN:9780521629959
- [Dingley06] D.J. Dingley. Orientation Imaging Microscopy for the Transmission Electron Microscope. *Microchim Acta*. 155:19–29, 2006. doi:10.1007/s00604-006-0502-4
- [Divinski11] S.V. Divinski, G. Reglitz, H. Rösner, Y. Estrin and G. Wilde. Ultra-fast diffusion channels in pure Ni severely deformed by equal-channel angular pressing. *Acta Materialia*. 59:1974–1985, 2011. doi:10.1016/j.actamat.2010.11.063
- [Edalati09] K. Edalati, E. Matsubara and Z. Horita. Processing Pure Ti by High-Pressure Torsion in Wide Ranges of Pressures and Strain. *Metallurgical and Materials Transactions A*. 40:2079–2086, 2009. doi:10.1016/10.1007/s11661-009-9890-5
- [Emrick61] R. M. Emrick. Pressure Effect on Vacancy Migration Rate in Gold. *Physical Review*. 122:1720–1733, 1961. doi:10.1103/PhysRev.122.1720
- [Engler09] O. Engler and V. Randle. *Introduction to Texture Analysis: Macrotexture, Microtexture, and Orientation Mapping, Second Edition*. CRC Press, 2009. ISBN:9781420063653

- [Ewald31] P.P. Ewald and C. Hermann *Strukturbericht 1913–1928*. Akademische Verlagsgesellschaft mbH, Leipzig, 1931.
- [Fecht07] H.J. Fecht, E. Hellstern, Z. Fu and W.L. Johnson. Nanocrystalline metals prepared by high-energy ball milling. *Metallurgical and Materials Transactions A*. 21:2333–2337, 2007. doi:10.1007/BF02646980
- [Fischer76] L. Fischer. Transmissionselektronenmikroskopische Untersuchung der Versetzungsstruktur plastisch verformter Nickel Einkristalle. Dissertation, Universität Wien, 1976.
- [Fultz05] B. Fultz and J. Howe *Transmission Electron Microscopy and Diffractometry of Materials*. Springer, 2005. ISBN:9783540437642
- [Gammer07] C. Gammer. *Distributionen als Randwerte harmonischer und analytischer Funktionen*. Diplomarbeit, Technische Universität Wien, 2007.
- [Gammer11d] C. Gammer. *Ordnungseinstellung in nanokristallinem FeAl untersucht mit Transmissionselektronenmikroskopie und dynamischer Differenzkalorimetrie*. Diplomarbeit, Universität Wien, 2011.
- [Gao09] N. Gao, M.J. Starink and T.G. Langdon. Using differential scanning calorimetry as an analytical tool for ultrafine-grained metals processed by severe plastic deformation. *Materials Science and Technology*. 6:687–698, 2009. doi:10.1179/174328409X408901
- [Geist10] D. Geist, C. Gammer, C. Mangler, C. Rentenberger, and H. P. Karnthaler. Electron microscopy of severely deformed L1₂ intermetallics. *Philosophical Magazine*. 90:4635–4654, 2010. doi:10.1080/14786435.2010.482178
- [Gialanella98] S. Gialanella, X. Amils, M.D. Baro, P. Delcroix, G. Le Caer L. Lutterotti and S. Surinach. Microstructural and kinetic aspects of the transformations induced in a FeAl alloy by ball-milling and thermal treatments. *Acta Materialia*. 46:3305–3316, 1998. doi:10.1016/S1359-6454(97)00484-9
- [Gifkins67] R.C. Gifkins. Diffusional Creep Mechanisms. *Journal of the American Ceramic Society*. 51:69–72, 1967. doi:10.1111/j.1151-2916.1968.tb11838.x

- [Girifalco64] L. A. Girifalco. Vacancy concentration and diffusion in order-disorder alloys. *Journal of Physics and Chemistry of Solids*. 24:323–333, 1964. doi:10.1016/0022-3697(64)90111-8
- [Gleiter00] H. Gleiter. Nanostructured materials: basic concepts and microstructure. *Acta Materialia*. 48:1–29, 2000. doi:10.1016/S1359-6454(99)00285-2
- [Goodman05] J.W. Goodman. *Introduction to Fourier Optics, Third Edition*. Roberts & Co, United States, 2005. ISBN:9780974707723
- [Groma88] I. Groma, T. Ungár and M. Wilkens. Asymmetric X-ray line broadening of plastically deformed crystals. I. Theory. *Journal of Applied Crystallography*. 21:47–54, 1988. doi:10.1107/S0021889887009178
- [Groma98] I. Groma. X-ray line broadening due to an inhomogeneous dislocation distribution. *Physical Review B*. 57:7535–7542, 1998. doi:10.1103/PhysRevB.57.7535
- [Gupta88] A.K. Gupta, A.K. Jena, M.C. Chaturvedi. A differential technique for the determination of the activation energy of precipitation reactions from differential scanning calorimetric data. *Scripta Metallurgica*. 22:369–371, 1988. doi:10.1016/S0036-9748(88)80207-2
- [Haasen86] P. Haasen. *Physical Metallurgy*. Cambridge University Press, 1986. ISBN:9780534921736
- [Hafok06] M. Hafok A. Vorhauer, J. Keckes and R. Pippan. HPT-Deformation of Copper and Nickel Single Crystals. *Materials Science Forum*. 503:621–626, 2006. doi:10.4028/www.scientific.net/MSF.503-504.621
- [Hall51] E. Hall. The Deformation and Ageing of Mild Steel: III Discussion of Results. *Proceedings of the Physical Society. Section B*. 64:747–753, 1951. doi:10.1088/0370-1301/64/9/303
- [Hemker04] K.J. Hemker. MATERIALS SCIENCE: Understanding How Nanocrystalline Metals Deform. *Science*. 304:221–223, 2004. doi:10.1126/science.1097058
- [Hernando98] A. Hernando, X. Amils, J. Nogues, S. Surinach, M.D. Baro and M.R. Ibarra. Influence of magnetization on the reordering of nanostructured

- ball-milled Fe-40at%Al powders. *Physical Review B*. 58:864–867, 1998. doi:10.1103/PhysRevB.58.R11864
- [Herring50] C. Herring. Diffusional Viscosity of a Polycrystalline Solid. *Journal of Applied Physics*. 21, 437–445, 1950. doi:10.1063/1.1699681
- [Hirth67] J.H. Hirth and J. Lothe. *Theory of dislocations*. McGraw-Hill, 1967. ISBN:9780894646171
- [Hoehne96] G. W. H. Hoehne, W. F. Hemminger and H.J. Flammersheim. *Differential Scanning Calorimetry – An introduction for Practitioners*. Springer-Verlag Berlin, 1996. ISBN:9783540590125
- [Howie62] A. Howie, M.J. Whelan. Diffraction Contrast of Electron Microscope Images of Crystal Lattice Defects. III. Results and Experimental Confirmation of the Dynamical Theory of Dislocation Image Contrast. *Proceedings of the Royal Society of London. Series A*. 267:206–230, 1962. doi:10.1098/rspa.1962.0093
- [Huang03] J.Y.Huang, X.Z.Liao, Y.T. Zhu, F. Zhou and E.J. Lavernia. Grain boundary structure of nanocrystalline Cu processed by cryomilling. *Philosophical Magazine*. 83:1407–1419, 2003. doi:10.1080/1478643031000083633
- [Huang07] X. Huang. Characterization of nanostructured metals produced by plastic deformation. *Journal of Materials Science*. 42:1577, 2007. doi:10.1007/s10853-006-0988-5
- [Huang93] Y. Huang and A. Menovsky. Calorimetric analysis of the grain growth in nanocrystalline copper samples. *Nanostructured Materials*. 2:587–595, 1993. doi:10.1016/0965-9773(93)90032-7
- [Humphreys04] F.J. Humphreys. Characterisation of fine-scale microstructures by electron backscatter diffraction (EBSD). *Scripta Materialia*. 51:771–776, 2004. doi:10.1016/j.scriptamat.2004.05.016
- [Hurtado95] J.A. Hurtado, B.R. Elliot, H.M. Shodja, D.V.Gorelikov, C.E. Campbell, H.E. Lippar, T.C. Isabell J. Weertmann. Disclination grain boundary model with plastic deformation by disclinations. *Materials Science and Engineering A*. 190:1–7, 1995. doi:10.1016/0921-5093(94)09592-K

- [Huygens90] C. Huygens. *Traite de la lumiere*. Leiden, Netherlands, 1690. ISBN:9782100014002
- [Jakobsen06] B. Jakobsen, H. F. Poulsen, U. Lienert, J. Almer, S. D. Shastri, H. O. Sorensen, C. Gundlach and W. Pantleon. Formation and Subdivision of Deformation Structures During Plastic Deformation. *Science* 312: 889–892, 2006. doi:10.1126/science.1124141
- [Jin04] M. Jin, A.M. Minor, E.A. Stach and J.W. Morris. Direct observation of deformation-induced grain growth during the nanoindentation of ultrafine-grained Al at room temperature. *Acta Materialia*. 52:5381–5387, 2004. doi:10.1016/j.actamat.2004.07.044
- [Jordan03] J. L. Jordan and S. C. Deevi. Vacancy formation and effects in FeAl. *Intermetallics*.11:507–528, 2003. doi:10.1016/S0966-9795(03)00027-X
- [Kattner86] U.R. Kattner. In: T.B. Massalski (Ed.), *Binary Alloy Phase Diagrams Vol.1*, ASM International, 1990. ISBN:9780871704030
- [Kelly00] A. Kelly, G. W. Groves and P. Kidd. *Crystallography and Crystal Defects*. John Wiley & Sons LTD, 2000. ISBN:9780582444911
- [Kilmametov04] A.R. Kilmametov, I.V. Alexandrov and A. Dubravina. Texture Analysis of Nanostructured Metals Produced by Severe Plastic Deformation. *Materials Science Forum*. 44:243–246, 2001. doi:10.4028/www.scientific.net/MSF.443-444.243
- [Kissinger56] H. E. Kissinger. Variation of Peak Temperature With Heating Rate in Differential Thermal Analysis. *Journal Of Research Of The National Bureau Of Standards*. 57:217–221, 1956. ISSN:00910635
- [Kissinger57] H. E. Kissinger. Reaction Kinetics in Differential Thermal Analysis. *Analytical Chemistry*. 29:1702–1706, 1957 doi:10.1021/ac60131a045
- [Klimanek88] P. Klimanek and R. Kuzel. X-ray Diffraction Line Broadening Due to Dislocations in Non-Cubic Materials. I. General Considerations and the Case of Elastic Isotropy Applied to Hexagonal Crystals. *Journal of Applied Crystallography*. 21:59–66, 1988. doi:10.1107/S0021889887009580
- [Koch06] C.C. Koch. *Nanostructured Materials: Processing, Properties and Applications*. William Andrew, 2006. ISBN:9780815514510

- [Kocks98] U.F. Kocks, C.N. Tome, H.-R. Wenk. *Texture and Anisotropy*. Cambridge University Press, 1998. ISBN:9780521794206
- [Kolb07] U. Kolb, T. Gorelik, C. Kübel, M.T. Otten and D. Hubert. Towards automated diffraction tomography: Part I–Data acquisition. *Ultramicroscopy*. 107:507–513, 2007. doi:10.1016/j.ultramic.2006.10.007
- [Korner85] A. Korner and H.P. Karnthaler. Fault energies in ordered and disordered Ni₃Fe. *Philosophical Magazine A* 52:29–38, 1985. doi:10.1080/01418618508237603
- [Korzniakov99] A. V. Korzniakov, O. Dimitrov, G. F. Korznikova, J. P. Dallas, A. Quivy, R. Z. Valiev and A. Mukherjee. Nanocrystalline structure and phase transformation of the intermetallic compound TiAl processed by severe plastic deformation. *Nanostructured Materials*. 11:17–23, 1999. doi:10.1016/S0965-9773(98)00157-3
- [Kraan86] A. M. Van der Kraan and K. H. J. Buschow. The ⁵⁷Fe Mössbauer isomer shift in intermetallic compounds of iron. *Physica B+C*. 138:55–6, 1986. doi:10.1016/0378-4363(86)90492-4
- [Krause92] R. Krause and A. Polity *Untersuchungen von Kristalldefekten mit Hilfe der Positronenannihilation*. Wiss. Zeitschrift Univ. Halle XXXXI'92, **3** (1992) 3–22.
- [Kril98] C.E. Kril and R. Birringer. Estimating grain-size distributions in nanocrystalline materials from X-ray diffraction profile analysis. *Philosophical Magazine A*. 77:621–640, 1998. doi:10.1080/01418619808224072
- [Krivoglaz95] M.A. Krivoglaz. *X-Ray and Neutron Diffraction in Nonideal Crystals*. Translated by O.A. Glebov, Springer, 1995. ISBN:9783540505648
- [Langford78] J.I. Langford and A.J.C. Wilson. Scherrer after Sixty Years: A Survey and Some New Results in the Determination of Crystallite Size. *Journal of Applied Crystallography*. 11:102–113, 1978. doi:10.1107/S0021889878012844
- [Langford96] J.I. Langford and D. Louer. Powder Diffraction. *Reports on Progress in Physics*. 59:131–234, 1996. doi:10.1088/0034-4885/59/2/002

- [Leoni06] M. Leoni, T. Confente and P. Scardi. PM2K: a flexible program implementing Whole Powder Pattern Modelling. *Zeitschrift für Kristallographie*. 2006 Issue suppl 23:249–254. doi:10.1524/zksu.2006.suppl_23.249
- [Liao04] X.Z. Liao, Y.H. Zhao, S.G. Srinivasan and Y.T. Zhu, R.Z. Valiev and D.V. Gunderov. Deformation twinning in nanocrystalline copper at room temperature and low strain rate. *Applied Physics Letters*. 84:592–594, 2004. doi:10.1063/1.1644051
- [Lin97] Jyung-Dong Lin and Jeng-Gong Duh. The use of X-ray line profile analysis to investigate crystallite size and microstrain for zirconia powders. *Journal of Materials Science*. 32:5779–5790, 1997. doi:10.1023/A:1018630103804
- [Liu07] F. Liu, and F. Sommer, C. Bos and E.J. Mittemeijer. Analysis of solid state phase transformation kinetics: models and recipes. *International Materials Reviews*. 52:193–212, 2007. doi:10.1179/174328007X160308
- [Liu11] H. H. Liu, S. Schmidt, H. F. Poulsen, A. Godfrey, Z. Q. Liu, J. A. Sharon and X. Huang. Three-Dimensional Orientation Mapping in the Transmission Electron Microscope. *Science* 332:833–834, 2011. doi:10.1126/science.1202202
- [Liu98] C.T. Liu, E.P. George, P.J. Maziasz and J.H. Schneibel. Recent advances in B2 iron aluminide alloys: deformation, fracture and alloy design. *Materials Science and Engineering A*. 258:84–98, 1998. doi:10.1016/S0921-5093(98)00921-6
- [Lu93] K. Lu and M.L. Sui. An explanation to the abnormal Hall–Petch relation in nanocrystalline materials. *Scripta Metallurgica et Materialia*. 28:1465–1470, 1993 doi:10.1016/0956-716X(93)90576-E
- [Malek95] J. Malek. The applicability of Johnson-Mehl-Avrami model in the thermal analysis of the crystallization kinetics of glasses. *Thermochimica Acta*. 267:61–73, 1995. doi:10.1016/0040-6031(95)02466-2
- [Mangler09] C. Mangler *Transmission Electron Microscopy Studies of nanocrystalline FeAl produced by High Pressure Torsion*. PhD thesis, University of Vienna, 2009. AC07451944

- [McFadden99] S.X. McFadden, R.S. Mishra, R.Z. Valiev, A.P. Zhilyaev and A.K. Mukherjee. Low-temperature superplasticity in nanostructured nickel and metal alloys. *Nature*. 398:684–686, 1999. doi:10.1038/19486
- [Mendelev07] M. I. Mendelev and B. S. Bokstein. Molecular dynamics study of vacancy migration in Al. *Materials Letters*. 61:2911–2914, 2007. doi:10.1016/j.matlet.2006.10.024
- [Menendez09] E. Menendez, M.O. Liedke, J. Fassbender, T. Gemming, A. Weber, L.J. Heyderman, K.V. Rao, S.C. Deevi, S. Surinach, M. Dolors Baro, J. Sort and J. Nogues. Direct Magnetic Patterning due to the Generation of Ferromagnetism by Selective Ion Irradiation of Paramagnetic FeAl Alloys. *Small*. 5:229–234, 2009 doi:10.1002/sml.200800783
- [Meyers06] M.A. Meyers, A. Mishra and D.J. Benson. Mechanical properties of nanocrystalline materials. *Progress in Materials Science*. 51:427–556, 2006. doi:10.1016/j.pmatsci.2005.08.003
- [Midgley09] R.E. Midgley and P.A. Dunin-Borkowski. Electron tomography and holography in materials science. *Nature Materials*, 8:271–280, 2009. doi:10.1038/nmat2406
- [Mikaekyan00] K.N. Mikaekyan, I.A. Ovid’ko and A.E. Romanov. Disclination-structural-unit model of quasiperiodic tilt boundaries of finite extent. *Materials Science and Engineering A*. 255:61–65, 2000. doi:10.1016/S0921-5093(00)00884-4
- [Mittemeijer92] E. J. Mittemeijer. Analysis of the kinetics of phase transformations. *Journal of Materials Science*. 27:3977–3987, 1992. doi:10.1007/BF01105093
- [Morris02a] D.G. Morris, X. Amils, J. Nogues, S. Surinach, M.D. Baro and M.A. Munoz-Morris. Disorder of B2 intermetallics by ball milling, with particular attention to FeAl. *International Journal of Non-Equilibrium Processing*. 11:379, 2002. ISSN:1368-9290
- [Morris02b] D.G. Morris and M.A. Munoz-Morris. Microstructure of severely deformed Al–3Mg and its evolution during annealing. *Acta Materialia*. 50:4047–4060, 2002. doi:10.1016/S1359-6454(02)00203-3

- [Morris68] B. L. Morris and A. Wold. Faraday Balance for Measuring Magnetic Susceptibility. *Review of Scientific Instruments*. 39:1937, 1968. doi:10.1063/1.1683276
- [Morris96] D.G. Morris and S. Gunther. Strength and ductility of Fe-40%Al alloy prepared by mechanical alloying. *Materials Science and Engineering A*. 208:7-19, 1996. doi:10.1016/0921-5093(95)10041-5
- [Morris98] M.A. Morris, O. George and D.G. Morris. Vacancies, vacancy aggregates and hardening in FeAl. *Materials Science and Engineering A*. 258:99-107, 1998. doi:10.1016/S0921-5093(98)00922-8
- [Mukherjee02] A.K. Mukherjee. An examination of the constitutive equation for elevated temperature plasticity. *Materials Science and Engineering A*. 322:1-22, 2002. doi:10.1016/S0921-5093(01)01115-7
- [Müller00] M.A. Müller. *Aktivierungsvolumen und chemische Umgebung von thermischen Leerstellen in intermetallischen Verbindungen*. Dissertation, Universität Stuttgart, 2000. urn:nbn:de:bsz:93-opus-6485
- [Müller01] M.A. Müller, W. Sprengel, J. Major and H. E. Schaefer. Activation Volume and Chemical Environment of Atomic Vacancies in Intermetallic Compounds. *Materials Science Forum*. 363-365:85-87, 2001. doi:10.4028/www.scientific.net/MSF.363-365.85
- [Nanu05] M. Nanu, J. Schoonman and A. Goossens. Nanocomposite Three-Dimensional Solar Cells Obtained by Chemical Spray Deposition. *Nano Letters*. 5:1716-1719, 2005. doi:10.1021/nl0509632
- [Nazarov93] A.A. Nazarov1, A.E. Romanov and R.Z. Valiev. On the structure, stress fields and energy of nonequilibrium grain boundaries. *Acta Metallurgica et Materialia*. 41:1033-1040, 1993. doi:10.1016/0956-7151(93)90152-I
- [Nellist04] P. D. Nellist, M.F. Chisholm, N. Dellby, O.L. Krivanek, M.F. Murriff, Z.S. Szilagy, A.R. Lupini, A. Borisevich, W.H. Sidesand and S.J. Pennycook. Direct Sub-Angstrom Imaging of a Crystal Lattice. *Science*. 305:1741, 2004. doi:10.1126/science.1100965

- [Okamoto72] H. Okamoto and P.A. Beck. Magnetische Eigenschaften von Fe_3Al und FeAl und spezifische Wärmen bei tiefen Temperaturen *Monatshefte für Chemie* 103:907–921, 1972. doi:10.1007/bf00905453
- [Ovidko05] I.A. Ovid'ko. Superplasticity and ductility of superstrong nano-materials. *Reviews on Advanced Materials Science*. 10:89–104, 2005. ISSN:16058127
- [Padmanabhan04] K.A. Padmannabhan and H. Gleiter. Optimal structural superplasticity in metals and cermaics of microcrystalline- and nanocrystalline-grain sizes. *Materials Science Engineering A*. 381:28–38, 2004. doi:10.1016/j.msea.2004.02.054
- [Padmanabhan09] K.A. Padmannabhan. Grain boundary sliding controlled flow and its relevance to superplasticity in metals, alloys, ceramics and intermetallics and strain-rate dependent flow in nanostructured materials. *Journal of Materials Science*. 44:2226, 2009. doi:10.1007/s10853-008-3076-1
- [Palumbo90] G. Palumbo, S.J. Thorpe and K.T. Aust. On the contribution of triple junctions to the structure and properties of nanocrystalline materials. *Scripta Metallurgica et Materialia*. 24:1347–1350, 1990. doi:10.1016/0956-716X(90)90354-J
- [Pande93] C.S. Pande, R.A. Masumura and R.W. Armstrong. Pile-up based Hall–Petch relation for nano–scale materials. *Nanostructured Materials*. 2:323–331, 1993. doi:10.1016/0965-9773(93)90159-9
- [Pavlina08] E.J. Pavlina and C.J. Van Tyne. Correlation of Yield Strength and Tensile Strength with Hardness for Steels. *Journal of Materials Engineering and Performance*. 17:888, 2008. doi:10.1007/s11665-008-9225-5
- [Peterlechner09b] M. Peterlechner, T. Waitz and H.P. Karnthaler. Nanoscale amorphization of severely deformed NiTi shape memory alloys. *Scripta Materialia*. 60:1137–1140, 2009. doi:10.1016/j.scriptamat.2009.02.055
- [Phillips79] J.C. Phillips. Topology of covalent non-crystalline solids I: Short-range order in chalcogenide alloys. *Journal of Non-Crystalline Solids*. 34:153–181, 1979. doi:10.1016/0022-3093(79)90033-4

- [Pippan10] R. Pippan, S. Scheriau, A. Taylor, M. Hafok, A. Hohenwarter and A. Bachmaier. Saturation of Fragmentation During Severe Plastic Deformation. *Annual Review of Materials Science*. 40:319–343, 2010. doi:10.1146/annurev-matsci-070909-104445
- [Popa02] N.C. Popa and D. Balzar. An analytical approximation for a size-broadened profile given by the lognormal and gamma distribution. *Journal of Applied Crystallography*. 35:338–346, 2002. doi:10.1107/S0021889802004156
- [Qi96] T. Qi. Ordering and Reordering of Nanophase FeAl Intermetallics Synthesized by Mechanical Alloying. *Chinese Physics Letters*, 13:851–8540, 1996. doi:10.1088/0256-307X/13/11/014
- [QxLaue] M. Krystian. QxLaue – A Laue indexing software.
<http://homepage.univie.ac.at/maciej.krystian/qxl/qxld.html>
- [Raj71] R. Raj and M.F. Ashby. On Grain Boundary Sliding and Diffusional Creep. *Metalurgical Transactions*. 2:1113, 1971. doi:10.1007/BF02664244
- [Reading94] M. Reading, A. Ludget and R. Wilson. Modulated differential scanning calorimetry. *Thermochimica Acta*. 238:295–307, 1994. doi:10.1016/S0040-6031(94)85215-4
- [Reimann01] K. Reimann, H.J. Fecht, H.E. Schaefer. Atomistic modeling of the ordering of disordered nanocrystalline FeAl and NiAl. *Scripta Materialia*. 44:1999–2003, 2001. doi:10.1016/S1359-6462(01)00822-3
- [Reimann02] K. Reimann. *Mechanismen der Ordnungseinstellung in nanokristallinen intermetallischen Verbindungen*. Dissertation, Universität Stuttgart, 2002. urn:nbn:de:bsz:93-opus-10507
- [Reimer08] L. Reimer and H. Kohl. *Transmission electron microscopy: physics of image formation*. Springer series in optical sciences, 2008. ISBN:9780387400938
- [Rentenberger03] C. Rentenberger, T. Waitz and H.P. Karnthaler. TEM investigation of the structure of deformation-induced antiphase boundary faults in Ni₃Al. *Physical Review B*. 67:094109, 2003. doi:10.1103/PhysRevB.67.094109

- [Rentenberger04] C. Rentenberger, T. Waitz and H.P. Karnthaler. HRTEM analysis of nanostructured alloys processed by severe plastic deformation. *Scripta Materialia*. 51:789–794, 2004. doi:10.1016/j.scriptamat.2004.05.008
- [Rentenberger05] C. Rentenberger and H.P. Karnthaler. On the evolution of a deformation induced nanostructure in a Ni₃Al alloy. *Acta Materialia*. 53:3031–3040, 2005. doi:10.1016/j.actamat.2005.03.016
- [Rentenberger08] C. Rentenberger and H. P. Karnthaler. Extensive disordering in long-range-ordered Cu₃Au induced by severe plastic deformation studied by transmission electron microscopy. *Acta Materialia*, 56:2526–2530, 2008. doi:10.1016/j.actamat.2008.01.035
- [Revesz06] A. Revesz, S. Hobor, J.L. Labar, A.P. Zhilyaev and Z. Zsolt. Partial amorphization of a Cu–Zr–Ti alloy by high pressure torsion. *Journal of Applied Physics*. 100:103522, 2006. doi:10.1063/1.2388868
- [Ribarik01] G. Ribárik, T. Ungár and J. Gubicza. MWP-fit: a program for multiple whole-profile fitting of diffraction peak profiles by ab initio theoretical functions. *Journal of Applied Crystallography*. 34:669–676, 2001. doi:10.1107/S0021889801011451
- [Saada05] G. Saada. Hall–Petch revisited. *Materials Science and Engineering A*. 400–401:146–149, 2005 doi:10.1016/j.msea.2005.02.091
- [Saito98] Y. Saito, N. Tsuji, H. Utsunomiya, T. Sakai and R.G. Hong. Ultra-fine grained bulk aluminum produced by accumulative roll-bonding (ARB) process. *Scripta Materialia*. 39:1221–1227. doi:10.1016/S1359-6462(98)00302-9
- [Sang02] Y.H. Sang, M.J. Mehl, D.A. Papaconstantopoulos and M. B. Scott. Application of a tight-binding total-energy method for FeAl. *Journal of Physics: Condensed Matter*. 14:1895–1902, 2002. doi:10.1088/0953-8984/14/8/317
- [Sauvage05] X. Sauvage, F. Wetsche and P. Pareige. Mechanical alloying of Cu and Fe induced by severe plastic deformation of a Cu-Fe composite. *Acta Materialia*. 53:2127–2135, 2005. doi:10.1016/j.actamat.2005.01.024

- [Sauvage07] X. Sauvage, G.P. Dindaa and G. Wilde. Non-equilibrium intermixing and phase transformation in severely deformed Al/Ni multilayers. *Scripta Materialia*. 56:181–184, 2007. doi:10.1016/j.scriptamat.2006.10.021
- [Scattergood92] R.O. Scattergood and C.C. Koch. A modified model for hall-petch behavior in nanocrystalline materials. *Scripta Metallurgica et Materialia*. 27:1195–1200, 1992. doi:10.1016/0956-716X(92)90598-9
- [Schaefer99] H.-E. Schaefer, K. Frenner and R. Wüschum. Time-differential length change measurements for thermal defect investigations: intermetallic B2–FeAl and B2–NiAl compounds, a case study. *Physical Review Letters*. 82:948–951, 1999. doi:10.1103/PhysRevLett.82.948
- [Schafner01] E. Schafner, M. Zehetbauera and T. Ungar. Measurement of screw and edge dislocation density by means of X-ray Bragg profile analysis. *Materials Science and Engineering A*. 319:220–223, 2001. doi:10.1016/S0921-5093(01)00979-0
- [Schafner05b] E. Schafner, G. Steiner, E. Korznikova, M. Kerber and M.J. Zehetbauer. Lattice defect investigation of ECAP-Cu by means of X-ray line profile analysis, calorimetry and electrical resistometry. *Materials Science and Engineering: A*. 410:169–173, 2005. doi:10.1016/j.msea.2005.08.070
- [Schafner05] E. Schafner and M. Zehetbauer. Characterization of Nanostructured Materials by X-ray Line Profile Analysis. *Reviews on Advanced Materials Science*. 10:28–33, 2005. ISSN:16058127
- [Schafner10] E. Schafner. Effects of releasing the hydrostatic pressure on the nanostructure after severe plastic deformation of Cu. *Scripta Materialia*. 62:423–426, 2010. doi:10.1016/j.scriptamat.2009.12.004
- [Schafner11] E. Schafner. Strength response upon pressure release after high pressure torsion deformation. *Scripta Materialia*. 64:130–132, 2011. doi:10.1016/j.scriptamat.2010.09.026
- [Scherik92] A.M. El-Sherik, U. Erb, G. Palumbo and K.T. Aust. Deviations from hall-petch behaviour in as-prepared nanocrystalline nickel. *Scripta Metallurgica et Materialia*. 27:1185–1188, 1992. doi:10.1016/0956-716X(92)90596-7

- [Scherrer18] P. Scherrer, Bestimmung der Grösse und der inneren Struktur von Kolloidteilchen mittels Röntgenstrahlen. *Nachrichten von der Gesellschaft der Wissenschaften zu Göttingen*. 26:98–100, 1918. ISSN:03696650
- [Shrivastava82] S.C. Shrivastava, J.J. Jonas and G. Canova. Equivalent strain in large deformation torsion testing : Theoretical and practical considerations. *Journal of the Mechanics and Physics of Solids*. 30:75–90; 1982. doi:10.1016/0022-5096(82)90014-X
- [Schumann91] H. Schumann and K. Cyrener. *Metallographie*. Deutscher Verlag für Grundstoffindustrie, 1991. ISBN:9783342004318
- [Schwarzer93] R.A. Schwarzer. The determination of local texture by electron diffraction - a tutorial review. *Textures and Microstructures*. 20:7–27, 1993. doi:10.1155/TSM.20.7
- [Shewmon69] P. G. Shewmon. *Transformations in metals*. McGraw-Hill, 1969. ISBN:9788189617189
- [Smith22] R.L. Smith and G.E. Sandland. An accurate method of determining the hardness of metals, with particular reference to those of a high degree of hardness. *Proceedings of the Institution of Mechanical Engineers*. 1:623, 1922. doi:10.1243/PIME_PROC_1922_102_033_02
- [Stadelmann87] P.A. Stadelmann. EMS - a software package for electron-diffraction analysis and HREM image simulation in materials science. *Ultramicroscopy*. 21:131–145, 1987. doi:10.1016/0304-3991(87)90080-5
- [Starink03] M. J. Starink. The determination of activation energy from linear heating rate experiments: a comparison of the accuracy of isoconversion methods. *Thermochimica Acta*. 404:163–176, 2003. doi:10.1016/S0040-6031(03)00144-8
- [Starink04] M. J. Starink. Analysis of aluminium based alloys by calorimetry: quantitative analysis of reactions and reaction kinetics. *International Materials Reviews*. 49:191–226, 2004. doi:10.1179/095066004225010532
- [Stein75] E.M. Stein and G. Weiss. *Introduction to Fourier Analysis on Euclidean Spaces*. Princeton University Press, United States, 1971. ISBN:9780691080789

- [Stokes44] A.R. Stokes and A.J.C. Wilson. The diffraction of X rays by distorted crystal aggregates - I. *Proceedings of the Physical Society*. 56:174–181, 1944. doi:10.1088/0959-5309/56/3/303
- [Sundar03] R.S. Sundar and S.C. Deevi. Effect of Carbon Addition on the Strength and Creep Resistance of FeAl Alloys. *Metallurgical and Materials Transactions A*. 34A:2233–2246, 2003. doi:10.1007/s11661-003-0287-6
- [Suwas08] S. Suwas and N.P. Gurao. Crystallographic texture in Materials. *Journal of the Indian Institute of Science*. 88:151–177, 2008. ISSN:00194964
- [Swygenhoven02] H. Van Swygenhoven, P.M. Derlet and A. Hasnaoui. Atomic mechanism for dislocation emission from nanosized grain boundaries. *Physical Review B*. 66:24101, 2002. doi:10.1103/PhysRevB.66.024101
- [Swygenhoven99] H. Van Swygenhoven, M. Spaczer and A. Caro. Microscopic description of plasticity in computer generated metallic nanophase samples: a comparison between Cu and Ni. *Acta Materialia*. 47:3117–3126, 1999. doi:10.1016/S1359-6454(99)00109-3
- [Tabor96] D. Tabor. Indentation hardness: fifty years on A personal view. *Philosophical Magazine A*. 74:1207, 1996 . doi:10.1007/01418619608239720
- [Taylor34] G. I. Taylor. The Mechanism of Plastic Deformation of Crystals. Part I. Theoretical. *Proceedings of the Royal Society London A*. 145:362–387, 1934. doi:10.1098/rspa.1934.0106
- [Thompson87] P. Thompson, D.E. Cox and J.B. Hastings. Rietveld refinement of Debye-Scherrer synchrotron X-ray data from Al₂O₃. *Journal of Applied Crystallography*. 20:79–83. 1987. doi:10.1107/S0021889887087090
- [Topas] Bruker AXS. TOPAS – A profile and structure analysis software. www.bruker-axs.de/topas.html
- [Uhlemann98] S. Uhlemann and M. Haider. Residual wave aberrations in the first spherical aberration corrected transmission electron microscope. *Ultramicroscopy*. 72:109–119, 1998. doi:10.1016/S0304-3991(97)00102-2
- [Ungar04] T. Ungar. Microstructural parameters from X-ray diffraction peak broadening. *Scripta Materialia*. 51:777–781, 2004. doi:10.1016/j.scriptamat.2004.05.007

- [Ungar05] T. Ungar, G. Tichy, J. Gubicza and R. J. Hellmig. Correlation between subgrains and coherently scattering domains. *Powder Diffraction*. 20:366, 2005. doi:10.1154/1.2135313
- [Ungar96] T. Ungar and A. Borbely. The effect of dislocation contrast on X-ray line broadening: A new approach to line profile analysis. *Applied Physics Letters*. 69:3137, 1996. doi:10.1063/1.117951
- [Ungar98] T. Ungar, A. Revesz and A. Borbely. Dislocations and Grain Size in Electrodeposited Nanocrystalline Ni Determined by the Modified Williamson-Hall and Warren-Averbach Procedures. *Journal of Applied Crystallography*. 31:554–558, 1998. doi:10.1107/S0021889897019559
- [Ungar99b] T. Ungar and G. Tichy. The Effect of Dislocation Contrast on X-Ray Line Profiles in Untextured Polycrystals. *Physica Status Solidi (a)*. 171:425–434, 1999. doi:10.1002/(SICI)1521-396X(199902)171:2<425::AID-PSSA425>3.0.CO;2-W
- [Ungar99] T. Ungar, I. Dragomir and A. Revesz. The contrast factors of dislocations in cubic crystals: the dislocation model of strain anisotropy in practice. *Journal of Applied Crystallography*. 32:922-1002, 1999. doi:10.1107/S0021889899009334
- [Valiev06a] R.Z. Valiev, Y. Estrin, Z. Horita, T.G. Langdon, M.J. Zehetbauer and Y.T. Zhu. Producing bulk ultrafine-grained materials by severe plastic deformation. *JOM Journal of the Minerals, Metals and Materials Society*. 58:33–39, 2006. doi:10.1007/s11837-006-0213-7
- [Valiev06b] R.Z. Valiev and T.G. Langdon. Principles of equal-channel angular pressing as a processing tool for grain refinement. *Progress in Materials Science*. 51:881–981, 2006. doi:10.1016/j.pmatsci.2006.02.003
- [Valiev94] R.Z. Valiev, E.V. Kozlov, Y.F. Ivanov, J. Lian, A.A. Nazarov and B. Baudelet. Deformation behaviour of ultra-fine-grained copper. *Acta Metallurgica et Materialia*. 42:2467-2475, 1994. doi:10.1016/0956-7151(94)90326-3
- [Varin99] R.A. Varin, J. Bystrzycki and A. Calka. Characterization of nanocrystalline Fe–45at%Al intermetallic powders obtained by controlled ball

- milling and the influence of annealing. *Intermetallics*. 7:917–930, 1999. doi:10.1016/S0966-9795(99)00004-7
- [Wang02] Y. Wang. High tensile ductility in a nanostructured metal. *Nature*. 412:912–915, 2002. doi:10.1038/nature01133
- [Wang08] Y.B. Wang, B.Q. Li, M.L. Sui and S.X. Mao. Deformation-induced grain rotation and growth in nanocrystalline Ni. *Applied Physics Letters*. 92:11903, 2008. doi:10.1063/1.2828699
- [Wang95] N. Wang, Z. Wang, K.T. Aust and U. Erb. Effect of grain size on mechanical properties of nanocrystalline materials. *Acta Metallurgica et Materialia*. 43:519–528, 1995. doi:10.1016/0956-7151(94)00253-E
- [Warren50] B.E. Warren and B.L. Averbach. A Quantized The Effect of Cold-Work Distortion on X-Ray Patterns. *Journal of Applied Physics*. 21:595–599, 1950. doi:10.1063/1.1699713
- [Warren90] B.E. Warren. *X-ray Diffraction*. Dover Publications, United States, 1990. ISBN:9780486663173
- [Wei02] Q. Wei, D. Jia, K.T. Ramesh and E. Ma. Evolution and microstructure of shear bands in nanostructured Fe. *Applied Physics Letters*. 1240–1242, 2002. doi:10.1063/1.1501158
- [Welzel05] U. Welzel, J. Ligot, P. Lamparter, A. C. Vermeulen and E.J. Mittemeijer. Stress analysis of polycrystalline thin films and surface regions by X-ray diffraction. *Journal of Applied Crystallography*. 38:1–29, 2005. doi:10.1107/S0021889804029516
- [Westbrook00a] J.H. Westbrook and R.L. Fleischer. *Intermetallic Compounds, Volume 2, Basic Mechanical Properties and Lattice Defects of Intermetallic Compounds*. John Wiley & Sons LTD, 2000. ISBN:9780471611752
- [Westbrook00b] J.H. Westbrook, R.L. Fleischer *Intermetallic Compounds, Volume 9, Structural applications of intermetallic compounds*. John Wiley & Sons LTD, 2000. ISBN:9780471612421
- [Wilde05] G. Wilde, G.P. Dinda and H. Rösner. Synthesis of Bulk Nanocrystalline Materials by Repeated Cold Rolling. *Advanced Engineering Materials*. 7:11–15, 2005. doi:10.1002/adem.200400166

- [Wilkins70] M. Wilkins. The determination of density and distribution of dislocations in deformed single crystals from broadened X-ray diffraction profiles. *Physica Status Solidi*. 2:359–370, 1970. doi:10.1002/pssa.19700020224
- [Williams96] D. B. Williams and C. B. Carter *Transmission Electron Microscopy*. Plenum Press, 1996. ISBN:9780387765006
- [Williamson53] G.K. Williamson and W.H. Hall. X-ray line broadening from fcc aluminium and tungsten. *Acta Metallurgica*. 1:22–31, 1953. doi:10.1016/0001-6160(53)90006-6
- [Wu03] D. Wu, P.R. Munroe and I. Baker. The paramagnetic-to-ferromagnetic transition in B2-structured Fe-Al single crystals: experiments and calculations. *Philosophical Magazine* 83:295–313, 2003. doi:10.1080/0141861021000042280
- [Wu09] G. Wu and S. Zaeferrer. Advances in TEM orientation microscopy by combination of dark-field conical scanning and improved image matching. *Ultramicroscopy*. 109:1317–1325, 2009. doi:10.1016/j.ultramic.2009.06.002
- [Wu98] E. Wu, E. MacA. Gray and E. H. Kisi. Modelling Dislocation-Induced Anisotropic Line Broadening in Rietveld Refinements Using a Voigt Function. I. General Principles. *Journal of Applied Crystallography*. 31:356–362, 1998. doi:10.1107/S002188989701217X
- [Wuerschum95] R. Würschum, C. Grupp and H.-E. Schaefer. Simultaneous study of vacancy formation and migration at high temperatures in B2-Type Fe aluminides. *Physical Review Letters*. 75:97–100, 1995. doi:10.1103/PhysRevLett.75.97
- [Xiao95] H. Xiao and I. Baker. Relationship between point defects and mechanical properties in Fe–Al at room temperature. *Acta metallurgica et materialia*. 43:391–396, 1995. doi:10.1016/0956-7151(95)90295-3
- [Yamagata73] T. Yamagata and H. Yoshida. Deformation behavior of FeAl single crystals. *Materials Science and Engineering*. 12:95–100, 1973. doi:10.1016/0025-5416(73)90132-8
- [Yamaguchi81] M. Yamaguchi, D. P. Pope, V. Vitek and Y. Umakoshi. Planar faults and dislocation dissociations in body-centred-cubic-derivative

- ordered structures. *Philosophical Magazine A*. 43:1265–1275, 1981. doi:10.1080/01418618108236155
- [Yamakov04] V. Yamakov, D. Wolf, S.R. Phillpot, A.K. Mukherjee and H. Gleiter. Deformation-mechanism map for nanocrystalline metals by molecular-dynamics simulation. *Nature Materials*. 3:43–47, 2004. doi:10.1038/nmat1035
- [Yamamoto03] K. Yamamoto, S. Miyazaki, S. Kumai and A. Sato. Strong magnetization by antiphase-boundary tubes in a cyclically deformed Fe-35 at.% Al alloy. *Philosophical Magazine* 83:1431–1449, 2003. doi:10.1080/1478643031000078486
- [Yang99] Y. Yang, I. Baker and P. Martin. On the mechanism of the paramagnetic-to-ferromagnetic transition in Fe-Al. *Philosophical Magazine B* 79:449–461, 1999. doi:10.1080/13642819908206419
- [Yoshimi98] K. Yoshimi, M.H. Yoo and S. Hanada. Slip band propagation and slip vector transition in B2 FeAl single crystals. *Acta Materialia*. 46:5769–5776, 1998. doi:10.1016/S1359-6454(98)00228-6
- [Zehetbauer03] M.J. Zehetbauer, H.P. Stüwe, A. Vorhauer, E. Schafner and J. Kohout. The Role of Hydrostatic Pressure in Severe Plastic Deformation. *Advanced Engineering Materials*. 5:330–337, 2003. doi:10.1002/adem.200310090
- [Zeng06] Q. Zeng and I. Baker. Magnetic properties and thermal ordering of mechanically alloyed Fe-40at%Al. *Intermetallics*. 14:396–405, 2006. doi:10.1016/j.intermet.2005.07.005
- [Zhilyaev08] A. P. Zhilyaev and T. G. Langdon. Using high-pressure torsion for metal processing: Fundamentals and applications. *Progress in Materials Science*. 53:893–879, 2008. doi:10.1016/j.pmatsci.2008.03.002
- [Zhu03] Y.T. Zhu, J.Y. Huang, J. Gubicza, T. Ungar, Y.M. Wang, E. Ma and R.Z. Valiev. Nanostructures in Ti processed by severe plastic deformation. *Journal of Materials Research*. 18:1908–1917, 2003. doi:10.1557/JMR.2003.0267

- [Zhu04] Y.T. Zhu and X. Liao. Nanostructured metals: Retaining ductility. *Nature Materials*. 3:351–352, 2004. doi:10.1038/nmat1141

A Acknowledgements

First of all I would like to thank my supervisor Prof. Christian Rentenberger. Whenever I had a question or a problem he took the time to give me an answer. Thank you for being an amazing teacher, an enthusiastic discussion partner and a supportive supervisor. I am also very grateful to Prof. Hans-Peter Karnthaler for sharing his enthusiasm and vast experience with me. His good advice and support has been invaluable not only for the preparation of publications but also on a personal level. I would like to thank Dr. Clemens Mangler for great cooperation and constant help. Many results included in this work are an outcome of our cooperation. A special thank goes to Prof. Thomas Waitz for supporting me in every possible way. I would like to thank all my colleagues for providing an amazing working environment and especially Dr. Lidija Rafailović, Dr. David Geist and Dr. Martin Peterlechner for our cooperations. I also want to thank Ing. Andreas Berger for his help with specimen preparation, Regina Pinter for her help in administrative issues and Claudia Wich for development of the TEM films. I would like to thank Prof. Erhard Schafner and Mag. Michael Kerber for their help with the X-ray measurements and Prof. Reinhard Pippan and his group at ESI Leoben for help with the HPT deformation.

I would like to thank my parents and my brother for their constant support. I also want to thank my friends for tolerating when I did not have time or when I came too late because I had to finish some work.

Research is only possible with financial support. Therefore I am grateful for the employment by the IC I022-N “Experimental Materials Science - Nanostructured Materials” (a college for PhD students at the University of Vienna) and the project P22440 “Metastable phases in bulk intermetallics - TEM study” funded by the Austrian Science Fund. I am also grateful for financial support by the research project “Bulk Nanostructured Materials” within the research focus “Materials Science” of the University of Vienna.

B Curriculum Vitæ

DIPL.-ING. MAG. CHRISTOPH GAMMER

CONTACT & PERSONAL DATA

Gersthoferstraße 140/4/2

1180 Wien, Austria

Phone: +43-1-4277-51311

Email: christoph.gammer@univie.ac.at

Date of birth: 04th April, 1983

Place of birth: Vienna, Austria

Nationality: Austrian

PROFESSIONAL HISTORY

- 2010–present Member of the research project P22440 *Metastable phases in bulk intermetallics - TEM study* funded by the Austrian science fund. Physics of Nanostructured Materials, University of Vienna.
- 2008–2010 Ph.D. Program IK I022-N *Experimental Materials Science - Nanostructured Materials*. Physics of Nanostructured Materials, University of Vienna.
- 2007–2008 Civil service as paramedic at the Johanniter–Unfall Hilfe in Vienna, Austria.
-

EDUCATION

- May 2011 Physics at the University of Vienna (with distinction).
Thesis Title: *Reordering in nanocrystalline FeAl studied by Transmission Electron Microscopy and Differential Scanning Calorimetry*. Advisor: Prof. Christian Rentenberger.

- Degree awarded: Mag.
- March 2007 Technical Mathematics at the Vienna University of Technology
(with distinction).
Thesis Title: *Distributional boundary values of harmonic and analytic functions*. Advisor: Prof. Harald Woraceck.
Degree awarded: Dipl.-Ing.
- August 2001 United World College of the Adriatic. International School in
Duino, Italy.
International Baccalaureate Diploma awarded.
-

PARTICIPATIONS AT COURSES

- 02.06–12.06.2011 43rd Electron Crystallography Course in Erice, Italy.
- 23.05–25.05.2011 2nd Training Course on X-ray Line Profile Analysis in Budapest,
Hungary.
- 07.07–10.07.2009 International Summer School on Micro-Mechanical Experiments
in Leoben, Austria.
- 12.01–30.01.2009 EMAT Winter Workshop on High Resolution Electron Microscopy
in Antwerp, Belgium.
- 29.06–04.07.2008 Summer School of Calorimetry in Lyon, France.
-

TALKS AT INTERNATIONAL CONFERENCES

- 08/2009 C. Mangler, C. Gammer, C. Rentenberger and H.P. Karnthaler.
3D evolution of the nanocrystalline structure during HPT deformation of FeAl. 15th International Conference on the Strength of Materials in Dresden, Germany.
- 09/2009 D. Geist, C. Gammer, C. Mangler, C. Rentenberger and H.P. Karnthaler.
Electron microscopy of severely deformed intermetallics. Meeting in Honour of Prof. David Cockayne in Oxford, England (**invited**).

-
- 09/2009 C. Rentenberger, C. Mangler, C. Gammer, J. Rajagopalan, and H.P. Karnthaler. *Nanostructures in metals and intermetallics studied by TEM*. Microscopy Conference 2009 in Graz, Austria (**invited**).
- 07/2010 C. Mangler, C. Gammer, H.P. Karnthaler and C. Rentenberger. *Vacancy Induced Transition from a Ferromagnetic to a Paramagnetic State in Nanocrystalline FeAl*. ISMANAM 2010 in Zürich, Switzerland.
- 07/2010 C. Gammer, C. Mangler, H.P. Karnthaler and C. Rentenberger. *Grain Size Reduction by Static Recrystallization in Bulk Nanocrystalline FeAl*. ISMANAM 2010 in Zürich, Switzerland.
- 03/2011 C. Gammer, C. Mangler, H.P. Karnthaler and C. Rentenberger. *Quantitative local profile analysis of nanomaterials based on TEM diffraction*. DPG spring meeting in Dresden, Germany.
- 03/2011 A. Findeisen, C. Gammer, C. Rentenberger and H.P. Karnthaler. *Diffraction spots off the diffraction rings in severely deformed bulk nanocrystalline FeAl*. DPG spring meeting in Dresden, Germany.
- 03/2011 M. Peterlechner, C. Gammer, G. Wilde and T. Waitz. *Martensitic transformation of nanostructured NiTi made by crystallization of a deformation induced amorphous phase*. DPG spring meeting in Dresden, Germany.
- 03/2011 C. Mangler, C. Gammer, H.P. Karnthaler and C. Rentenberger. *Properties of nanocrystalline FeAl produced by High Pressure Torsion*. NanoSPD 5 in Nanjing, China.
- 03/2011 C. Gammer, C. Mangler, H.P. Karnthaler and C. Rentenberger. *Combining advanced transmission electron microscopy methods for a complete structural analysis of bulk nanocrystalline materials*. NanoSPD 5 in Nanjing, China.
- 08/2011 C. Gammer, C. Mangler, H.P. Karnthaler and C. Rentenberger. *Combining TEM diffraction and imaging for a complete structural analysis of bulk nanocrystalline materials using the example of FeAl*. Microscopy Conference 2011 in Kiel, Germany.

- 09/2011 C. Gammer, C. Mangler, H.P. Karnthaler and C. Rentenberger. *TEM investigations of bulk nanocrystalline intermetallics in 3D*. 10th Multinational Congress on Microscopy in Urbino, Italy (**invited**).
- 09/2011 C. Rentenberger, C. Gammer, D. Geist, A. Findeisen, C. Mangler, H.P. Karnthaler. *Metastable structures and phases of intermetallic alloys induced by severe plastic deformation*. ISPMA 12 in Prague, Czech Republic (**invited**).
- 09/2011 A. Findeisen, C. Gammer, H.P. Karnthaler, C. Rentenberger. *Microstructural evolution of intermetallic FeAl deformed by cold rolling and folding*. ISPMA 12 in Prague, Czech Republic.
- 09/2011 D. Geist, C. Gammer, H.P. Karnthaler, C. Rentenberger. *High pressure torsion of intermetallic NiAl*. ISPMA 12 in Prague, Czech Republic.
- 09/2011 C. Rentenberger, C. Gammer, D. Geist, A. Findeisen and H.P. Karnthaler. *Formation and stability of nanoscaled and amorphous structures induced by severe plastic deformation of intermetallics*. Euromat 2011 in Montpellier, France (**invited**).
- 09/2011 C. Rentenberger, C. Gammer, D. Geist, H.P. Karnthaler, G. Dehm, J. Rajagopalan and T.A. Saif *In-situ and post mortem TEM studies of nanostructured materials*. E-MRS 2011 Fall Meeting in Warsaw, Poland (**invited**).

POSTER PRESENTATIONS AT INTERNATIONAL CONFERENCES

- 08/2008 C. Gammer, C. Mangler, C. Rentenberger and H.P. Karnthaler. *Electron diffraction analysis of nanocrystalline FeAl*. 14th European Microscopy Congress in Aachen, Germany.
- 08/2009 C. Gammer, C. Mangler, C. Rentenberger and H.P. Karnthaler. *Determination of grain size and ordered domain size in nanocrystalline FeAl by electron diffraction*. 15th International Conference on the Strength of Materials in Dresden, Germany.

-
- 09/2009 C. Gammer, C. Mangler, C. Rentenberger and H.P. Karnthaler. *Quantitative local scale analysis by electron diffraction applied to nanocrystalline FeAl*. Microscopy Conference 2009 in Graz, Austria.
- 07/2010 C. Gammer, C. Mangler, H.P. Karnthaler and C. Rentenberger. *3D Analysis of Nanocrystalline Materials by Electron Diffraction Methods*. ISMANAM 2010 in Zürich, Switzerland.
- 07/2010 L.D. Rafailovic, C. Gammer, P. Angerer, A. Gavrilovic, G. Nauer, H.P. Karnthaler. *Thermal Treatment of CoNi Electrodeposits*. ISMANAM 2010 in Zürich, Switzerland.
- 09/2010 L.D. Rafailovic, C. Gammer, D. Minic, A. Gavrilovic, P. Angerer, E. Schafler, H.P. Karnthaler, N. Krendelsberger, G. Nauer. *Characterization of Electrochemically Deposited Nanostructured Ternary NiCoFe Alloy Powders*. 61st Annual Meeting of the International Society of Electrochemistry in Nice, France.
- 03/2011 C. Gammer, C. Mangler, H.P. Karnthaler and C. Rentenberger. *TEM diffraction used for 3D profile analysis of nanomaterials*. DPG spring meeting in Dresden, Germany.
- 03/2011 C. Gammer, C. Mangler, H.P. Karnthaler and C. Rentenberger. *Growth of nanosized ordered domains in nanocrystalline intermetallic FeAl studied by TEM methods*. DPG spring meeting in Dresden, Germany.
- 06/2011 C. Gammer, C. Mangler, H.P. Karnthaler, C. Rentenberger. *TEM diffraction profile analysis used for 3D study of nanomaterials*. International School on Crystallography in Erice, Italy.
- 09/2011 C. Gammer, C. Mangler, H.P. Karnthaler and C. Rentenberger. *PASAD-tools, a software for quantitative analysis of SAD patterns*. 10th Multinational Congress on Microscopy in Urbino, Italy.
- 09/2011 C. Gammer, D. Geist, C. Mangler, H.P. Karnthaler and C. Rentenberger. *3D Analysis by Electron Diffraction Methods of Nanocrystalline Materials*. Euromat 2011 in Montpellier, France.

-
- 09/2011 C. Gammer, D. Geist, C. Mangler, H.P. Karnthaler and C. Rentenberger. *Grain Size Reduction by Heating in Bulk Nanocrystalline FeAl*. Euromat 2011 in Montpellier, France.
- 09/2011 L.D. Rafailovic, C. Rentenberger, A. Gavrilovic, C. Kleber, H.P. Karnthaler, C. Gammer. *High pressure torsion of nickel powders obtained by electrodeposition*. 1st International Conference on Nanomaterials: Applications and Properties in Alushta, Ukraine.
-

AWARDS

- 2011 Poster Award at the 44th Course of the International School of Crystallography in Erice, Sicily. “TEM diffraction profile analysis used for 3D study of nanomaterials”.
- 2011 Gold Award for Young Scientist Oral Presentation at the 5th International Conference on Nanomaterials by Severe Plastic Deformation in Nanjing, China. “Combining Advanced Transmission Electron Microscopy Methods for a Complete Structural Analysis of Bulk Nanocrystalline Materials”.
- 2009 Best Poster Award at the Microscopy Congress 2009 in Graz, Austria. “Quantitative local scale analysis by electron diffraction applied to nanocrystalline FeAl”.
-

LIST OF PUBLICATIONS IN PEER-REVIEWED JOURNALS

C. Gammer, C. Mangler, H.P. Karnthaler and C. Rentenberger. Three-dimensional analysis by electron diffraction methods of nanocrystalline materials. *Microscopy and Microanalysis*, in print, 2011.

M. Peterlechner, T. Waitz, C. Gammer and T. Antretter. Martensitic phase transformations of nanocrystalline NiTi shape memory alloys processed by repeated cold rolling. *International Journal of Materials Research (formerly Z. f. Metallkd.)*, 102:634–64, 2011.

C. Mangler, C. Gammer, K. Hiebl, H.P. Karnthaler and C. Rentenberger. Thermally induced transition from a ferromagnetic to a paramagnetic state in nanocrystalline FeAl processed by high-pressure torsion. *Journal of Alloys and Compounds*, 509 Suppl.1:389–392, 2011 (**highlighted paper**).

C. Gammer, C. Mangler, H.P. Karnthaler and C. Rentenberger. Growth of nanosized chemically ordered domains in intermetallic FeAl made nanocrystalline by severe plastic deformation. *Scripta Materialia*, 65:57–60, 2011.

C. Mangler, C. Gammer, C. Rentenberger and H.P. Karnthaler. Structural modifications during heating of bulk nanocrystalline FeAl produced by high pressure torsion. *Acta Materialia*, 58:5631–5638, 2010.

C. Gammer, C. Mangler, C. Rentenberger and H.P. Karnthaler. Quantitative local profile analysis of nanomaterials by electron diffraction. *Scripta Materialia*, 63:312–315, 2010.

D. Geist, C. Gammer, C. Mangler, C. Rentenberger and H.P. Karnthaler. Electron Microscopy of severely deformed L1₂ intermetallics. *Philosophical Magazine*, 90:4635–4645, 2010.